eLIFE
elifesciences.org

RESEARCH ARTICLE

Figures and figure supplements

Matrix-regulated integrin $\alpha_v\beta_5$ maintains $\alpha_5\beta_1$-dependent desmoplastic traits prognostic of neoplastic recurrence

Janusz Franco-Barraza *et al*

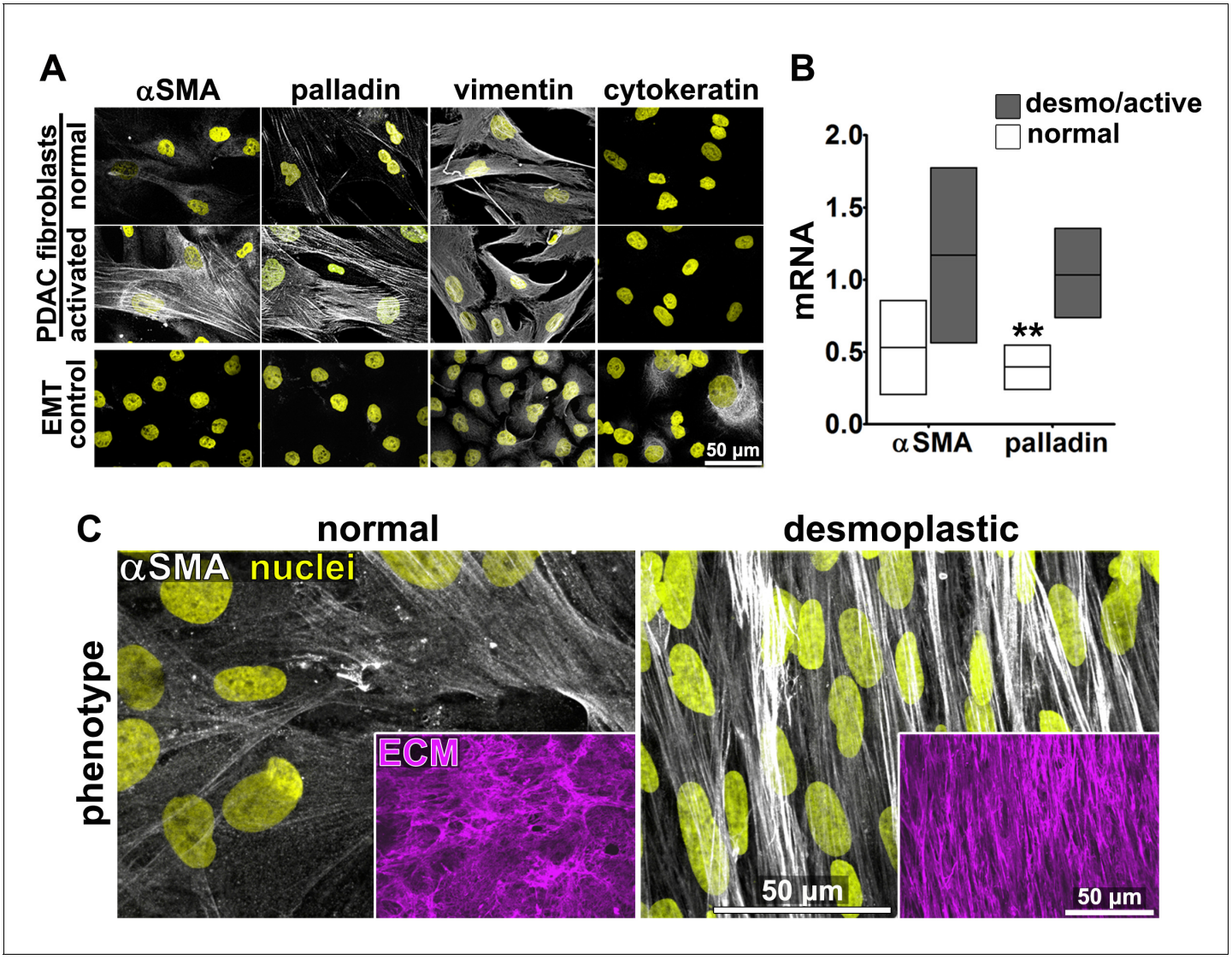

Figure 1. Characterization of human fibroblastic cells isolated from PDAC surgical samples. Fibroblastic cells were isolated from normal or tumoral surgical samples from PDAC patients. (**A**) Representative indirect immunofluorescent assessments of vimentin-positive and pan-cytokeratin-negative fibroblasts, isolated from PDAC surgical specimens. Harvested cells were probed for desmoplastic markers αSMA and palladin, while the pancreatic cancer cell line, Panc1, was used as an epithelial-to-mesenchymal transduced (EMT) control that is known to express both epithelial and mesenchymal markers. Assorted markers are shown in white while counterstained Hoechst-identified nuclei are shown in yellow. (**B**) The bar chart shows normal vs. desmoplastic mRNAs levels, corresponding to αSMA and palladin obtained by RT-qPCR from the indicated 3D-cultures following ECM production (obtained by confluent culturing of fibroblasts in the presence of ascorbic acid for a period lasting 8 days [***Franco-Barraza et al., 2016***]) (**p=0.0286). (**C**) Representative images of normal vs. desmoplastic phenotypes after 3D ECM production; comparison of low vs. high αSMA levels (white), heterogeneous/round vs. elongated/spindled nuclei (yellow) and disorganized/isotropic vs. parallel aligned/anisotropic ECMs (magenta) are evident in the representative images. Note that the examples shown corresponds to the matching pair of (naïve vs. desmoplastic) fibroblastic cells that were harvested from surgical samples corresponding to patient #1 and that this pair of cells was used for all examples provided in figures below, unless otherwise stated.

DOI: 10.7554/eLife.20600.003

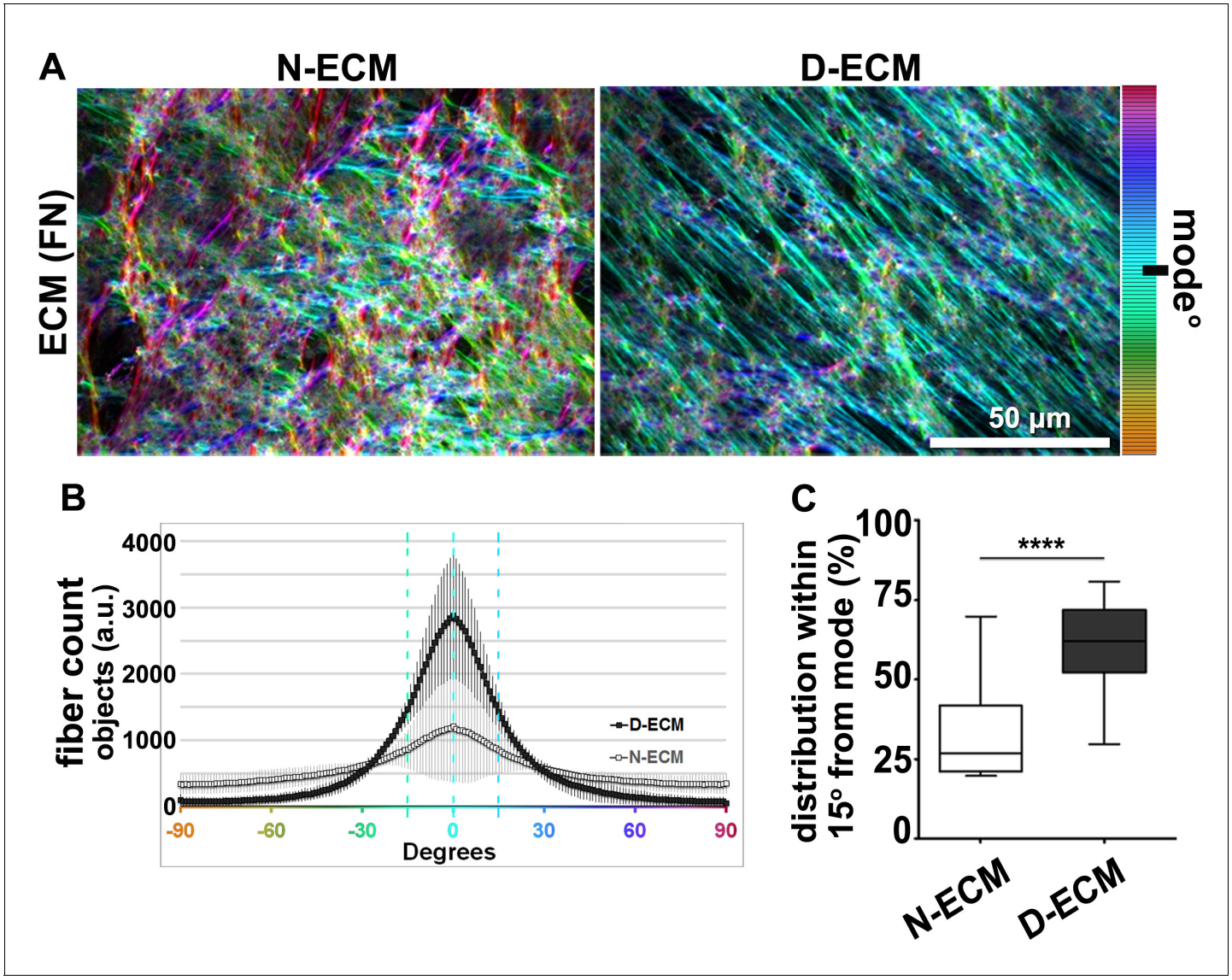

Figure 1—figure supplement 1. CAFs produce anisotropic D-ECMs. (**A**) Images representative of 3D ECM phenotypes: normal (produced by naïve stellate cells N-ECM) and desmoplastic (produced by CAFs D-ECM). The distributions of ECM fiber angles , measured with Image-J's 'OrientationJ' plug, are represented by the various colors; all were normalized using hue values for common, cyan, mode angle visualization as represented on the bar in the right. (**B**) Curves corresponding to the indicated experimental conditions depicting averaged and variations of angle distributions that were normalized to 0˚ modes. Dotted line areas depict a 15˚ spread from the mode. (**C**) Plotted data depicting summarized percentages of fibers distributed at 15˚angles from the mode corresponding to the indicated experimental conditions. Note that comparison between N-ECMs and D-ECMs showed statistically significant differences with p values smaller than 0.0001 (****).

DOI: 10.7554/eLife.20600.004

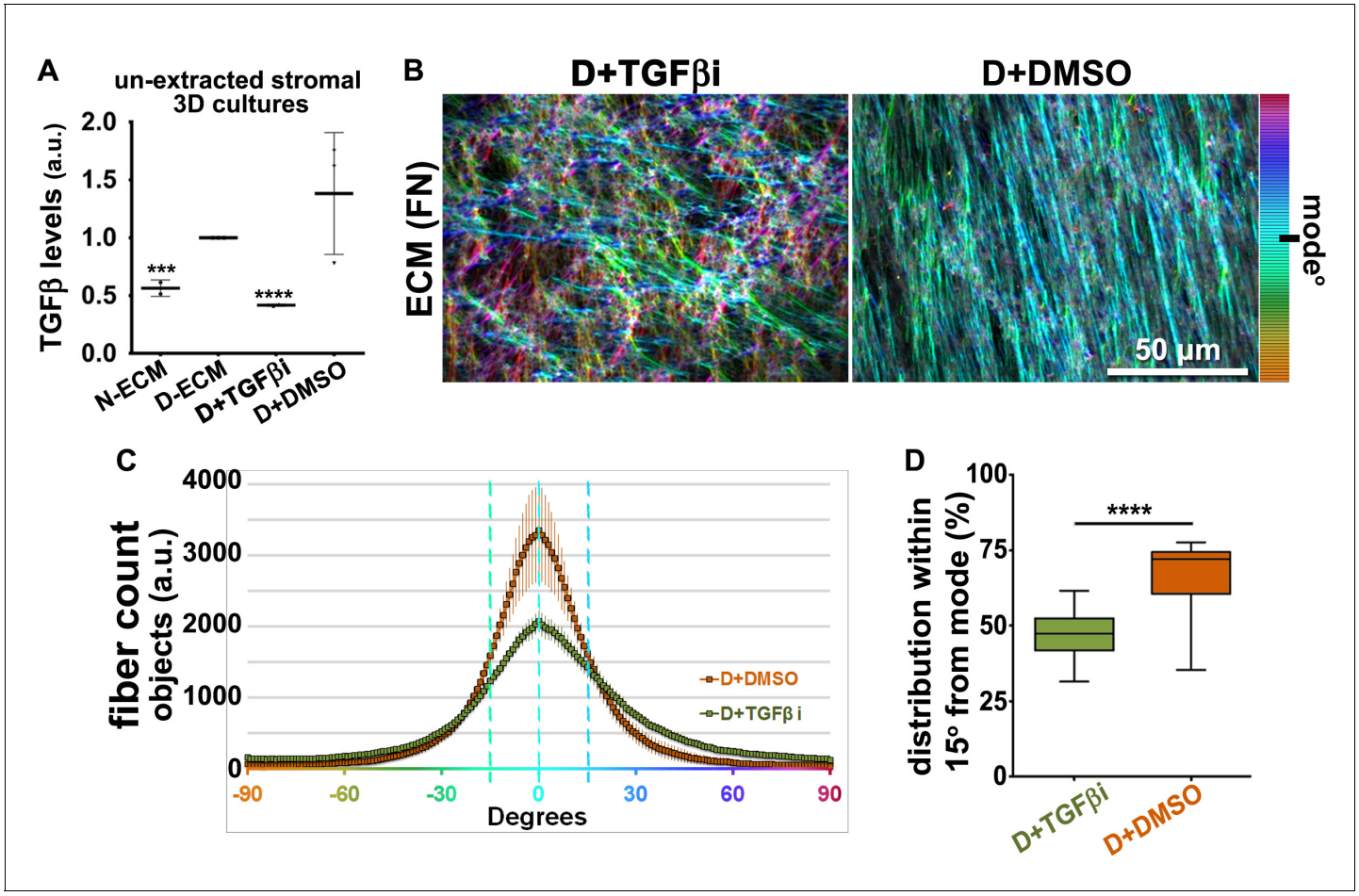

Figure 1—figure supplement 2. TGFβ inhibition disrupts anisotropy of D-ECM devoid of preventing CAF matrix fibrillogenesis. (**A**) TGFβ protein levels from lysates corresponding to 3D normal (N-ECM) and desmoplastic (D-ECM) matrices, produced by naïve fibroblastic stellate cells or CAFs, respectively, in the presence of the small molecule TGFβ1-receptor inhibitor SB431542 (D+TGFβ-i) or vehicle control (D+DMSO), were measured by ELISA. Data were normalized to total protein concentration in intact D-ECMs; results are expressed as arbitrary units (one arbitrary unit; a.u.). Significance values are ***p=0.0014, ****p<0.0001. (**B**) ECM fiber angle distributions, measured with Image-J's 'OrientationJ' plug, are represented by the various colors; all were normalized using hue values for common, cyan, mode angle visualization as represented on the bar on the right. Samples represent D-ECMs produced in the presence TGFβ1-receptor blockage (D+TGFβ-i) or vehicle (D+DMSO). Note how TGFβ inhibition causes disorganization of D-ECM (e.g., loss of anisotropic alignment). (**C**) Curves corresponding to the indicated experimental conditions depicting averaged and variations of angle distributions that were normalized to 0˚ modes. Dotted lines depict areas of 15˚ spreads. (**D**) Plotted data depicting summarized percentages of fibers distributed at 15˚angles from the mode corresponding to the indicated experimental conditions. TGFβ blockage during D-ECM production established that alignments were reduced to 47% (****p<0.0001; n = 21), rendering ECMs isotropic or disorganized.

DOI: 10.7554/eLife.20600.005

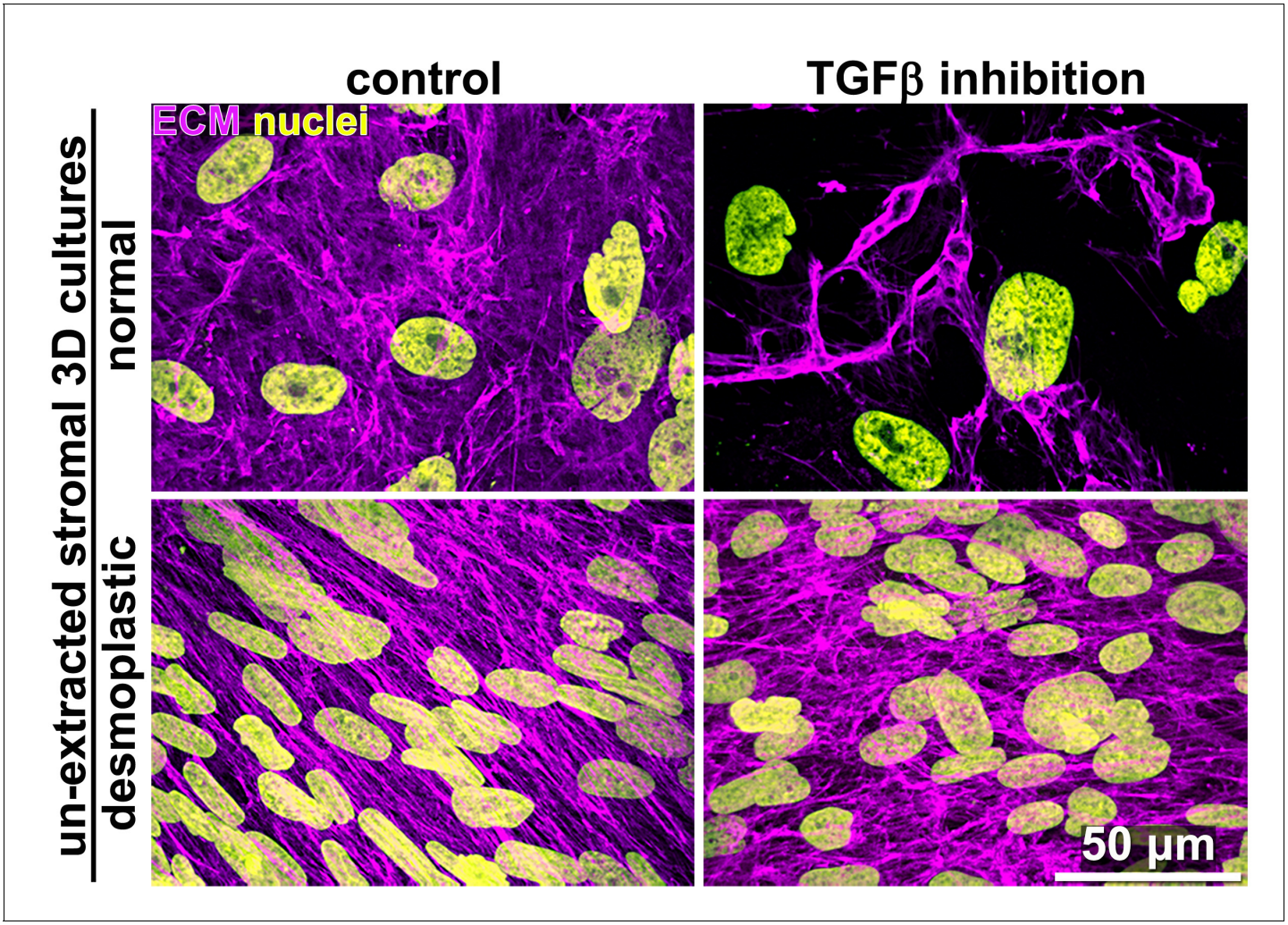

Figure 1—figure supplement 3. TGFβ inhibition disrupts N-ECM production by naïve fibroblastic stellate cells. Representative indirect immunofluorescent images of assorted 'unextracted' 3D cultures depicting nuclei (yellow) and ECMs (magenta) produced by naïve fibroblastic stellate cells or CAFs in the presence or absence of TGFβ1-receptor blockage. Note how TGFβ inhibition causes the disorganization of desmoplastic and the ablation of normal ECMs.

DOI: 10.7554/eLife.20600.006

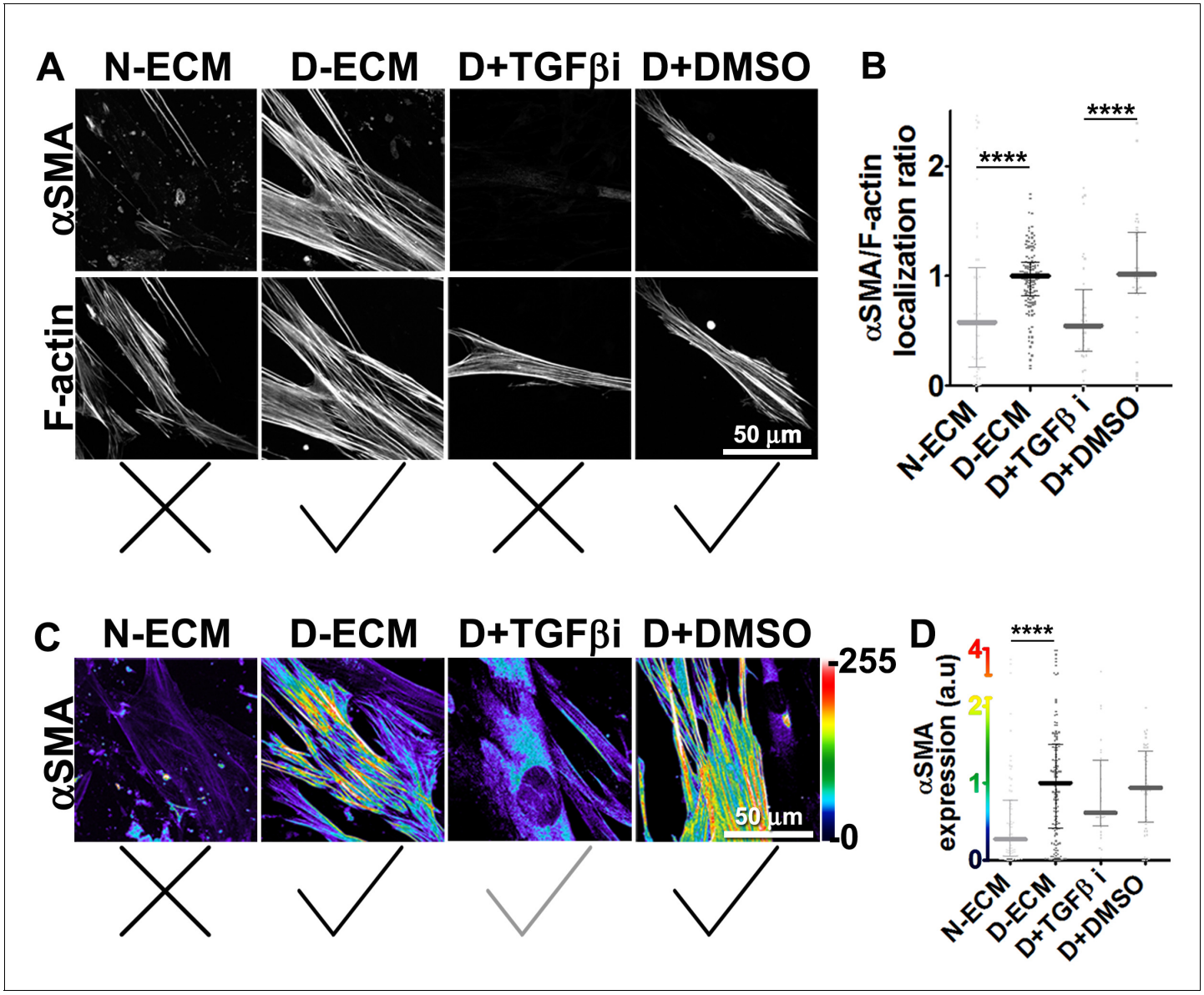

Figure 2. TGFβ is necessary for functional CAF-produced D-ECM. Naïve PDAC fibroblasts were cultured overnight within normal (N-ECM) vs. desmoplastic (D-ECM) ECMs that were produced in the presence or absence of TGFβ1-receptor inhibitor (D + TGFβi) or vehicle control (D + DMSO). All samples were subjected to indirect immunofluorescent labeling of αSMA and counterstained with fluorescently labeled phalloidin to detect actin stress fibers (F-actin). (**A**) Monochromatic images indicating double-labeled staining for αSMA and F-actin. (**B**) Quantification of the levels of localization of αSMA to actin stress fibers (F-actin) from (**A**). (**C**) Pseudo-colored images representing intensity-maps of αSMA levels, with an intensity color bar scale (0–255 intensity tone values) shown to the right. (**D**) Quantification of αSMA intensity from (**C**). Untreated D-ECM conditions were included in all experiments summarized in this figure and served as normalization controls (one arbitrary unit; a.u.). Checkmarks indicate conditions that induce myofibroblastic activation phenotypes. X marks indicate conditions that did not induce myofibroblastic activation. All quantifications and p-values can be found in ***Table 1***.

DOI: 10.7554/eLife.20600.010

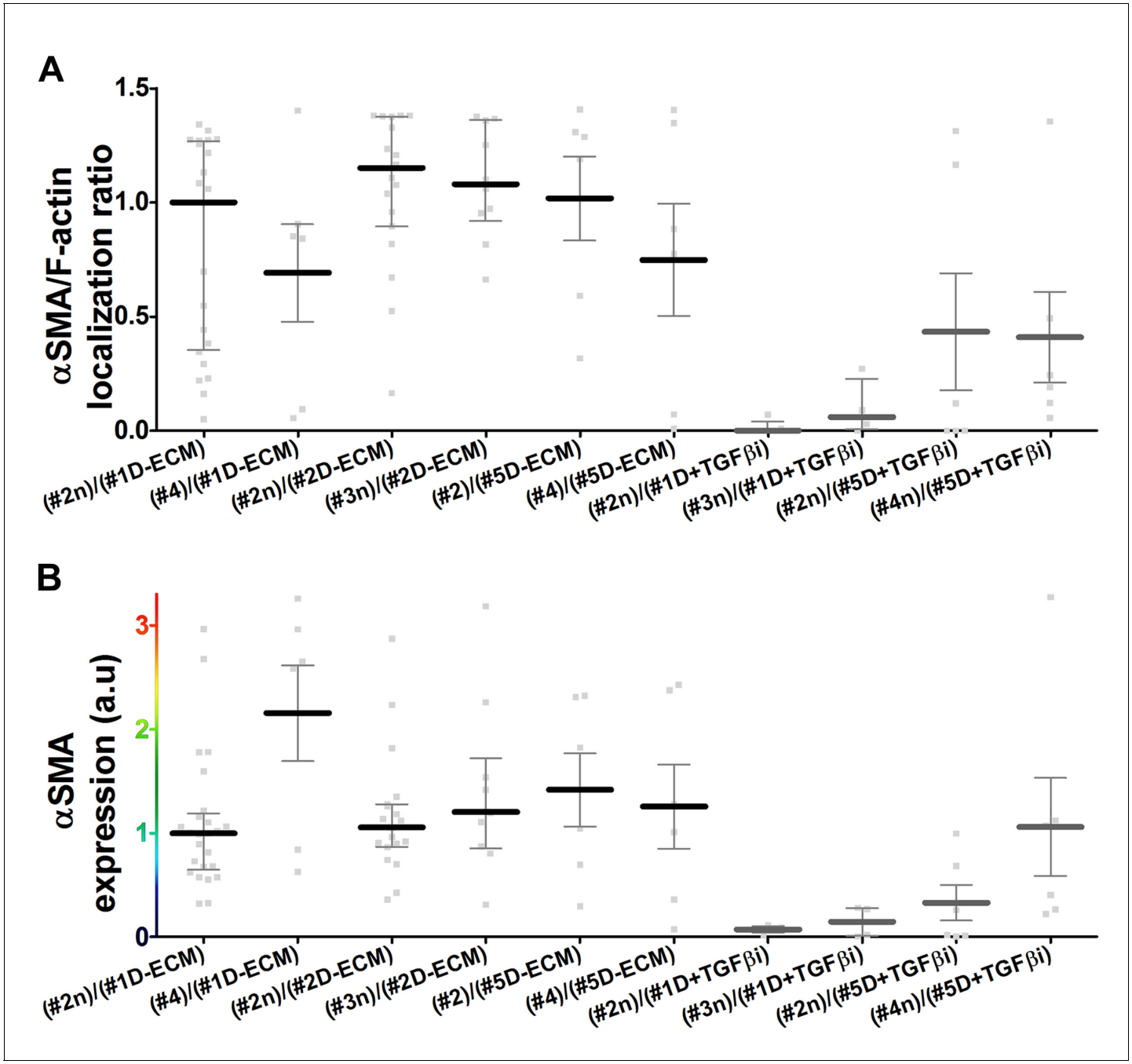

Figure 2—figure supplement 1. Primary CAF-produced D-ECMs induce naïve-to-myofibroblastic activation in normal pancreatic stellate cells. Naïve PDAC fibroblasts or CAFs were isolated from four additional patients and these fibroblasts were cultured overnight within the indicated patient CAF produced matrices, in the presence (D + TGFβi) or absence (D-ECM) of TGFβ1-receptor inhibitor. (**A**) Quantification of the localization of αSMA to actin stress fibers (F-actin) from images of indirect immunofluorescent labeling of αSMA counterstained with fluorescently labeled phalloidin to detect actin stress fibers (F-actin). (**B**) Quantification of images displaying αSMA intensity, from the indicated combinations of fibroblasts and ECMs. Untreated D-ECM conditions from patient #2 naïve fibroblast re-plated on patient-#1-derived D-ECM serve as normalization controls (one arbitrary unit; a.u.). Corresponding quantifications and p-values are listed in ***Table 2***.

DOI: 10.7554/eLife.20600.011

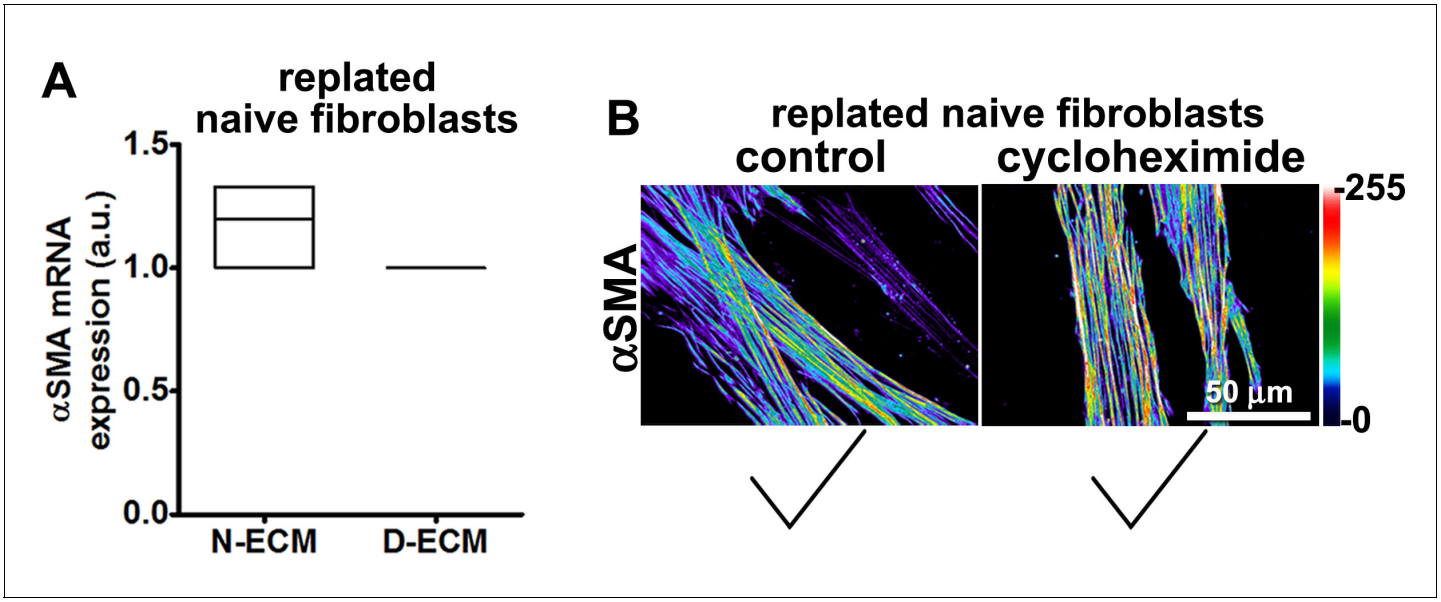

Figure 2—figure supplement 2. D-ECM imparts αSMA post-translational effects during naïve-to-myofibroblastic activation. (**A**) αSMA mRNA levels assessed by RT-qPCR of naïve/normal fibroblasts plated in N- vs. D-ECMs were unaltered. (**B**) Semi-quantitative indirect immunofluorescence showing similar pseudocolors depicting comparable αSMA protein intensity levels of naïve fibroblasts re-plated in D-ECMs comparing vehicle (control) vs. cycloheximide overnight treatments. Intensity levels correspond to the color bar scale shown on the right. Checkmarks indicate conditions that induce myofibroblastic activation phenotypes.

DOI: 10.7554/eLife.20600.012

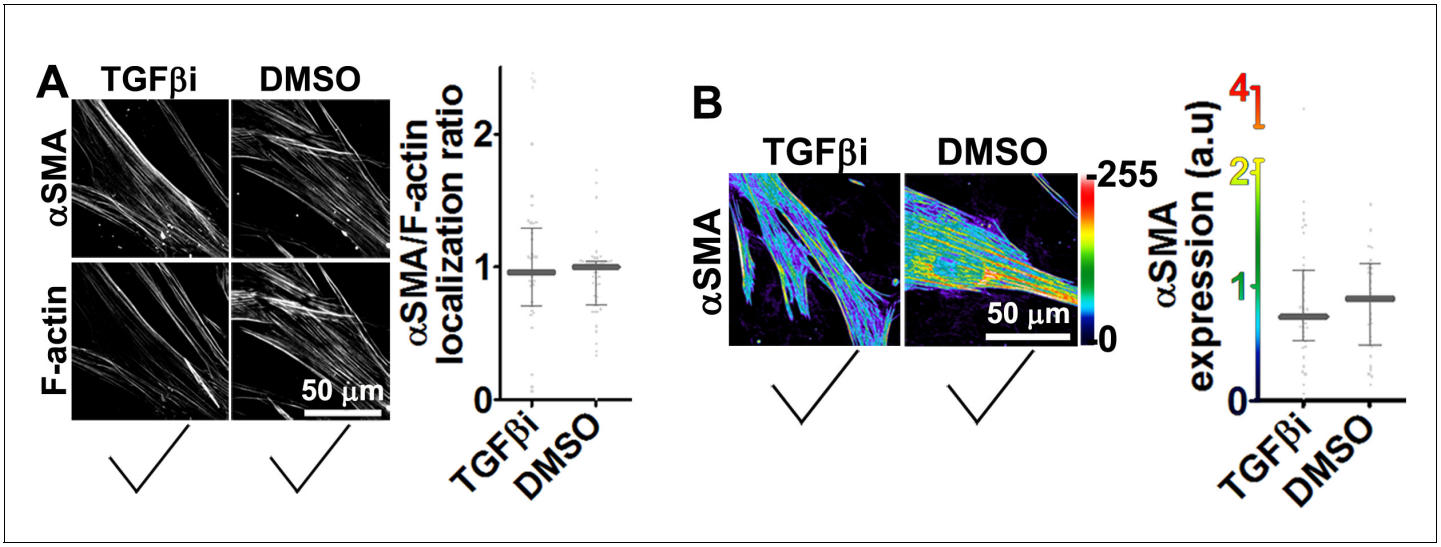

Figure 2—figure supplement 3. TGFβ activity is dispensable for D-ECM-induced naïve-to-myofibroblastic activation. Intact pre-produced **D-ECMs** were seeded overnight with naïve fibroblasts together with TGFβ1-receptor inhibitor (**D + TGFβi**) or vehicle control (**DMSO**). Samples were subjected to indirect immunofluorescent labeling of **αSMA** and counterstained with fluorescently labeled phalloidin to detect actin stress fibers (**F-actin**). (**A**) Representative images of **αSMA** and **F-actin** (**left** images) and the quantification of **αSMA** at stress fibers (graph on the **right**). (**B**) Pseudocolored images represent intensity maps of **αSMA**, with an intensity color bar scale (0–255 intensity tone values) (**left** images) and the quantification of **αSMA** intensity in the graph (**Right**). Checkmarks indicate that conditions effectively induced the myofibroblastic phenotype. Corresponding quantifications and p-values are summarized in ***Table 3***.

DOI: 10.7554/eLife.20600.013

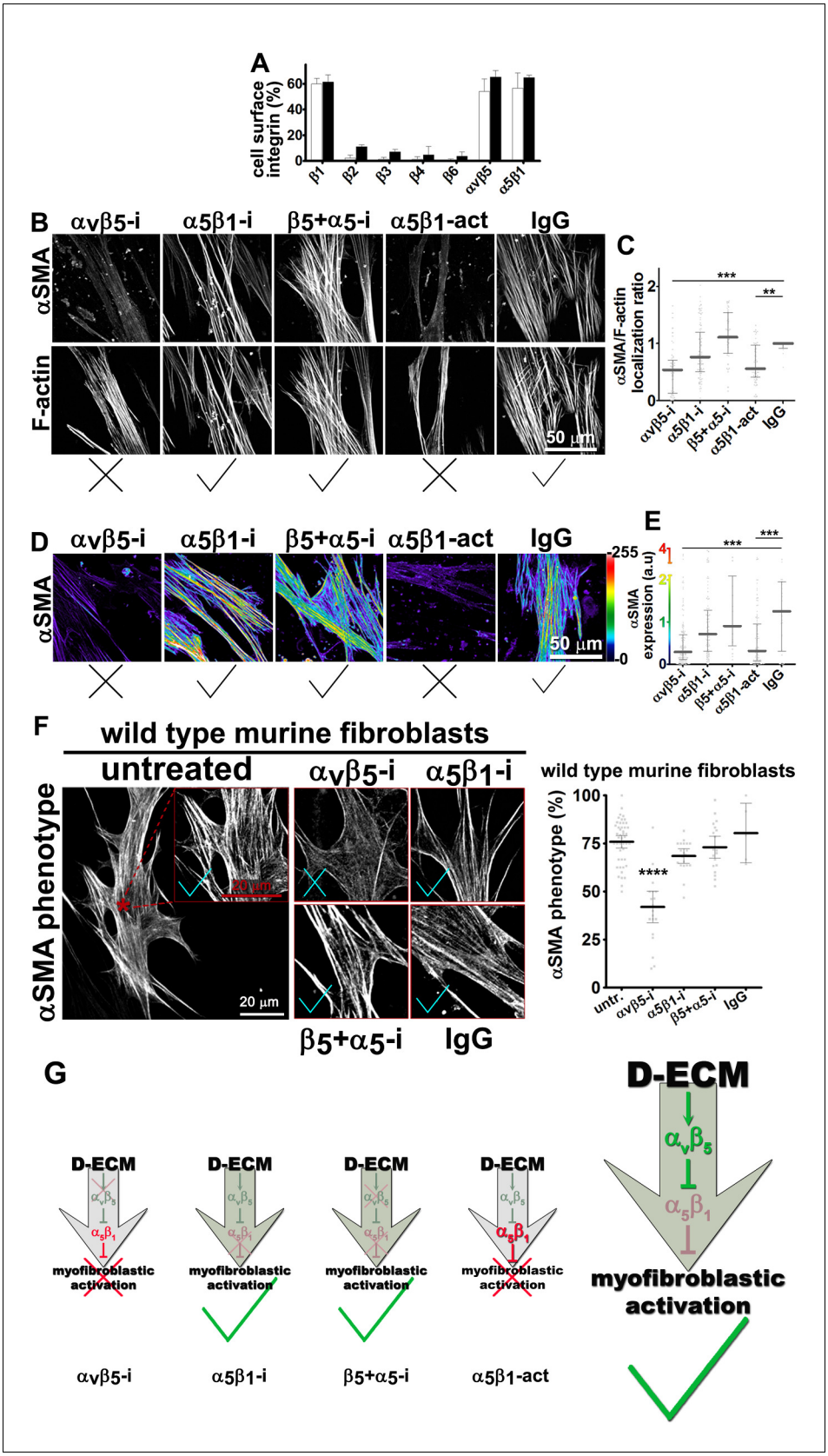

Figure 3. Integrin $\alpha_v\beta_5$ regulates $\alpha_5\beta_1$ activity thereby maintaining D-ECM-induced naïve-to-myofibroblastic activation. (**A**) An integrin-dependent cell adhesion array test was used to assess the PM expression of integrin heterodimers in primary fibroblasts isolated from normal (white bars) vs. matched

Figure 3 continued on next page

Figure 3 continued

tumor tissue (desmoplastic; dark bars). Note that no differences were apparent between the two cell types with regards to levels of $\alpha_v\beta_5$ and $\alpha_5\beta_1$ integrins. (**B**) Naïve human pancreatic fibroblastic stellate cells were re-plated onto D-ECMs overnight in the presence of functional blocking anti-$\alpha_v\beta_5$-integrin (ALULA [***Su et al., 2007***]; $\alpha_v\beta_5$-i), functional blocking anti-$\alpha_5\beta_1$-integrin (mAb16 [***Akiyama et al., 1989***]; $\alpha_5\beta_1$-i), combinations of both functional blocking antibodies (β_5-i + α_5-i), functional stabilizing anti-$\alpha_5\beta_1$-integrin (SNAKA51 [***Clark et al., 2005***]; $\alpha_5\beta_1$-act), or non-immunized isotypic antibodies (IgG). Representative monochromatic images of αSMA- and F-actin stained fibroblasts are shown. (**C**) Quantification of the experiment performed in (**B**). (**D**) Pseudocolored images depicting the intensity of αSMA expression including a color bar scale (0–255 intensity tone values). (**E**) Quantification of (**D**). Note that corresponding quantifications and p-values, for results shown in (**B–E**) are summarized in ***Table 4***. (**F**) Naïve murine skin fibroblasts were re-plated onto murine D-ECMs (mD-ECM) produced by murine skin squamous cell carcinoma associated CAFs (***Amatangelo et al., 2005***), and subjected to $\alpha_v\beta_5$-integrin and $\alpha_5\beta_1$-integrin inhibitors alone (ALULA: $\alpha_v\beta_5$-i [***Su et al., 2007***] and BMA5: $\alpha_5\beta_1$i) or in combination (β_5+ α_5-i). The effects on myofibroblastic activation were measured for αSMA as in (**B**). The red asterisk illustrates the area outlined in red in the magnified insert for the intact (untreated) control. The same magnification is shown for the experimental conditions in the additional panels. As a method of quantifying the percentage of cells showing myofibroblastic features, the percentage of cells that have a stress fiber localized (αSMA) phenotype is shown (****$p<0.0001$). Note that inhibition of $\alpha_5\beta_1$-integrin effectively reinstituted the mD-ECM-induced phenotype that was lost by inhibition of $\alpha_v\beta_5$-integrin, just as seen above for the human PDAC system. Checkmarks identify conditions that resulted in myofibroblastic activation, while Xs identify conditions that did not result in myofibroblastic activation. (**G**) Model of D-ECM-induced activation of naïve fibroblasts, dependent on the activity of integrins $\alpha_v\beta_5$ and $\alpha_5\beta_1$. Inhibition of $\alpha_v\beta_{5-}$ integrin results in release of active $\alpha_5\beta_1$-integrin, leading to blockade of D-ECM-induced myofibroblastic activation (1st arrow, red X). The activity of $\alpha_v\beta_{5-}$ integrin is no longer needed in the absence of $\alpha_5\beta_1$-integrin activity, suggesting that $\alpha_5\beta_1$-integrin activity in not necessary for fibroblasts to undergo D-ECM-induced myofibroblastic activation (2nd arrow, green checkmark). Double inhibition of $\alpha_v\beta_5$-integrin and $\alpha_5\beta_1$-integrin results in D-ECM myofibroblastic activation, which proposes that inhibition of $\alpha_5\beta_1$-integrin can overcome or rescue the effects seen under $\alpha_v\beta_5$-integrin inhibition (3rd arrow, green checkmark). Stabilization of $\alpha_5\beta_1$-integrin in its active conformation overcomes the inhibitory/regulatory effects imparted by $\alpha_v\beta_5$-integrin, resulting in ineffective D-ECM-induced myofibroblastic activation (4th arrow, red X). Overall, the model suggests that D-ECM induces $\alpha_v\beta_5$- integrin activity, which in turn results in the regulation of active $\alpha_5\beta_1$-integrin, allowing D-ECM-induced myofibroblastic activation (large arrow to the right, green checkmark).

DOI: 10.7554/eLife.20600.015

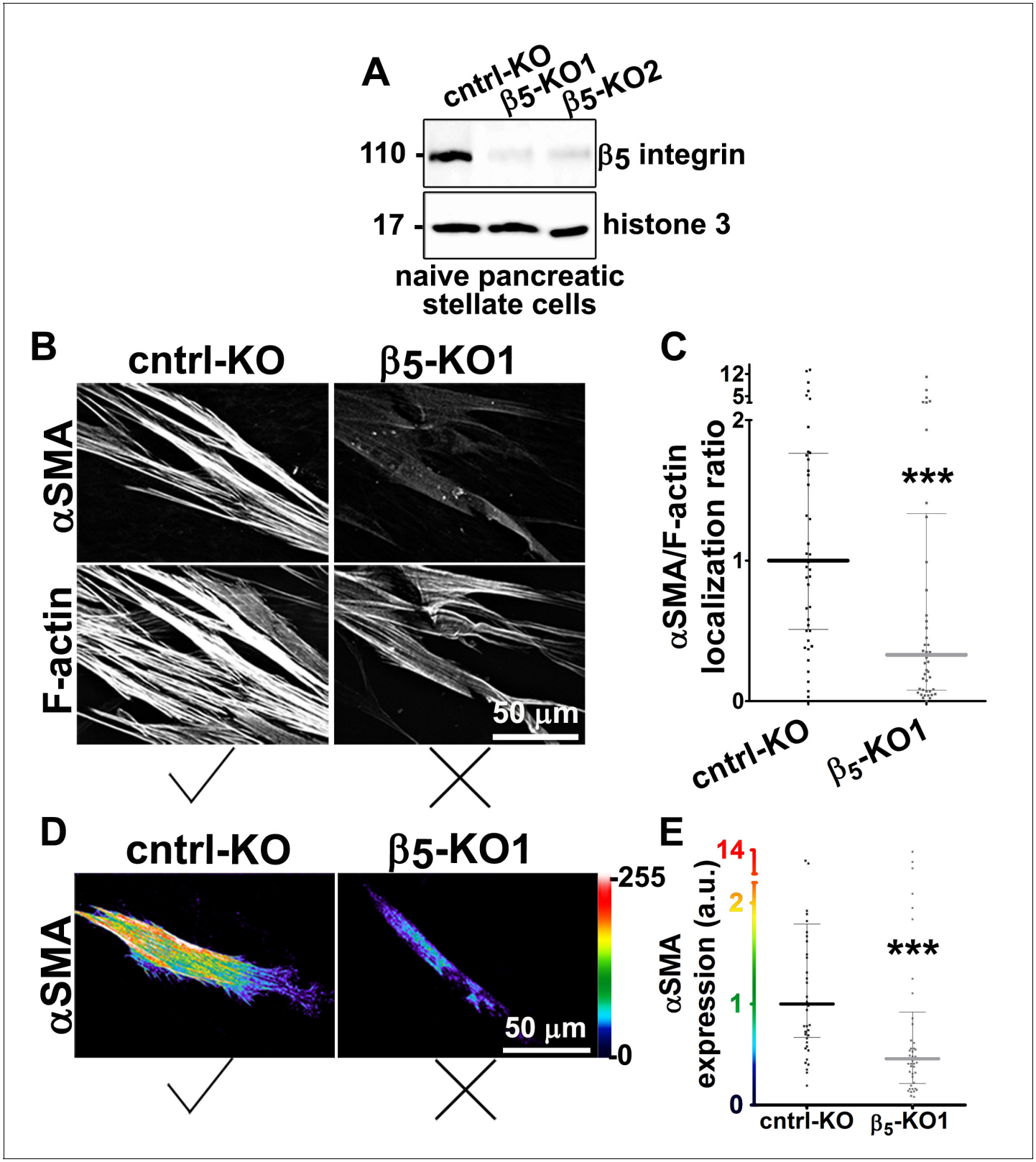

Figure 3—figure supplement 1. Naïve β_5-integrin KO fibroblasts display stunted D-ECM-induced myofibroblastic activation. (**A**) The CRISPR/CAS9 system was used to generate naïve fibroblastic stellate cell β_5-integrin knock-out (KO) (β_5-KO) or control KO (cntrl-KO) lines, whose genoype was confirmed by western blotting. The naïve cntrl-KO and β_5-KO1 fibroblastic stellate cells were challenged by overnight culture within intact D-ECM and

Figure 3—figure supplement 1 continued on next page

Figure 3—figure supplement 1 continued

their myofibroblastic features were assessed. (**B**) Samples were subjected to indirect immunofluorescent labeling of αSMA and counterstained with fluorescently labeled phalloidin to detect actin stress fibers (F-actin) and representative monochromatic images are displayed. (**C**) Quantification of αSMA localized at actin stress fibers (F-Actin) from the experiment in (**B**) (***p=0.0006; n = 46). (**D**) Pseudocolored images represent intensity map outputs of αSMA, with an intensity color bar scale (0–255 intensity tone values) shown to the right. (**E**) Measured values from (**D**) are summarized in the graph (***p=0.0001; n = 46). An experimental condition consisting of naïve cntrl-KO fibroblastic stellate cells cultured in intact D-ECM was included in all experiments; this condition is summarized in this figure and is used for normalization (one arbitrary unit; a.u.). Checkmarks indicate conditions that induce a myofibroblastic activation phenotype, while Xs indicate loss of D-ECM-induced activation.

DOI: 10.7554/eLife.20600.016

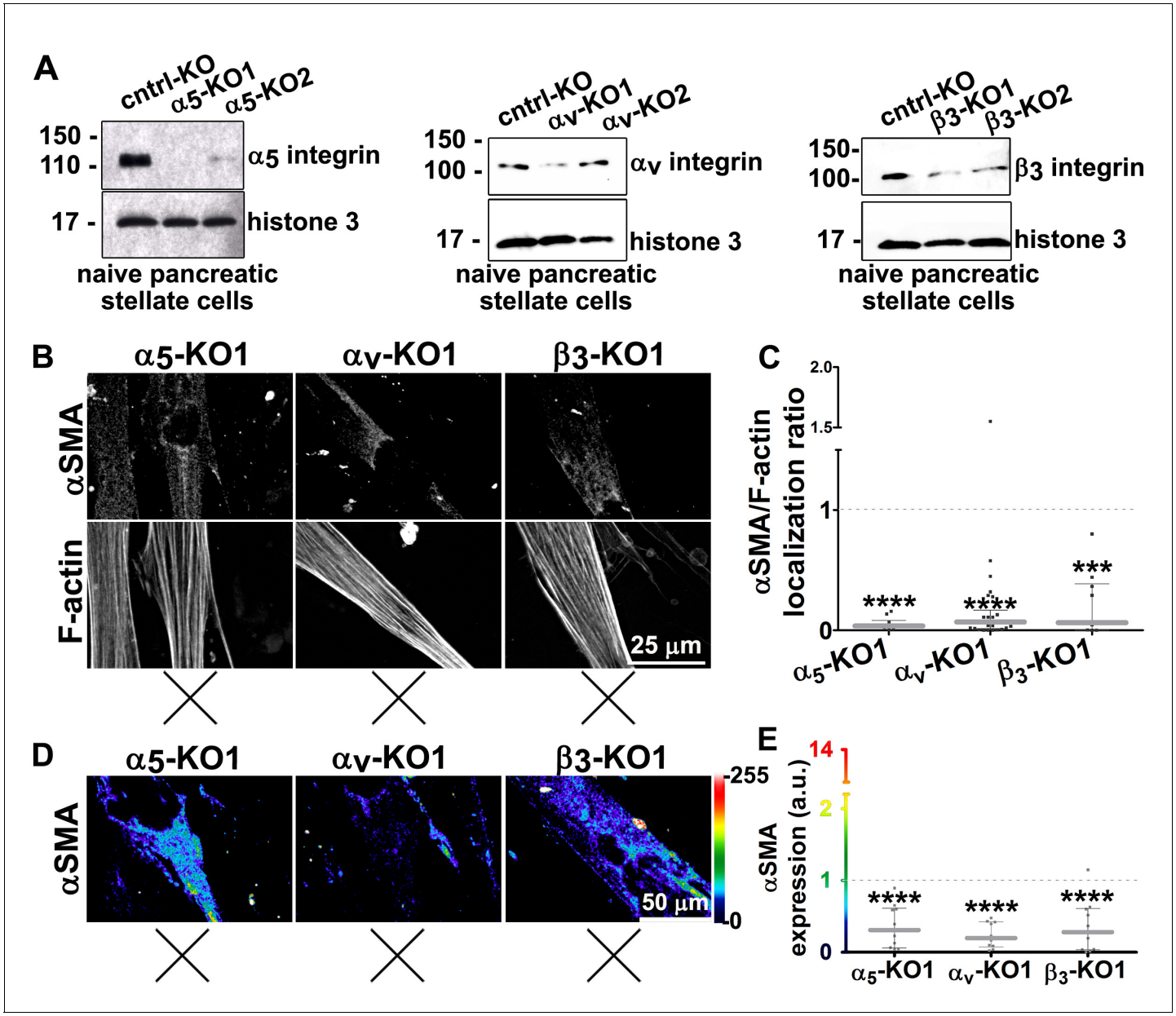

Figure 3—figure supplement 2. Expression of α_5-, α_v- and β_3-integrins in naïve fibroblastic stellate cells is necessary for D-ECM-induced myofibroblastic activation. (**A**) The CRISPR/CAS9 system was used to generate α_5-integrin knock-out (α_5-KO), α_v-integrin knock-out (α_V-KO), β_3-integrin knock-out (β_3-KO) and control KO (cntrl-KO) naïve fibroblasts, which were confirmed by western blotting. The naïve cntrl-KO and assorted integrin KO fibroblastic stellate cells were challenged by overnight culture within intact D-ECM, and their myofibroblastic features were assessed. (**B**) All samples were subjected to indirect immunofluorescent labeling of αSMA and counterstained with fluorescently labeled phalloidin to detect actin stress fibers (F-actin) and representative monochromatic images are displayed. (**C**) Quantification of αSMA localized at actin stress fibers (F-actin) from the experiment in (**B**) (***p=0.0002; ****p<0.0001). (**D**) Pseudocolored images represent intensity maps of αSMA, with an intensity color bar scale (0–255 intensity tone values) shown to the right. (**E**) Measured values from (**D**) are summarized in the graph (****p<0.0001). An experimental condition consisting of naïve cntrl-KO fibroblastic stellate cells cultured in intact D-ECM was included in all experiments summarized in this figure and is used for normalization (one arbitrary unit; a.u., indicated by dotted lines in graphs). X marks indicate loss of D-ECM-induced activation for all tested mutant cells.

DOI: 10.7554/eLife.20600.017

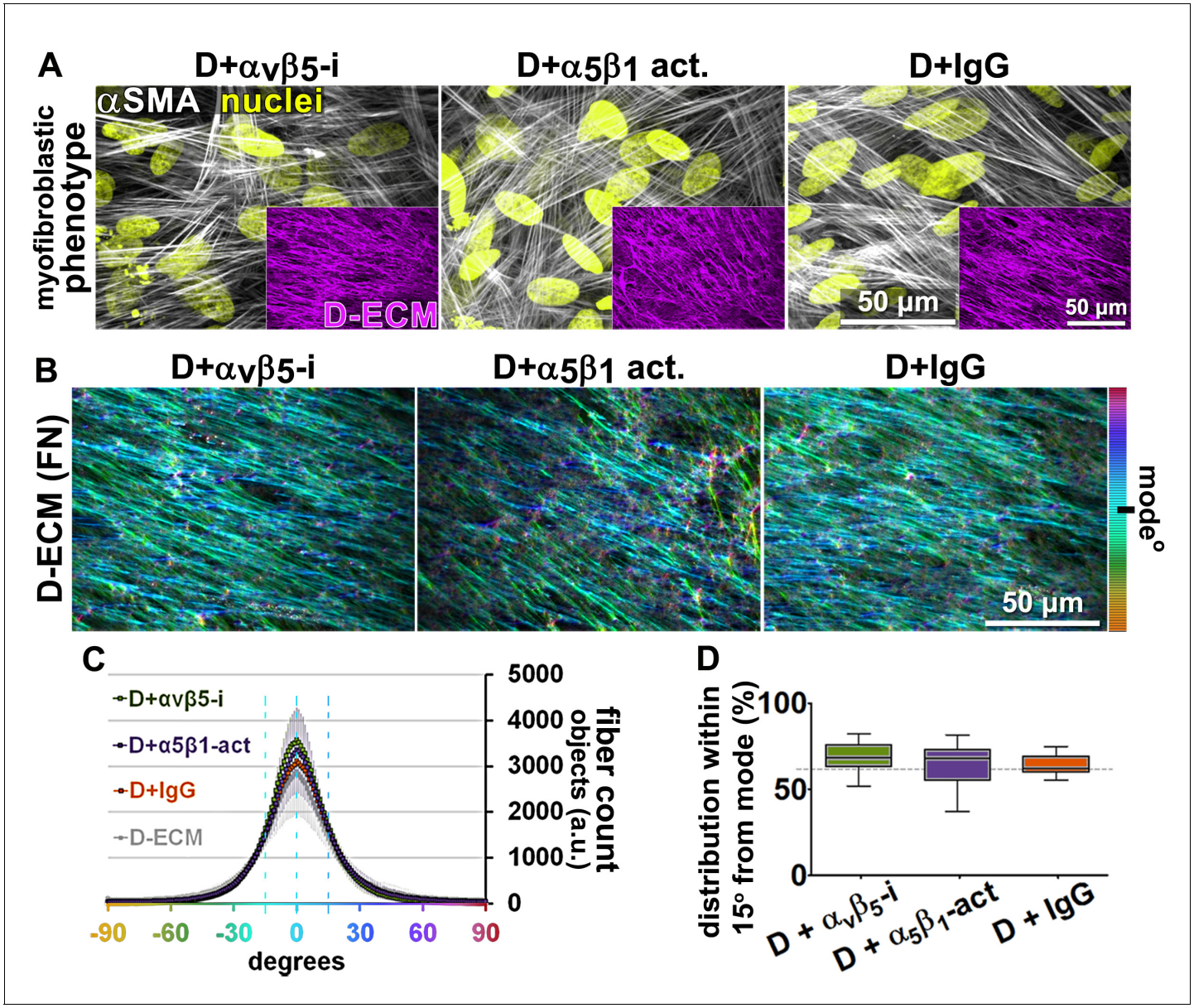

Figure 4. Transient $\alpha_v\beta_5$-integrin inhibition or $\alpha_5\beta_1$-integrin stabilization failed to alter CAF production of anisotropic D-ECM. (**A**) Representative indirect immunofluorescent images of 3D D-ECM producing CAFs in the presence of functional blocking anti-$\alpha_v\beta_5$-integrin (ALULA [***Su et al., 2007***]; D + $\alpha_v\beta_5$-i), active conformation stabilizing anti-$\alpha_5\beta_1$-integrin (SNAKA51 [***Clark et al., 2005***]; D + $\alpha_5\beta_1$-act.) or non-immunized isotypic antibodies (D + IgG). Spinning disk confocal monochromatic images, obtained following indirect immunofluorescence, show nuclei (Hoechst; yellow), αSMA (white) and ECM (fibronectin; magenta). (**B**) The corresponding ECM fiber angle distributions, determined by Image-J's 'Orientation J' plugin, were normalized using hue values for a cyan mode angle visualization as shown in the bar on the right. (**C**) Corresponding curves depicting experimental-repetition-averaged variations of angle distributions normalized to 0° modes and summarizing the results. Dotted lines correspond to 15° fiber angle spreads. (**D**) Plotted data depicting summarized percentages of fibers distributed at 15° angles from the mode for each experimental condition. The dotted line denotes 55% alignment. Note how none of the treatments seem to have altered the myofibroblastic features of CAFs or their capability to produce anisotropic D-ECMs.

DOI: 10.7554/eLife.20600.018

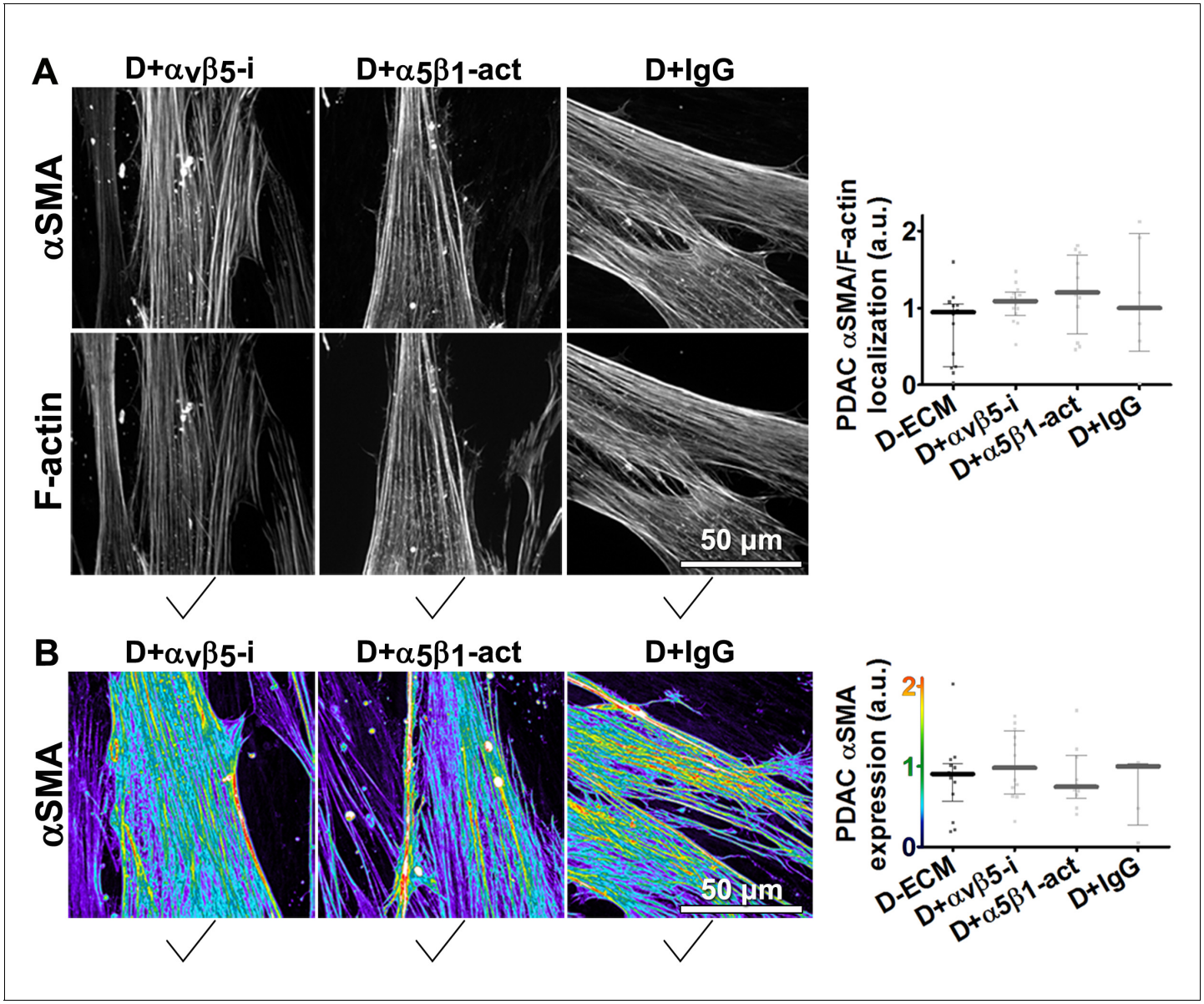

Figure 4—figure supplement 1. D-ECMs produced by CAFs under transient $\alpha_v\beta_5$-integrin inhibition or stabilization of $\alpha_5\beta_1$-integrin activity are functionally intact. Naïve fibroblasts were plated onto D-ECMs that were produced in the presence of functional blocking anti-$\alpha_v\beta_5$-integrin (ALULA [***Su et al., 2007***]; D + $\alpha_v\beta_5$-i), active conformation stabilizing anti-$\alpha_5\beta_1$-integrin (SNAKA51 [***Clark et al., 2005***]; D + $\alpha_5\beta_1$-act.) or non-immunized isotypic antibodies (D + IgG), and αSMA and actin stress fibers (F-actin) were immunofluorescently labeled. (**A**) Monochromatic images indicative of double-labeled αSMA and F-actin are shown, while levels of total αSMA localized at corresponding stress fibers are plotted in the graph to the right. (**B**) Pseudocolored images represent αSMA intensity values, which are summarized in the graph to the right. Checkmarks indicate conditions that induce a myofibroblastic activation phenotype. Note that D-ECMs that were produced under $\alpha_v\beta_5$-integrin inhibitory or active $\alpha_5\beta_1$-integrin stabilizing conditions resulted in no apparent alteration of D-ECM function of CAFs.

DOI: 10.7554/eLife.20600.019

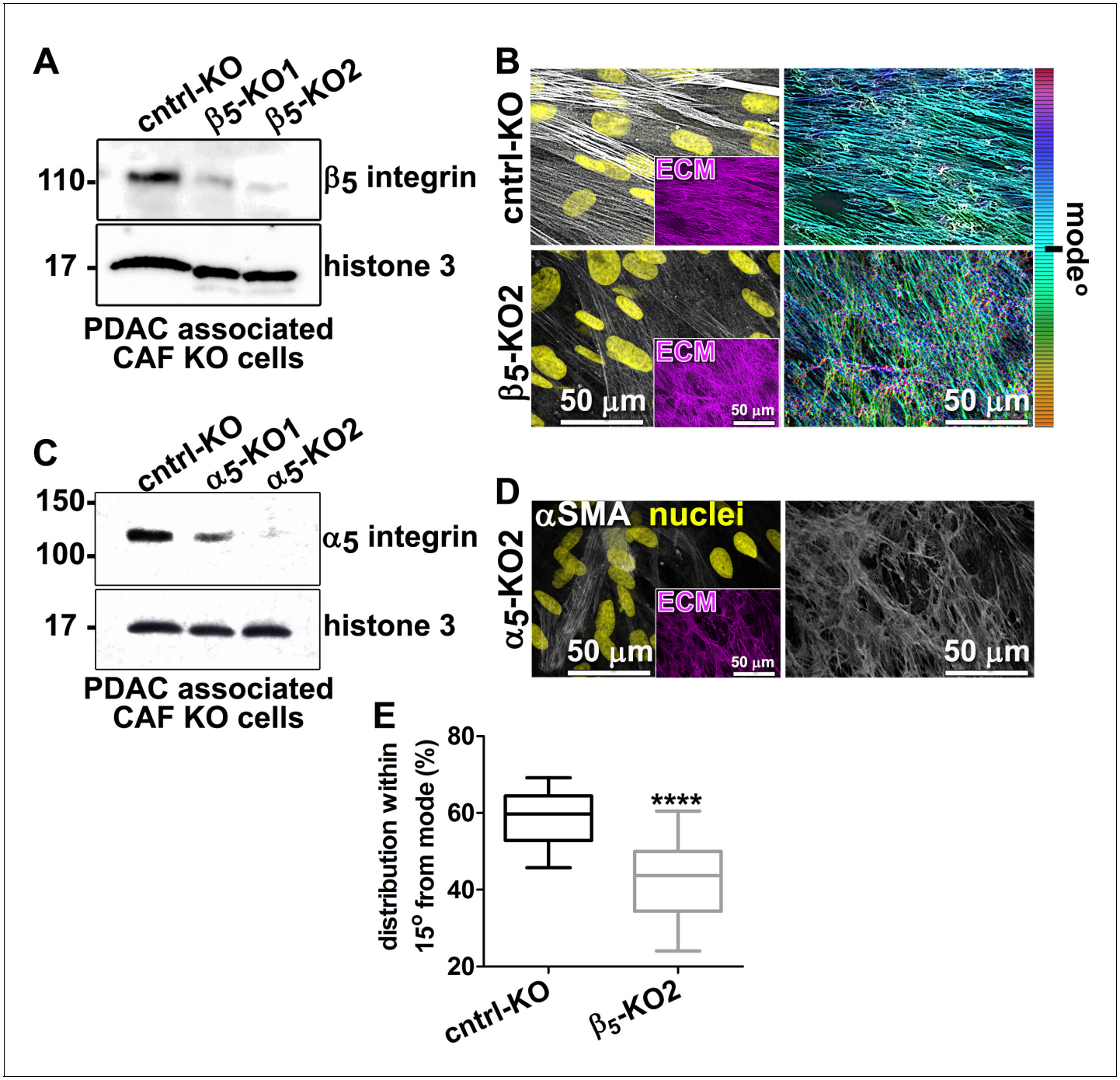

Figure 4—figure supplement 2. Loss of β_5-integrin expression in CAFs impairs D-ECM anisotropy, while expression of α_5-integrin is imperative for effective ECM fibrillogenesis. Representative western blot of β5-integrin (**A**) and α_5-integrin (**C**) expression in desmoplastic fibroblasts (CAFs), illustrating the result of CRISPR/CAS9-mediated KO of integrins (A — β5-KO1 + β5-KO2 and C — α_5-integrin α_5-KO1 + α_5-KO2) compared to non-targeting gRNA control (cntrl-KO). Histone three was used as a loading control. Representative confocal microscopy images of either control CAF-KO (cntrl-KO) or CAF-β5-integrin-KO2 (β5-KO2) (**B**) or CAF-α_5-integrin-KO2 (α_5-KO2) (**D**), depicting αSMA (white) and nuclei (yellow). Inserts show the image-matching ECM fibers (fibronectin, magenta). The images on the right show the corresponding ECM fiber angle distributions as obtained using the Image-J's 'OrientationJ' plug. (**E**) Quantification of the distribution of fiber angles that are within 15° of the mode from (**B**) (****$p<0.0001$). Note that α_5-KO2 CAFs did not produce matrices that were substantial enough for quantification and were therefore omitted from (**E**).

DOI: 10.7554/eLife.20600.020

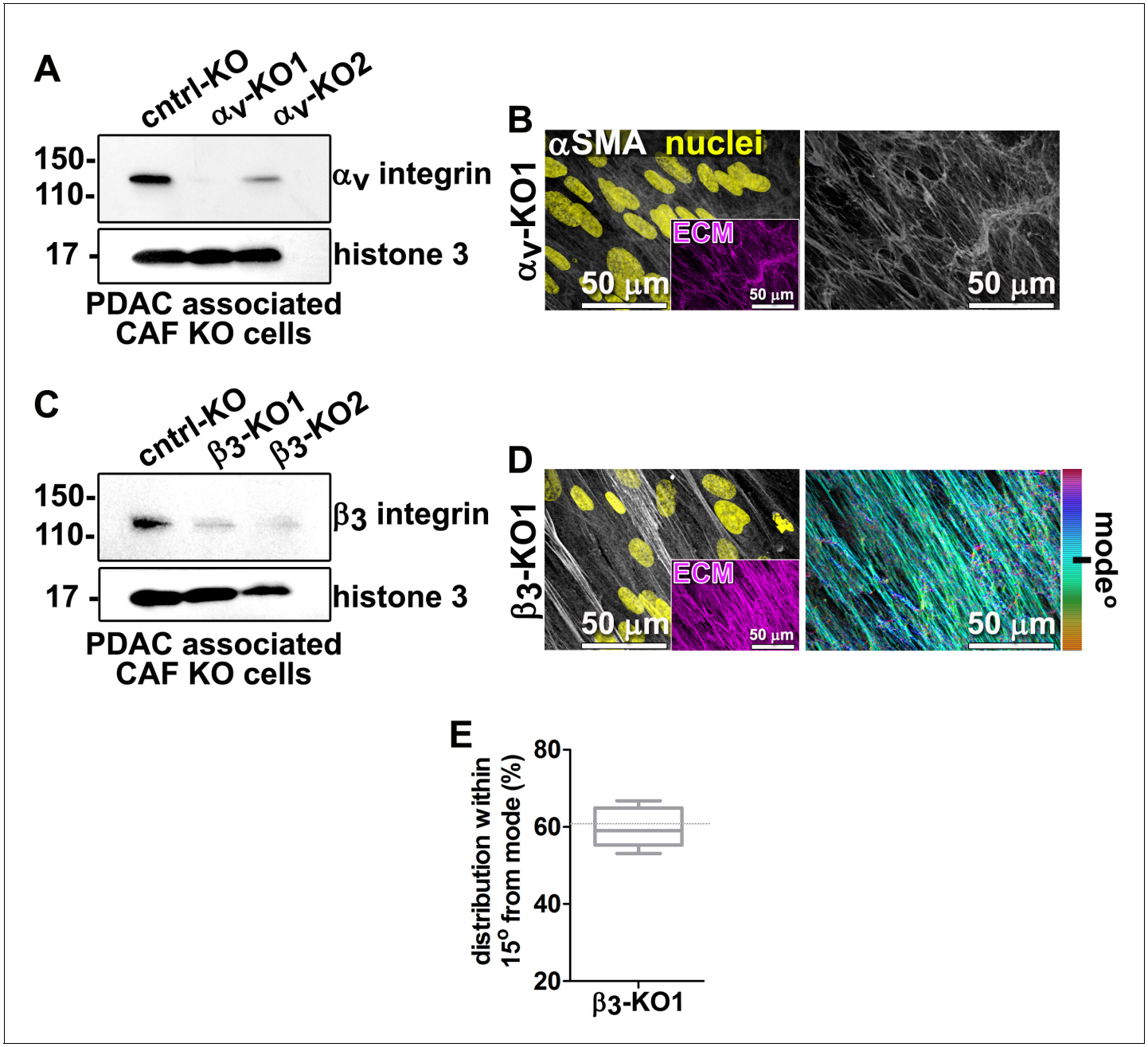

Figure 4—figure supplement 3. KO of α_V-integrin, but not β3-integrin, disrupts CAF myofibroblastic features and D-ECM production. Representative western blots of α_V-integrin (**A**) and β3-integrin (**C**) expression in CAFs, illustrating the result of CRISPR/CAS9 editing of α_V-integrin (α_V-KO1 + α_V-KO2) (**A**) and β3-integrin (β3-KO1 + β3-KO2) (**C**) compared to non-targeting, gRNA, control (cntrl-KO). Histone three was used as a loading control. Representative confocal microscopy images of CAF-α_V-integrin-KO1 (α_V-KO1) (**B**) and CAF-β3-integrin-KO1 (β3-KO2) (**D**) depicting αSMA (white) or nuclei (yellow). Inserts show the image-matching ECM fibers (fibronectin, magenta). The images on the right are the corresponding ECMs, which for α_V-KO1 was not substantial enough to pass the quality thickness test and was therefore omitted from further assessment; for β_3-KO2, ECM fiber angle distributions shown by pseudocoloring were obtained using Image-J's 'OrientationJ' plug in. (**E**) Quantification of the distribution of fiber angles that are within 15° of the mode shown in (**D**). The dotted line corresponds to the percentage of fiber alignment seen in control KO.

DOI: 10.7554/eLife.20600.021

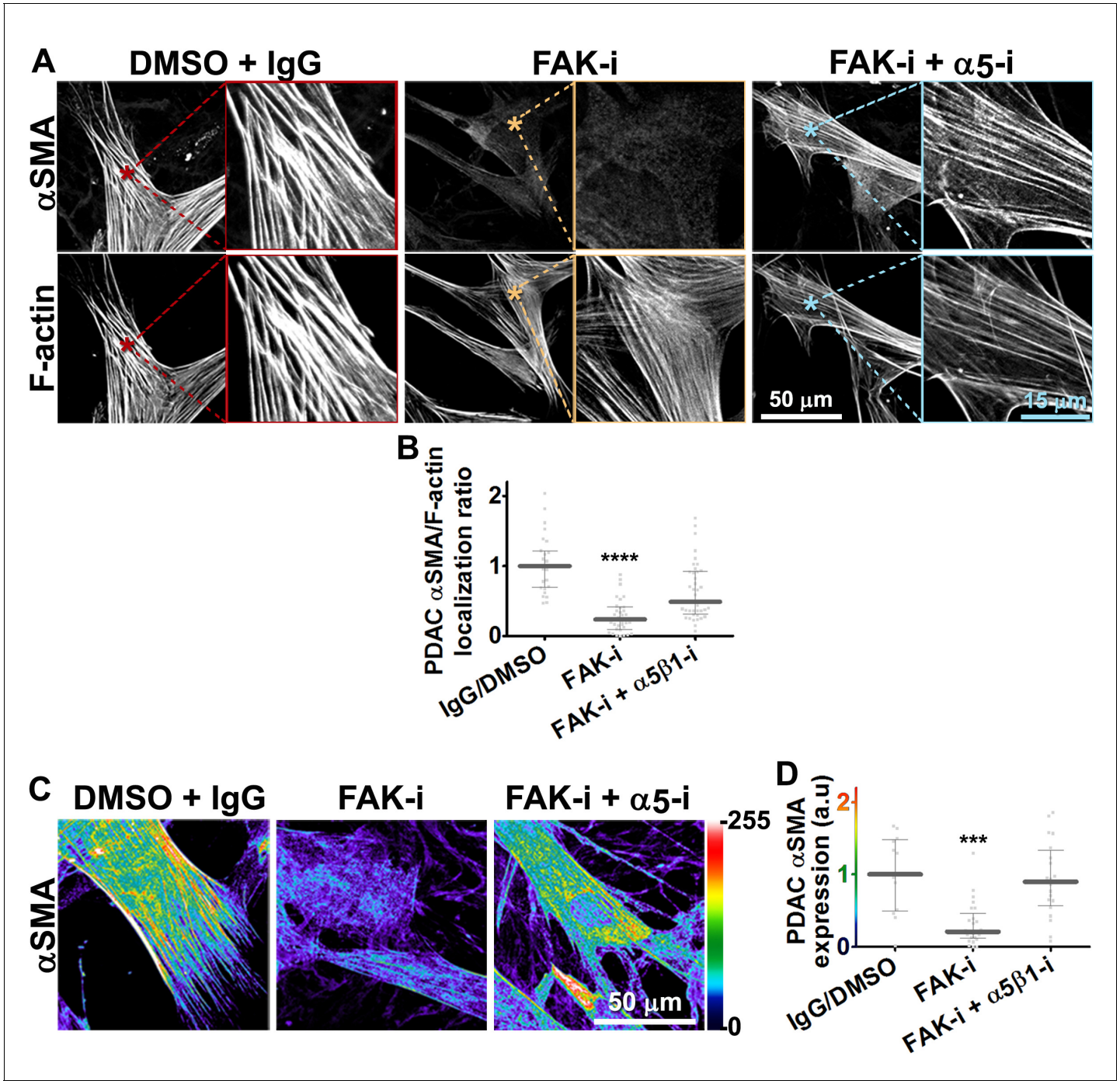

Figure 5. FAK-independent $\alpha_5\beta_1$-integrin activity negatively regulates PDAC D-ECM-induced naïve-to-myofibroblastic activation. Naïve fibroblasts were re-plated onto D-ECMs and challenged with either control conditions (DMSO + IgG), small molecule FAK inhibitor PF573,228 (***Slack-Davis et al., 2007***) (FAK-i) alone or FAK inhibitor in combination with $\alpha_5\beta_1$-integrin inhibitor (FAK-i + α_5-i, mAb16 [***Akiyama et al., 1989***]), and activation of fibroblasts was tested. (**A**) Representative monochromatic images of immunofluorescently labeled αSMA and actin stress fibers (F-actin). Colored asterisks in (**A**) represent areas that are magnified in the corresponding panels to the right. (**B**) Quantification of αSMA at actin stress fibers (F-actin) from the experiment in (**A**) and normalized to DMSO + IgG control (one arbitrary unit; a.u.) (****p<0.0001). (**C**) Pseudocolored images represent intensity maps of αSMA, with an intensity color bar scale (0–255 intensity tone values) shown to the right. (**D**) Quantification of αSMA intensity from (**C**) (***p=0.0001). Note that the D-ECM-induced phenotype that was lost under FAK inhibition was rescued under $\alpha_5\beta_1$-integrin co-inhibition (just as for the two integrin co-inhibitions shown in ***Figure 3***).

DOI: 10.7554/eLife.20600.022

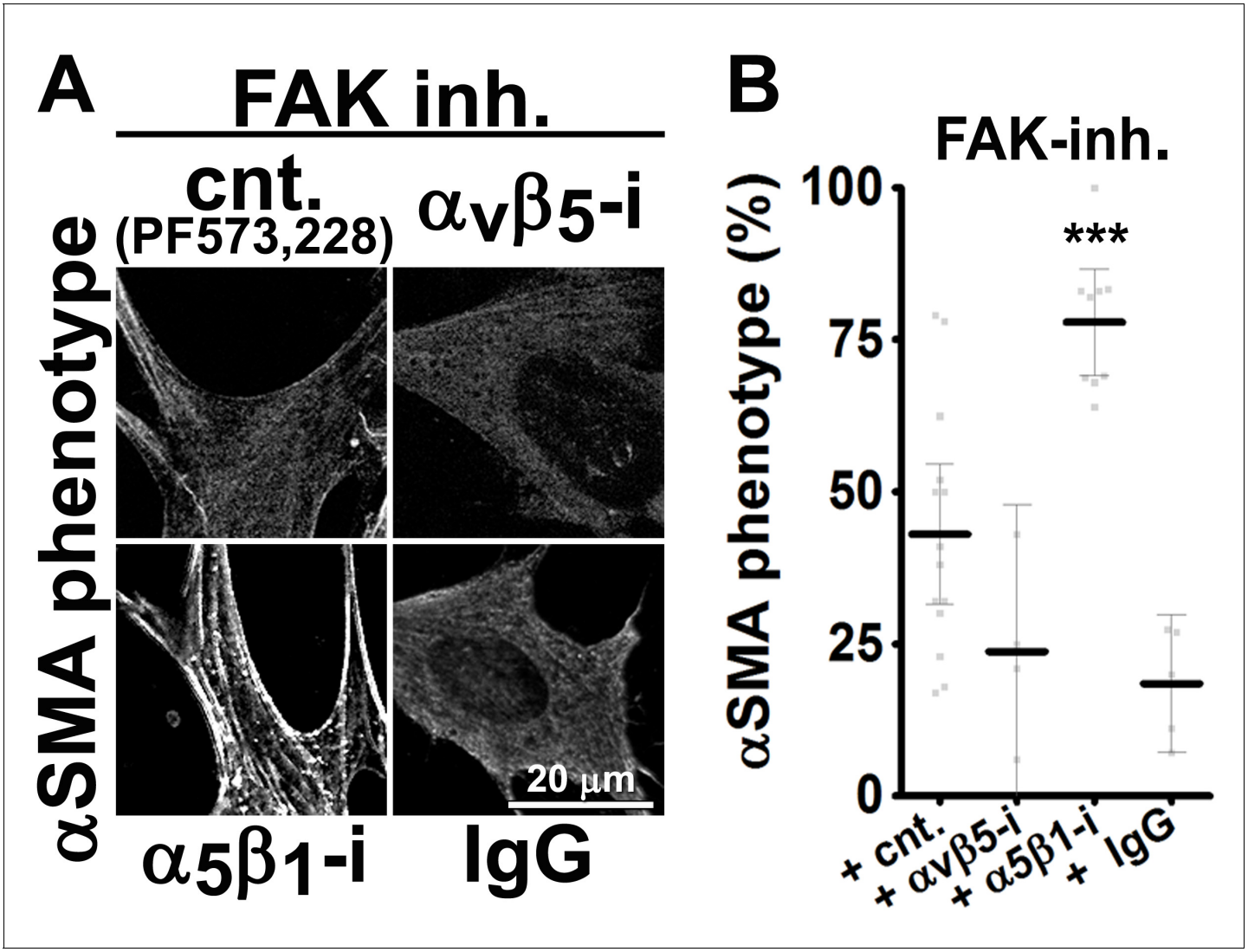

Figure 5—figure supplement 1. FAK-independent $\alpha_5\beta_1$-integrin activity negatively regulates mD-ECM-induced murine naïve-to-myofibroblastic activation. Naïve murine skin fibroblasts were re-plated onto murine D-ECMs (***Amatangelo et al., 2005***) (mD-ECM) and were treated with PF573,228 (FAK inhibitor) and also subjected to $\alpha_v\beta_5$-integrin or $\alpha_5\beta_1$-integrin inhibitors (ALULA — $\alpha_v\beta_5$-i (***Su et al., 2007***) or BMA5 — $\alpha_5\beta_1$i) or IgG control. The effects on naïve-to-myofibroblastic activation were measured in all treated PF573,228 conditions by indirect immunofluorescence of αSMA expression. (**A**) Representative monochromatic images of stress fiber localized αSMA. (**B**) Quantification of the percentage of cells showing myofibroblastic features (stress fiber localized αSMA phenotype %) during the experiment illustrated in (**A**) (***p=0.0001). Note that co-inhibition of FAK and $\alpha_5\beta_1$-integrin effectively reinstituted the mD-ECM-induced phenotype lost as a result of FAK inhibition alone (cnt), just as in the human PDAC stroma system (***Figure 5***) and as was the case for the two integrin co-inhibitions shown in ***Figure 3***.

DOI: 10.7554/eLife.20600.023

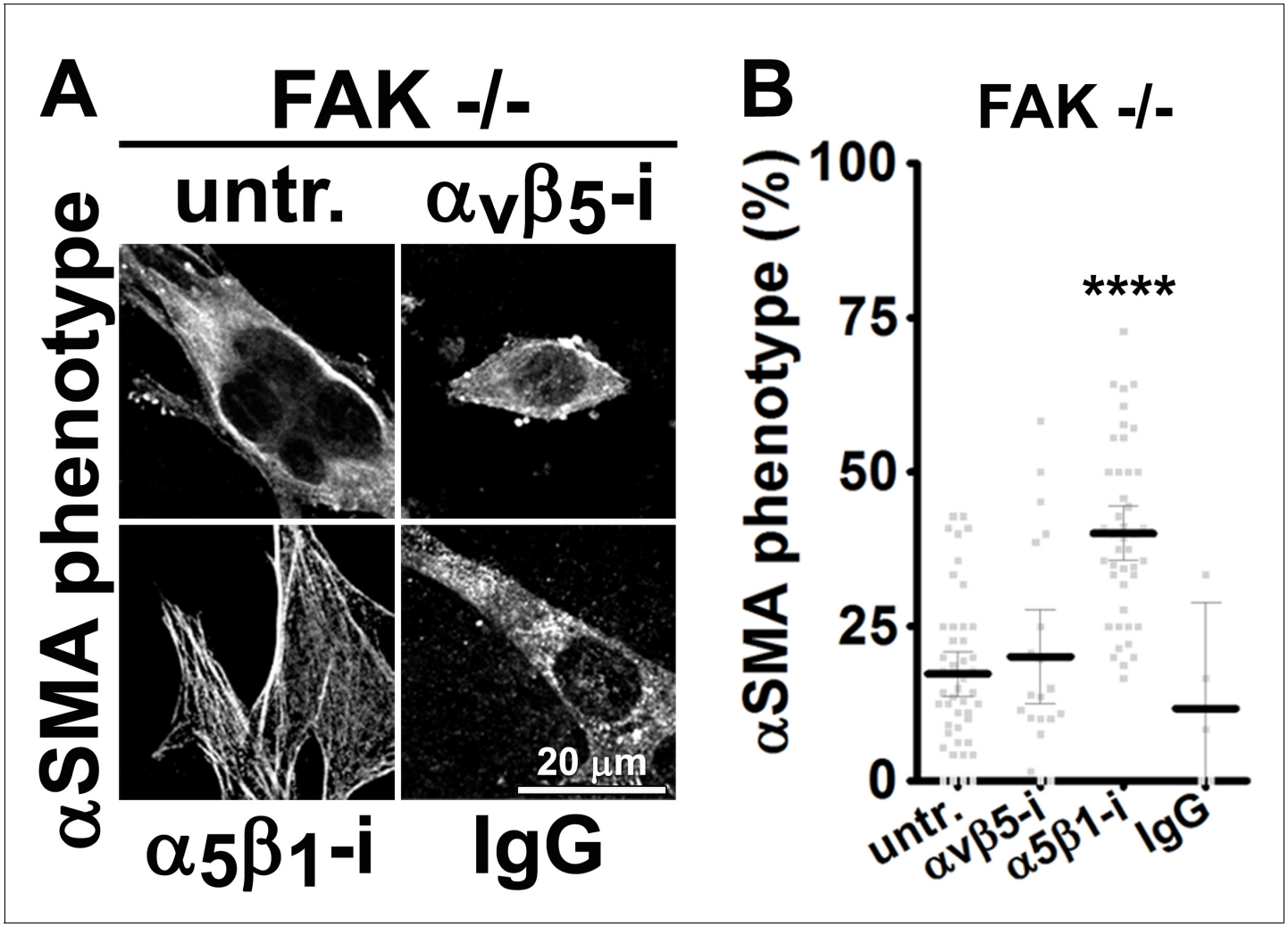

Figure 5—figure supplement 2. $\alpha_5\beta_1$-integrin inhibition restores mD-ECM-induced naïve-to-myofibroblastic activation in murine FAK$^{-/-}$ skin fibroblasts. FAK null (FAK -/-) naïve murine skin fibroblasts were re-plated onto murine D-ECMs (mD-ECM) subjected to $\alpha_v\beta_5$-integrin and $\alpha_5\beta_1$-integrin inhibitors (ALULA — $\alpha_v\beta_5$-i [***Su et al., 2007***] or BMA5 — $\alpha_5\beta_1$i). The effects on myofibroblastic activation were measured by indirect immunofluorescence of αSMA expression as before. (**A**) Representative monochromatic images of αSMA expression. (**B**) Quantification of the percentage of cells showing myofibroblastic features (stress fiber localized αSMA phenotype %) during the experiment illustrated in (**A**) (****p<0.0001). Note that inhibition of $\alpha_5\beta_1$-integrin effectively reinstituted the mD-ECM-induced phenotype that was lost as a result of FAK deletion.

DOI: 10.7554/eLife.20600.024

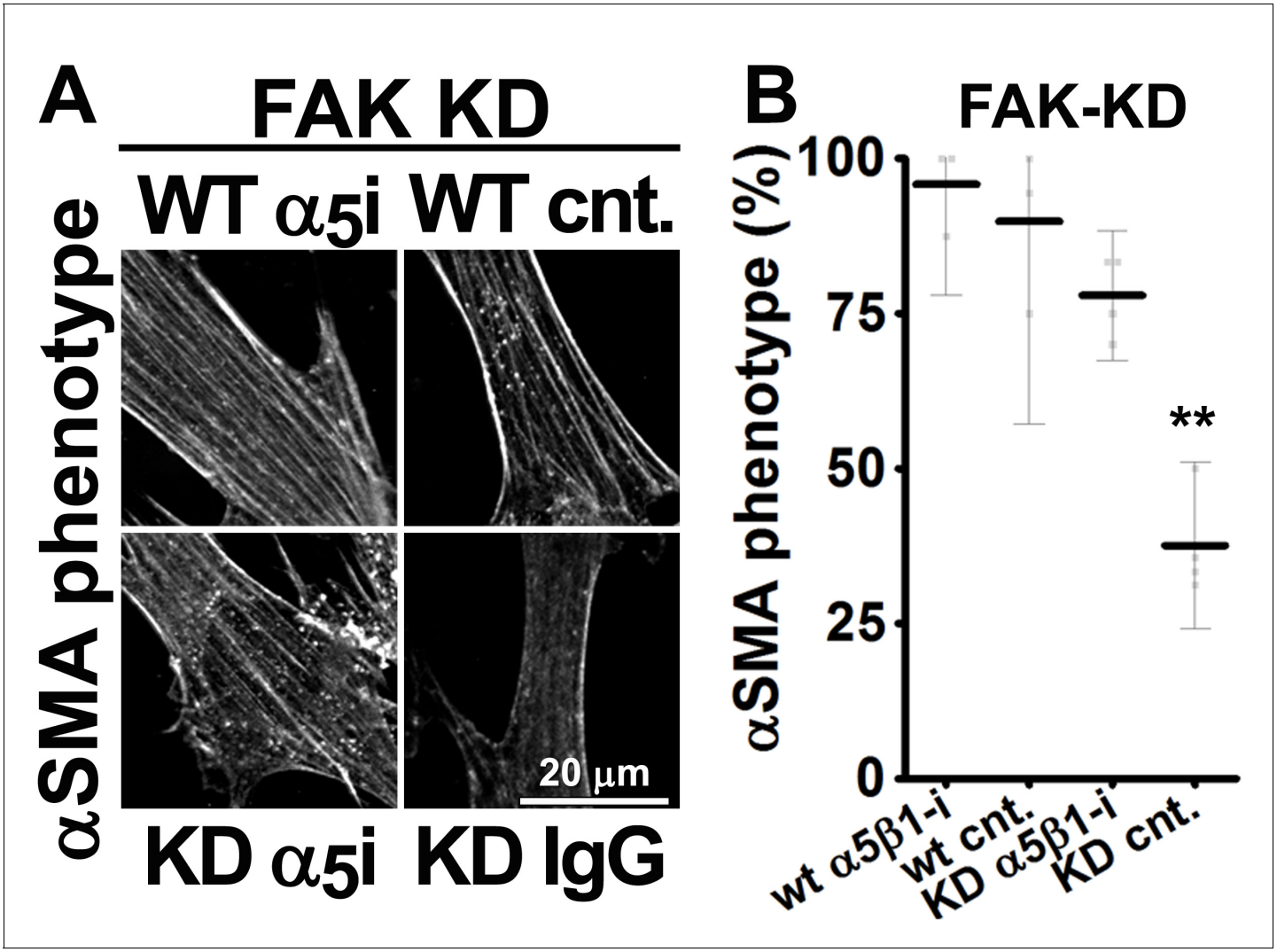

Figure 5—figure supplement 3. $\alpha_5\beta_1$-integrin inhibition restores mD-ECM-induced naïve-to-myofibroblastic in murine FAK-KD skin fibroblasts. Wild-type (WT) or FAK kinase dead (KD) naïve murine skin fibroblasts were re-plated onto murine D-ECMs (mD-ECM) and subjected to $\alpha_5\beta_1$-integrin inhibitor (BMA5 — WT α_5i or KD α_5i) or IgG control (WT cnt and KD IgG)). The effects on myofibroblastic activation were measured by indirect immunofluorescence of αSMA expression. (**A**) Representative monochromatic images of αSMA expression. (**B**) Quantification of the percentage of cells showing myofibroblastic features (stress fiber localized αSMA phenotype %) during the experiment illustrated in (**A**). Note that inhibition of $\alpha_5\beta_1$-integrin effectively reinstituted the mD-ECM-induced phenotype that was lost as a result of FAK KD mutation.

DOI: 10.7554/eLife.20600.025

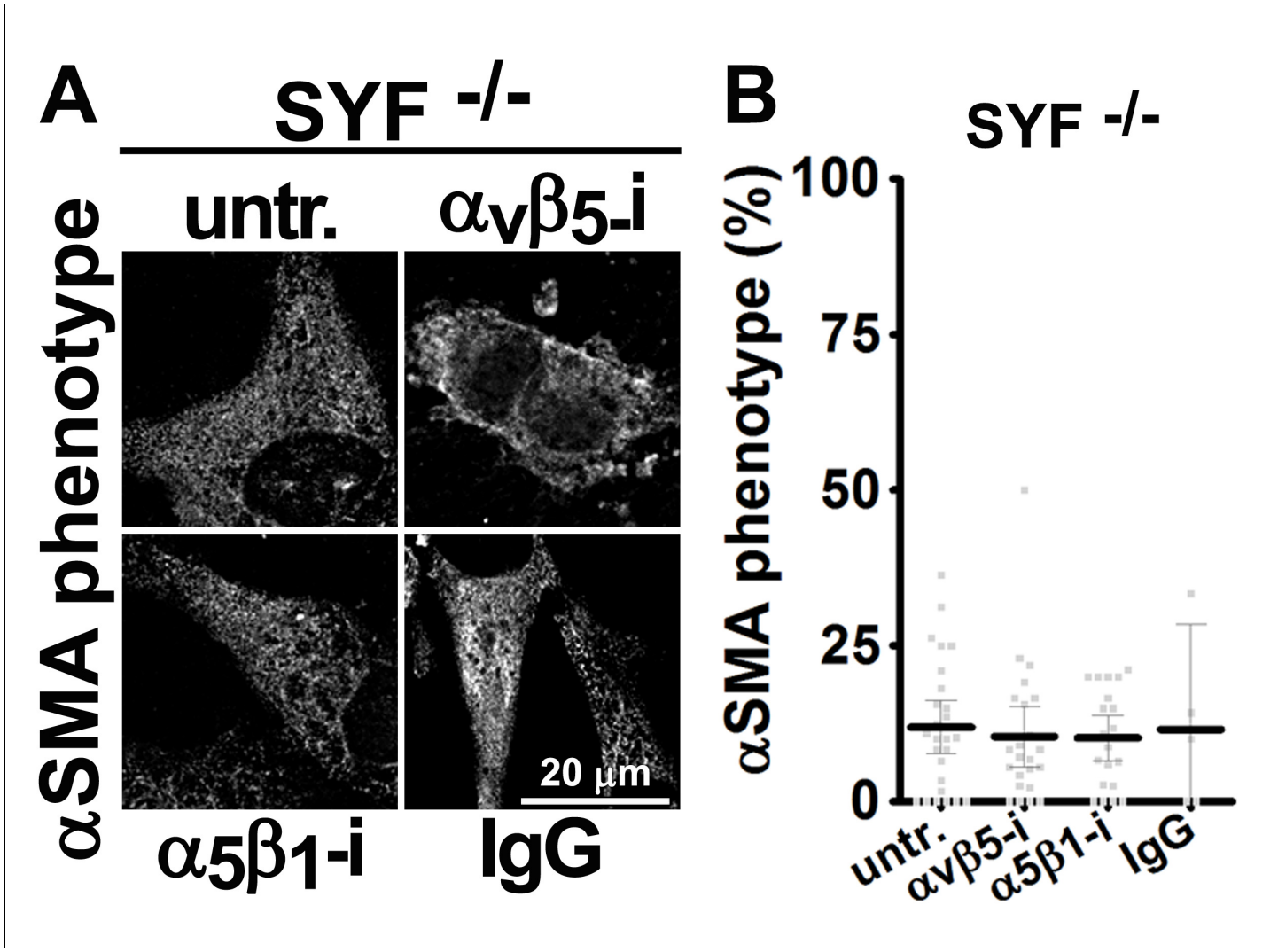

Figure 5—figure supplement 4. Ablation of SRC family kinases negates the ability of naïve fibroblasts to respond to mD-ECM. SRC naïve murine skin fibroblasts lacking SRC, YES and FYN (SYF -/-) were re-plated onto murine D-ECMs (mD-ECM) and $\alpha_v\beta_5$-integrin and $\alpha_5\beta_1$-integrin inhibitors (ALULA — $\alpha_v\beta_5$-i [***Su et al., 2007***] and BMA5 — $\alpha_5\beta_1$i) or IgG control (IgG). The effects on myofibroblastic activation were measured by indirect immunofluorescence of αSMA expression. (**A**) Representative monochromatic images of αSMA expression. (**B**) Quantification of the percentage of cells showing myofibroblastic features (stress fiber localized αSMA phenotype %) during the experiment illustrated in (**A**). Note that inhibition of $\alpha_5\beta_1$-integrin could not reinstitute the mD-ECM-induced phenotype that was lost in $SRC^{-/-}$ cells.

DOI: 10.7554/eLife.20600.026

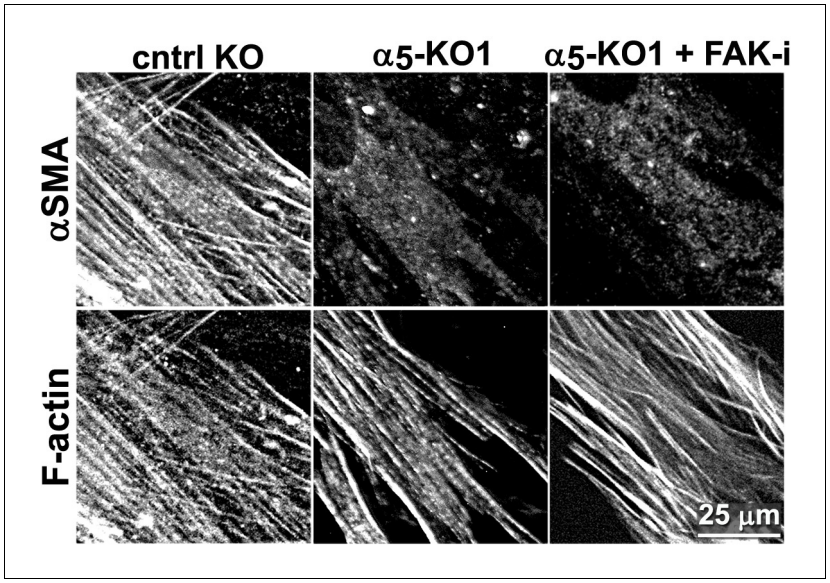

Figure 5—figure supplement 5. FAK inhibition in conjunction with loss of α_5-integrin expression in human naïve fibroblasts fails to restore D-ECM-induced myofibroblastic activation. Naïve fibroblastic stellate control KO (cntrl-KO) or α_5-integrin (α_5-KO) cells were re-plated within intact D-ECMs and challenged with DMSO as control or with the small molecule FAK inhibitor PF573,228 (***Slack-Davis et al., 2007***) (FAK-i), and the activation of fibroblasts was tested. Representative monochromatic images of αSMA and actin stress fibers (F-actin) were immunofluorescently labeled and are shown. Note that unlike $\alpha_5\beta_1$-integrin inhibition with mAb16, loss of α_5-integrin expression did not rescue the myofibroblastic phenotype.
DOI: 10.7554/eLife.20600.027

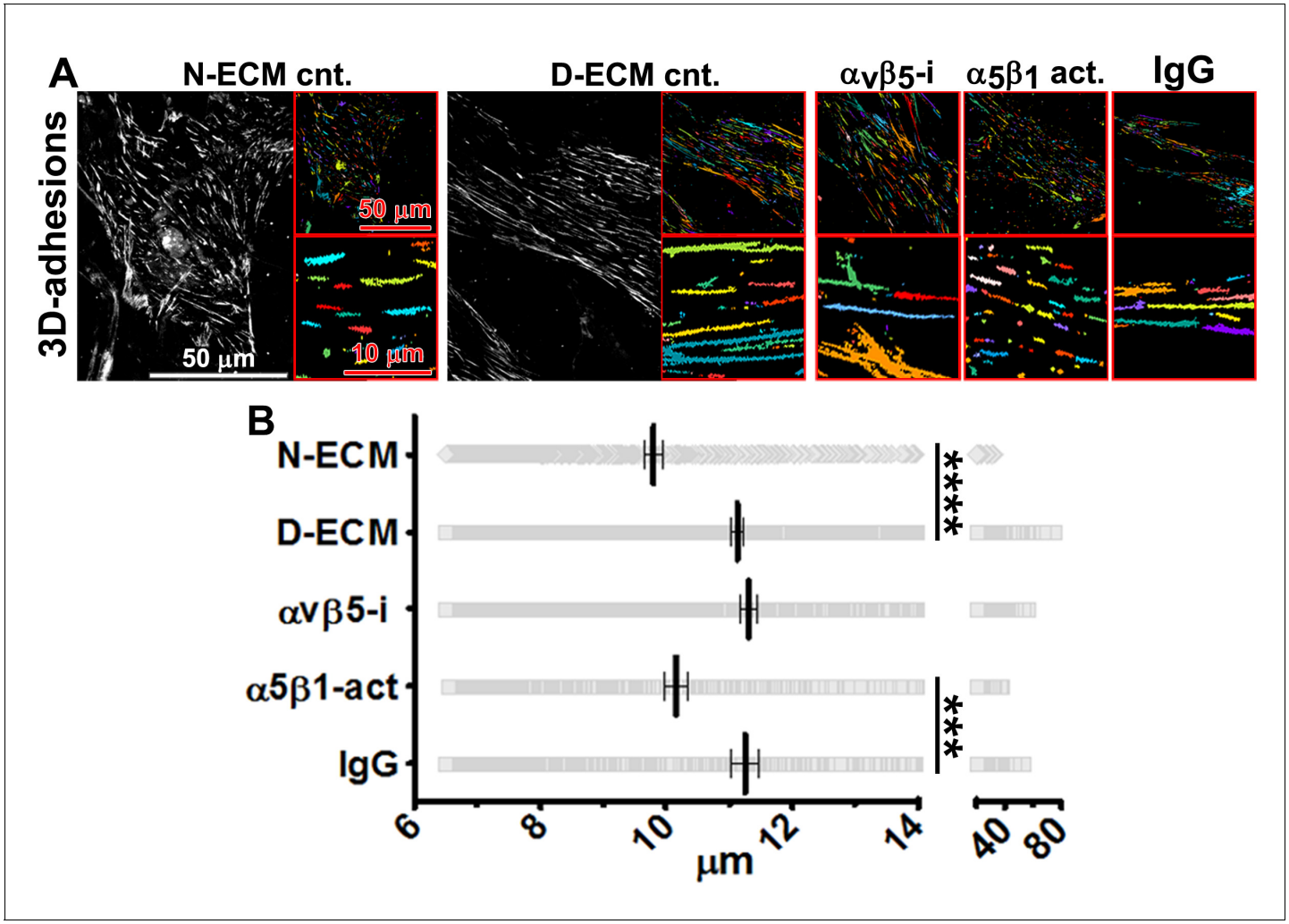

Figure 6. D-ECM regulates 3D-adhesion structure length, dependent on $\alpha_5\beta_1$-integrin activity. (**A**) Indirect immunofluorescent and spinning disc confocal generated images of 3D-adhesions (identified using mAb11) (***Cukierman et al., 2001***), formed by naïve fibroblastic cells cultured within N-ECM or D-ECM in the absence (cnt.) or presence of ALULA (***Su et al., 2007***) for $\alpha_v\beta_5$-integrin inhibition ($\alpha_v\beta_5$-i) or SNAKA52 (***Clark et al., 2005***) to stabilize $\alpha_5\beta_1$-integrin activity ($\alpha_5\beta_1$ act) or IgG as control. (A) The artificially colored structures represent computer-selected internally threshold objects (ITOs) of 3D-adhesion structures. (**B**) Quantification of the length of ITO generated objects from (**A**) (***p=0.0026. ****p<0.0001). Note the significant differences in 3D-adhesion length observed between N-ECM and D-ECM as well as between IgG and SNAKA51 treatments.

DOI: 10.7554/eLife.20600.028

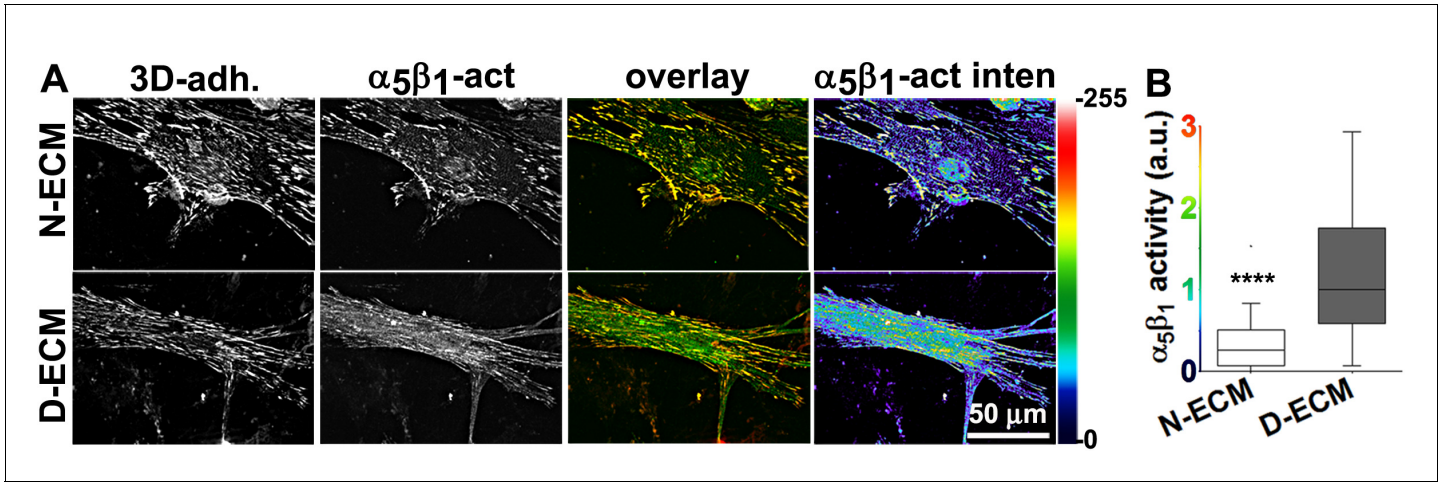

Figure 6—figure supplement 1. Naïve fibroblastic cells increase overall levels of active $\alpha_5\beta_1$-integrin in response to D-ECM. (**A**) Double-labeled images depicting 3D-adhesion (red in overlay; 3D-adh.) and active $\alpha_5\beta_1$-integrin (green in overlay; $\alpha_5\beta_1$-act) in naïve fibroblasts cultured overnight in normal-ECMs (N-ECM) or desmoplastic-ECMs (D-ECM). The pseudocolored images on the far right represent semi-quantitative images of maximum reconstructions of active $\alpha_5\beta_1$-integrin levels ($\alpha_5\beta_1$-act inten), with a corresponding intensity bar shown on the right. (**B**) Summary of total active $\alpha_5\beta_1$-integrin levels using median levels on D-ECM for normalization (one arbitrary unit; a.u.) (****$p<0.0001$).

DOI: 10.7554/eLife.20600.029

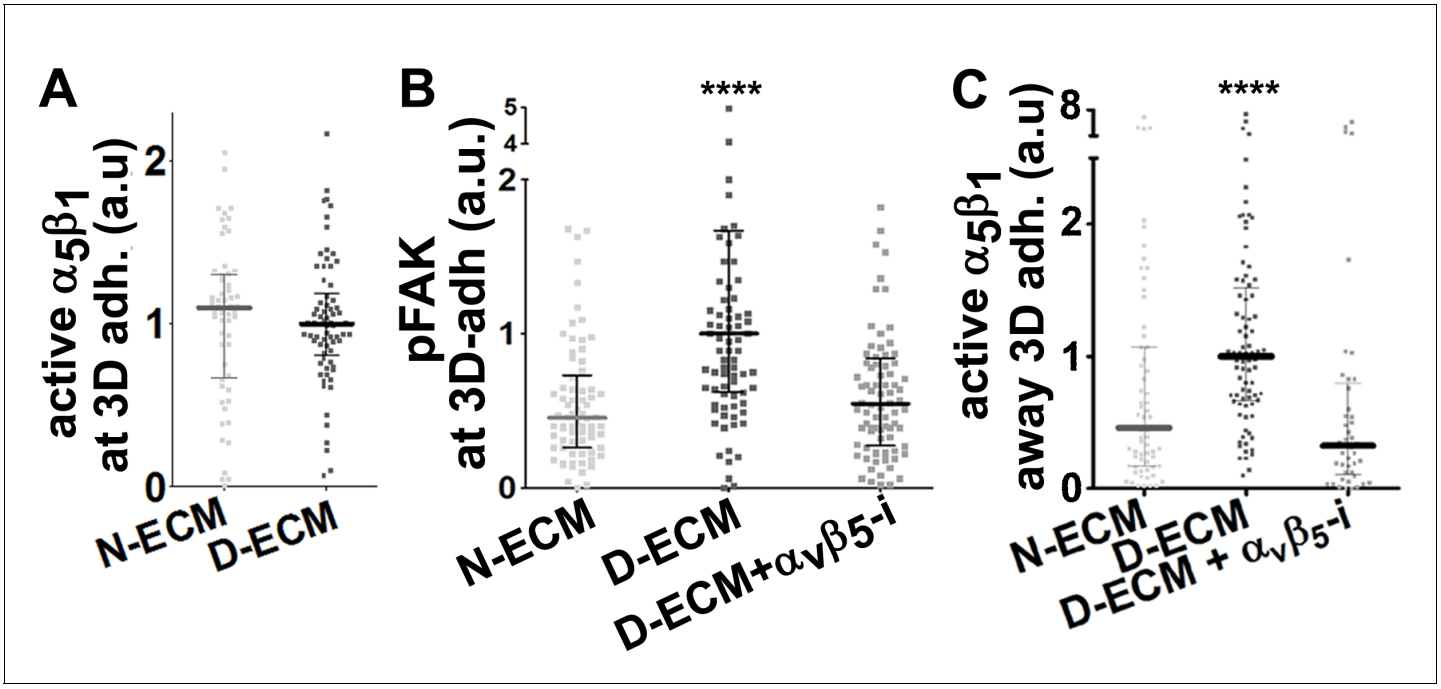

Figure 6—figure supplement 2. D-ECMs induce an increase in pFAK levels at 3D-adhesions and redistribution of increased active $\alpha_5\beta_1$-integrin to locations away from 3D-adhesions. Naïve fibroblasts were cultured within assorted ECMs in the absence (N-ECM or D-ECM) or presence of $\alpha_v\beta_5$-integrin inhibitor ALULA (***Su et al., 2007***) (D-ECM + $\alpha_v\beta_5$-i) and were stained for adhesion structures, pFAK, and active $\alpha_5\beta_1$-integrin and the images were quantified. (**A**) Graph depicting active $\alpha_5\beta_1$-integrin levels localized at 3D-adhesions, normalized to D-ECM median intensities, calculated using SMIA-CUKIE publicly available at https://github.com/cukie/SMIA. (**B**) Graph depicting levels of pFAK-Y^{397}, calculated using SMIA-CUKIE, localized at 3D-adhesions structures (****p<0.0001). (**C**) Graph showing active $\alpha_5\beta_1$-integrin intensity values, normalized to D-ECM mean intensities and calculated using SMIA-CUKIE, that are localized away from 3D-adhesions (****p<0.0001). Note that the D-ECM-induced increases in active $\alpha_5\beta_1$-integrin, which are evident at locations away from 3D-adhesions, are concomitant with increased 3D-adhesion localized pFAK.

DOI: 10.7554/eLife.20600.030

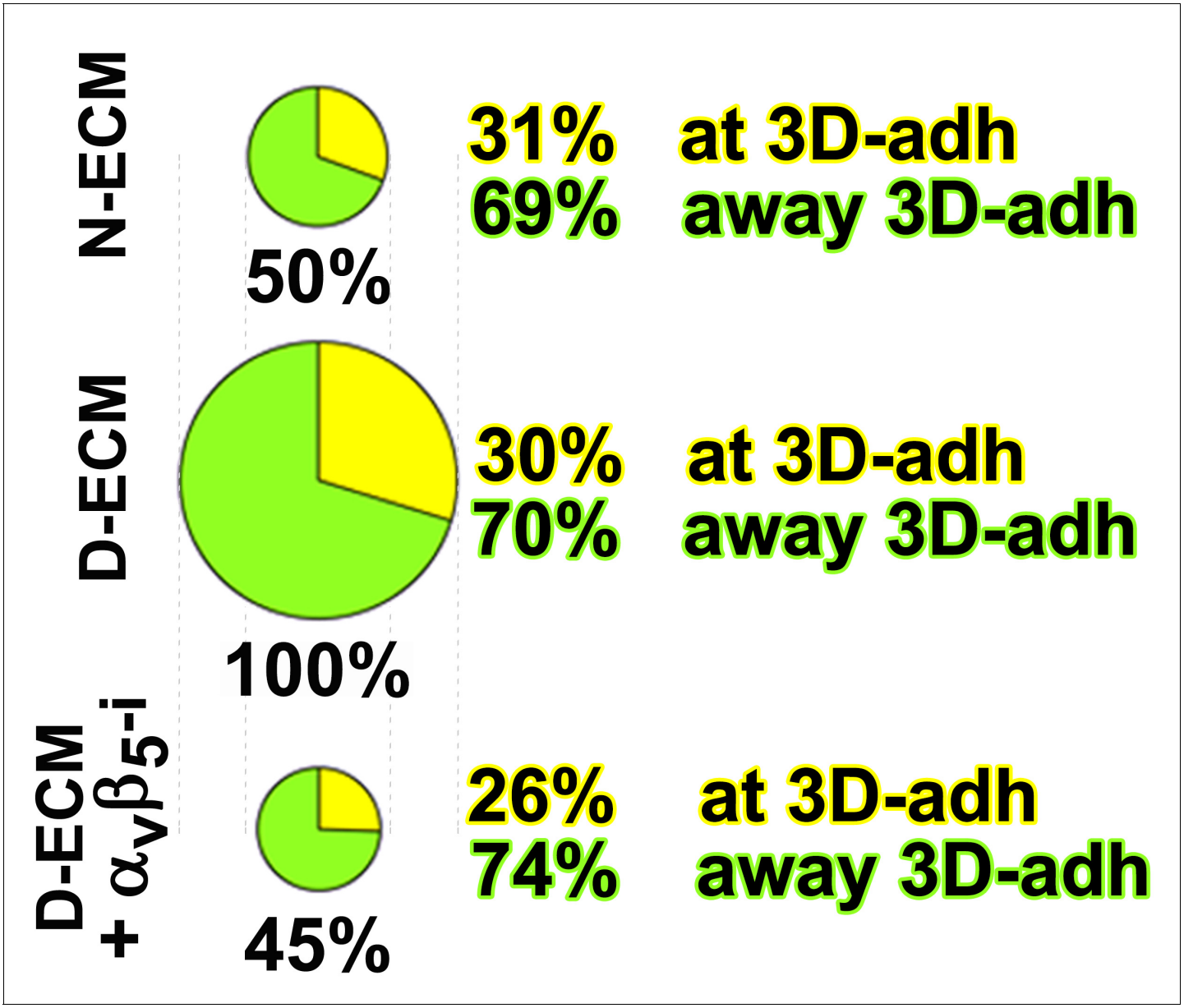

Figure 6—figure supplement 3. D-ECM-induced increase in active $\alpha_5\beta_1$-integrin is reversed by inhibition of $\alpha_v\beta_5$-integrin. Summary of results from naïve fibroblasts cultured within assorted ECMs in the absence (N-ECM or D-ECM) or presence of $\alpha_v\beta_5$-integrin inhibitor ALULA (***Su et al., 2007***) (D-ECM + $\alpha_v\beta_5$-i) and stained for adhesion structures and active $\alpha_5\beta_1$-integrin. The sizes of pie graphs are relative to SMIA-CUKIE output corresponding to total intensity levels, while relative percentage distributions at 3D-structures (yellow) and away from these structures (light green) are shown. Note that the percentage distributions between locations at and away from 3D-adhesions are relatively unchanged while total intensity levels of active integrin are increased in response to D-ECM.

DOI: 10.7554/eLife.20600.031

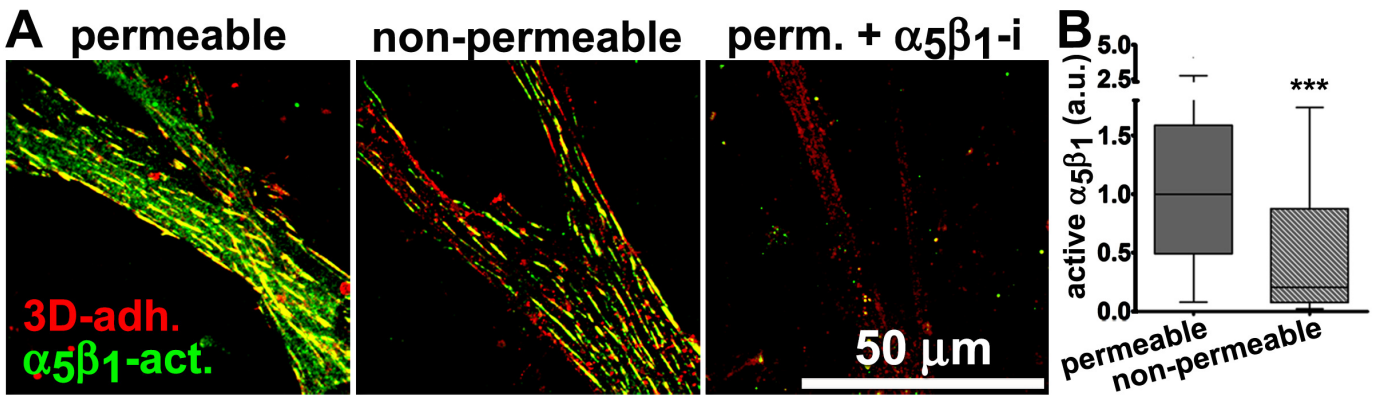

Figure 6—figure supplement 4. D-ECM induces intracellular accumulation of active $\alpha_5\beta_1$-integrin. Naïve cells were plated overnight within D-ECM. (**A**) Indirect immunofluorescent images of active $\alpha_5\beta_1$-integrin ($\alpha_5\beta_1$-act.; SNAKA51 in green) locations relative to 3D-adhesions (3D-adh.; mAb11 in red), showing a representative cell under permeable vs. non-permeable conditions. The third image (on the right)demonstrates the specificity of active $\alpha_5\beta_1$-integrin detection when samples were treated with functional blocking anti-$\alpha_5\beta_1$-integrin antibody, mAb16, under permeable conditions (perm. + $\alpha_5\beta_1$i). (**B**) Graph summarizes permeable vs. non-permeable values of active $\alpha_5\beta_1$-integrin from experimental repetitions in which median permeable intensity levels were used for normalization (one arbitrary unit; a.u.) (***p=0.0005).

DOI: 10.7554/eLife.20600.032

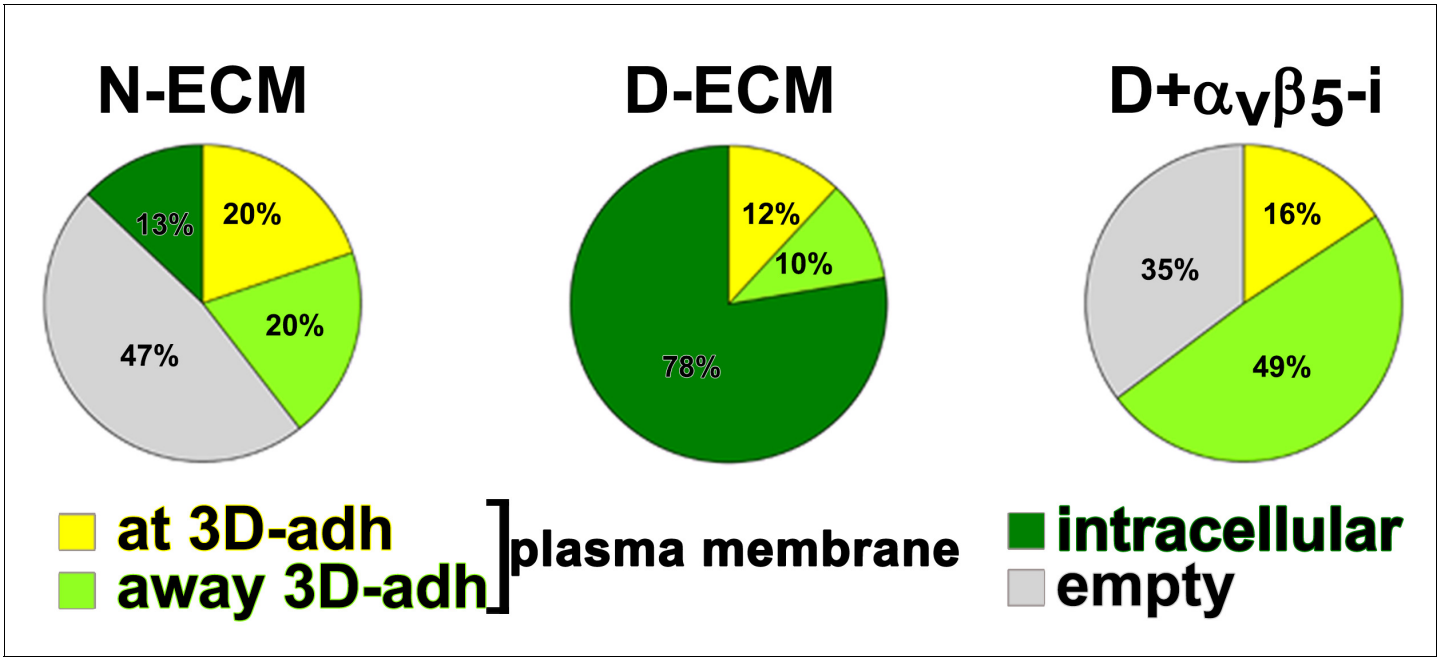

Figure 6—figure supplement 5. D-ECM-induced increase in intracellular $\alpha_5\beta_1$-integrin activity is regulated by $\alpha_v\beta_5$-integrin. Summary of results from naïve fibroblasts cultured within assorted ECMs in the absence (N-ECM or D-ECM) or presence of $\alpha_v\beta_5$-integrin inhibitor ALULA (***Su et al., 2007***) (D-ECM + $\alpha_v\beta_5$-i) and stained, following permeable vs. non-permeable conditions, for adhesion structures and active $\alpha_5\beta_1$-integrin. The pie graphs depict active $\alpha_5\beta_1$-integrin fractions localized exogenously on the PM at (non-permeable conditions; yellow or away from (light green) 3D-adhesions, or intracellularly (dark green). Diminished levels of intracellular active $\alpha_5\beta_1$-integrin are represented by the 'empty' pie wedges (gray). Data were normalized to D-ECM-induced levels obtained under permeable conditions as in ***Figure 6—figure supplements 3–4***.

DOI: 10.7554/eLife.20600.033

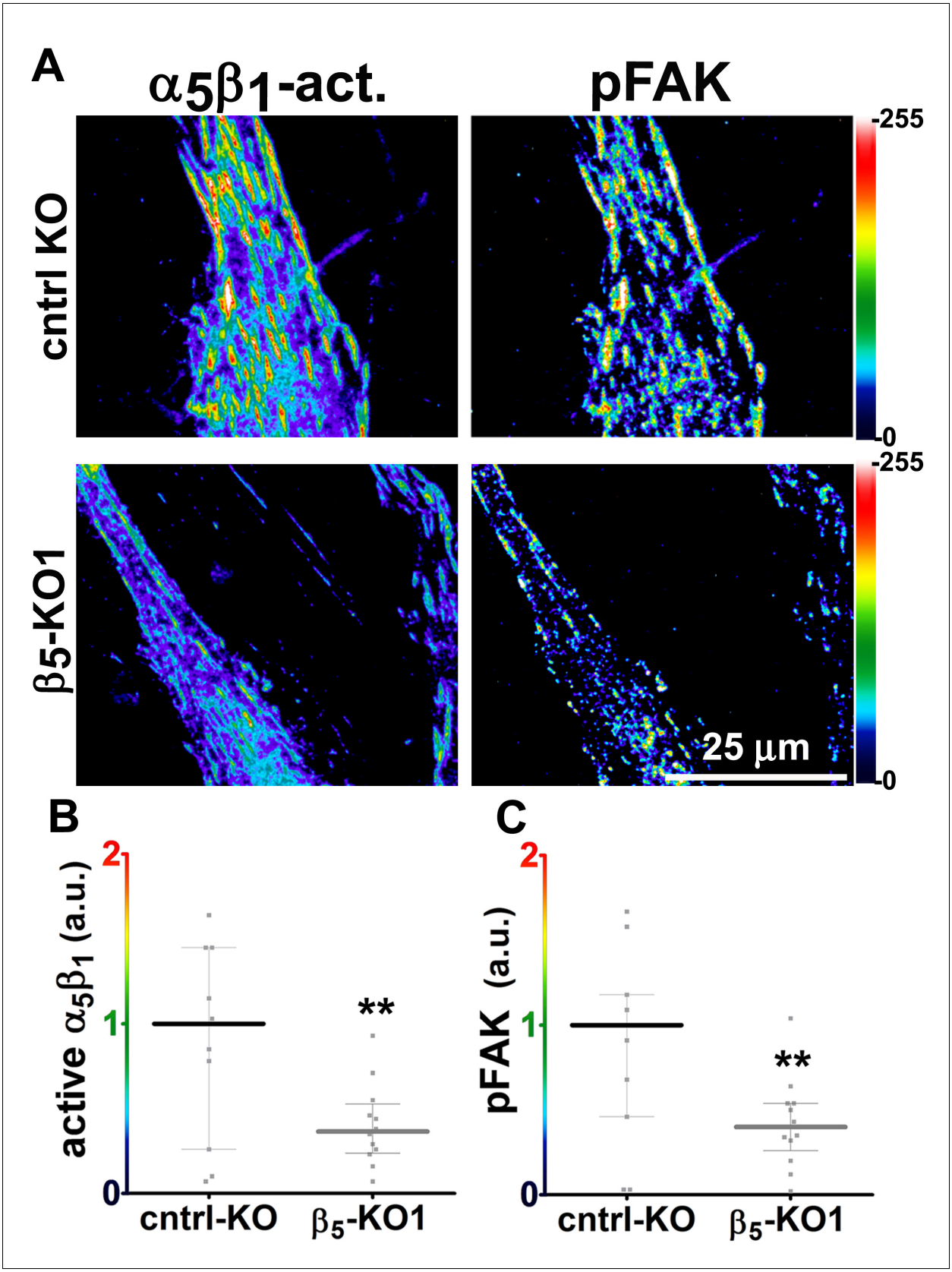

Figure 7. Loss of β5-integrin expression in naïve fibroblasts effectively reduces D-ECM-induced levels of active $\alpha_5\beta_1$-integrin and pFAK-Y^{397}. (**A**) Pseudocolored images showing the intensities of representative indirect immunofluorescence images indicating active $\alpha_5\beta_1$-integrin ($\alpha_5\beta_1$-act.) or pFAK

Figure 7 continued on next page

Figure 7 continued

from control KO (cntrl KO) or β_5-integrin KO (β_5-KO1) naïve fibroblasts. The fibroblasts were cultured overnight within D-ECMs. Intensity scale bars are shown to the right. (**B** and **C**) Quantification of total active $\alpha_5\beta_1$-integrin (**p=0.0420) (**B**) and pFAK-Y^{397} (**p=0.0246) (**C**) levels of cells from (**A**). Note that both activities that were induced by D-ECM in naïve fibroblasts are lost in β_5-integrin KO naïve fibroblastic stellate cells.

DOI: 10.7554/eLife.20600.034

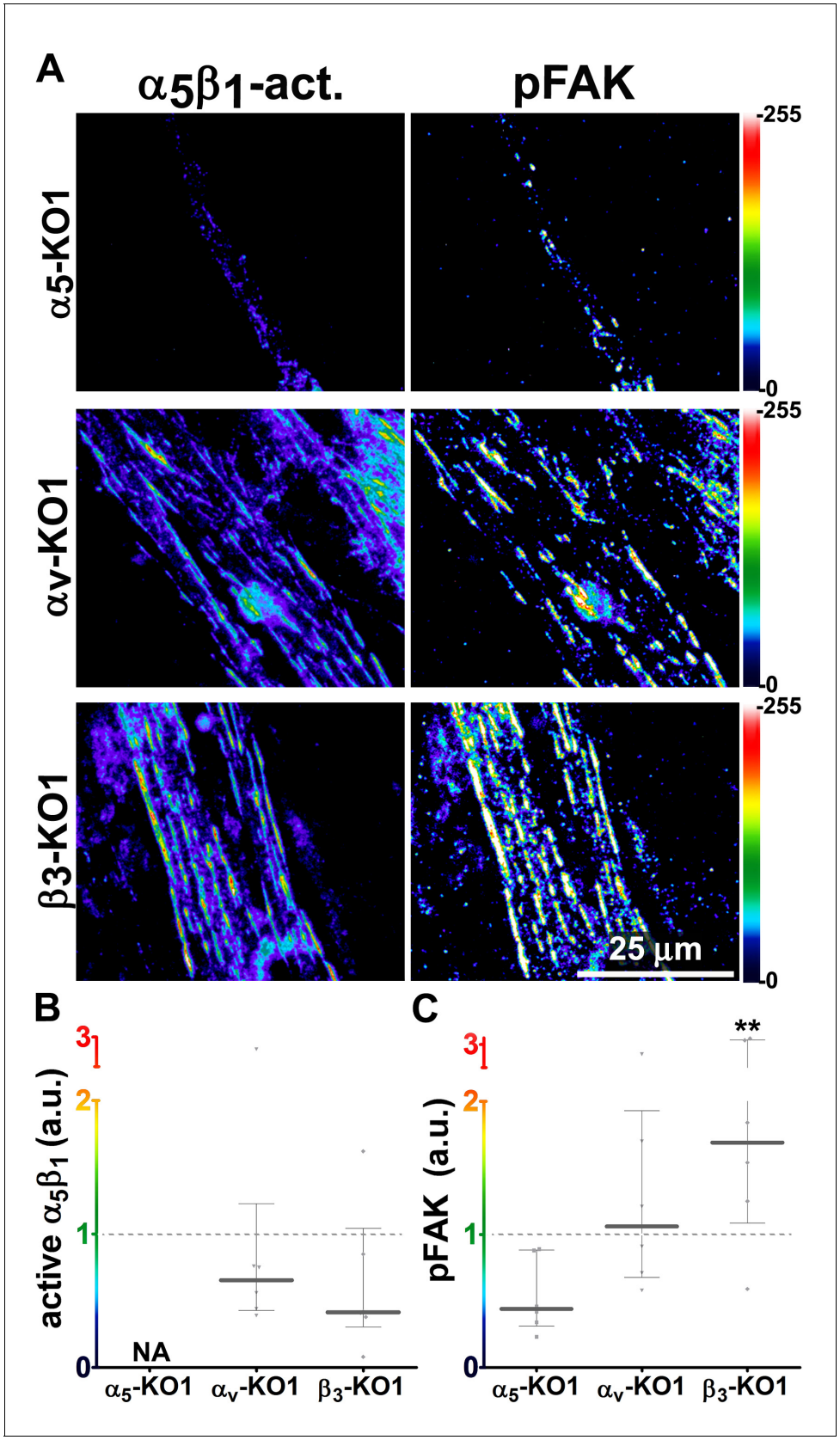

Figure 7—figure supplement 1. Loss of α_V- or β_3-integrins does not significantly reduce overall levels of active $\alpha_5\beta_1$-integrin that is induced by D-ECM in naïve fibroblasts. (**A**) Pseudocolored images showing the intensities of representative indirect immunofluorescence images indicating active $\alpha_5\beta_1$-

Figure 7—figure supplement 1 continued on next page

Figure 7—figure supplement 1 continued

integrin ($\alpha_5\beta_1$-act.) or pFAK from α_5-integrin KO (α_5-KO1), α_V-integrin KO (α_V-KO1) or β_3-integrin KO (β_3-KO1) naïve fibroblasts cultured overnight with D-ECMs. (**B**) Quantification of total active $\alpha_5\beta_1$-integrin levels of cells from (**A**). (**C**) Quantifiction of pFAK levels of cells from (**A** (**p=0.0343). Dotted lines in (**B**) and (denote control KO normalized levels shown in ***Figure 7***.

DOI: 10.7554/eLife.20600.035

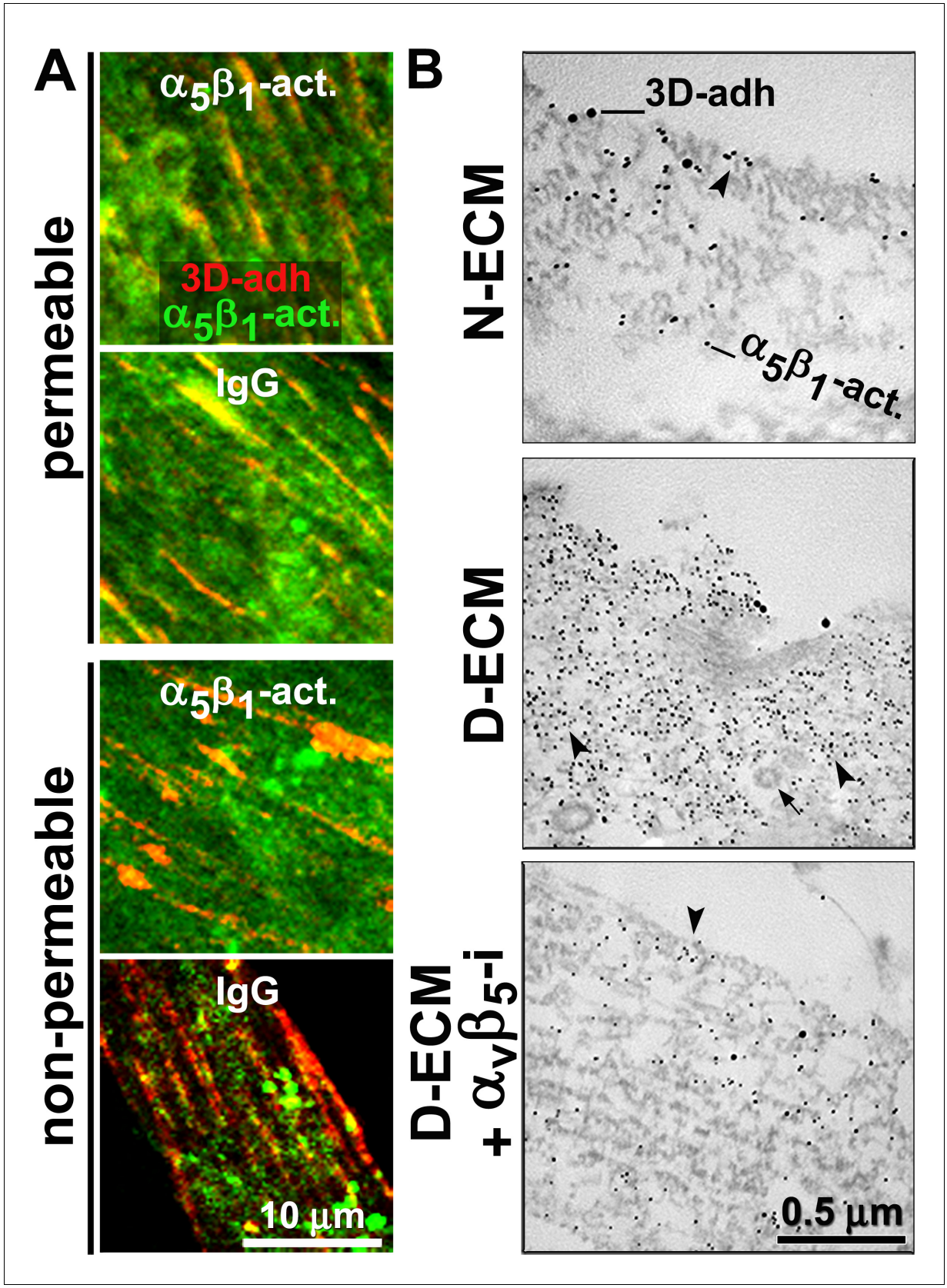

Figure 8. D-ECM prompts the internalization or relocation of $\alpha_5\beta_1$-integrin activity in an $\alpha_v\beta_5$-integrin-dependent manner. (**A**) Representative indirect immunofluorescent images corresponding to overnight 'chase' incubations with pre-labeled anti-active-$\alpha_5\beta_1$-integrin antibodies (SNAKA51 [***Clark et***

Figure 8 continued on next page

Figure 8 continued

al., 2005]) or IgG controls (blue, –not shown), followed by *de novo* detected active $\alpha_5\beta_1$-integrin labeling after fixation ($\alpha_5\beta_1$-act. in green) relative to 3D-adhesion structures (3D-adh. in red) under permeable vs. non-permeable conditions. Note how SNAKA51 treatment but not IgG prompts the relocation of integrin activity to the PM while there is practically no change between permeable and non-permeable active $\alpha_5\beta_1$-integrin levels. (**B**) Transmitted electron microscopy images of double immunogold-labeled 3D-adhesions (–3D-adh. large particles, [***Cukierman et al., 2001***]) vs. active $\alpha_5\beta_1$-integrin (-$\alpha_5\beta_1$-act. small particles, [***Clark et al., 2005***]), detected in naïve cells cultured within N–ECM vs. D-ECM in the presence or absence of $\alpha_v\beta_5$-integrin blockage using ALULA (***Su et al., 2007***) ($\alpha v\beta 5$-i). Both reduction and relocation of active $\alpha_5\beta_1$-integrin pools are observed. Arrowheads point at random immunogold particles as examples, while the closed arrow indicates the location of a clathrin-coated vesicle.

DOI: 10.7554/eLife.20600.036

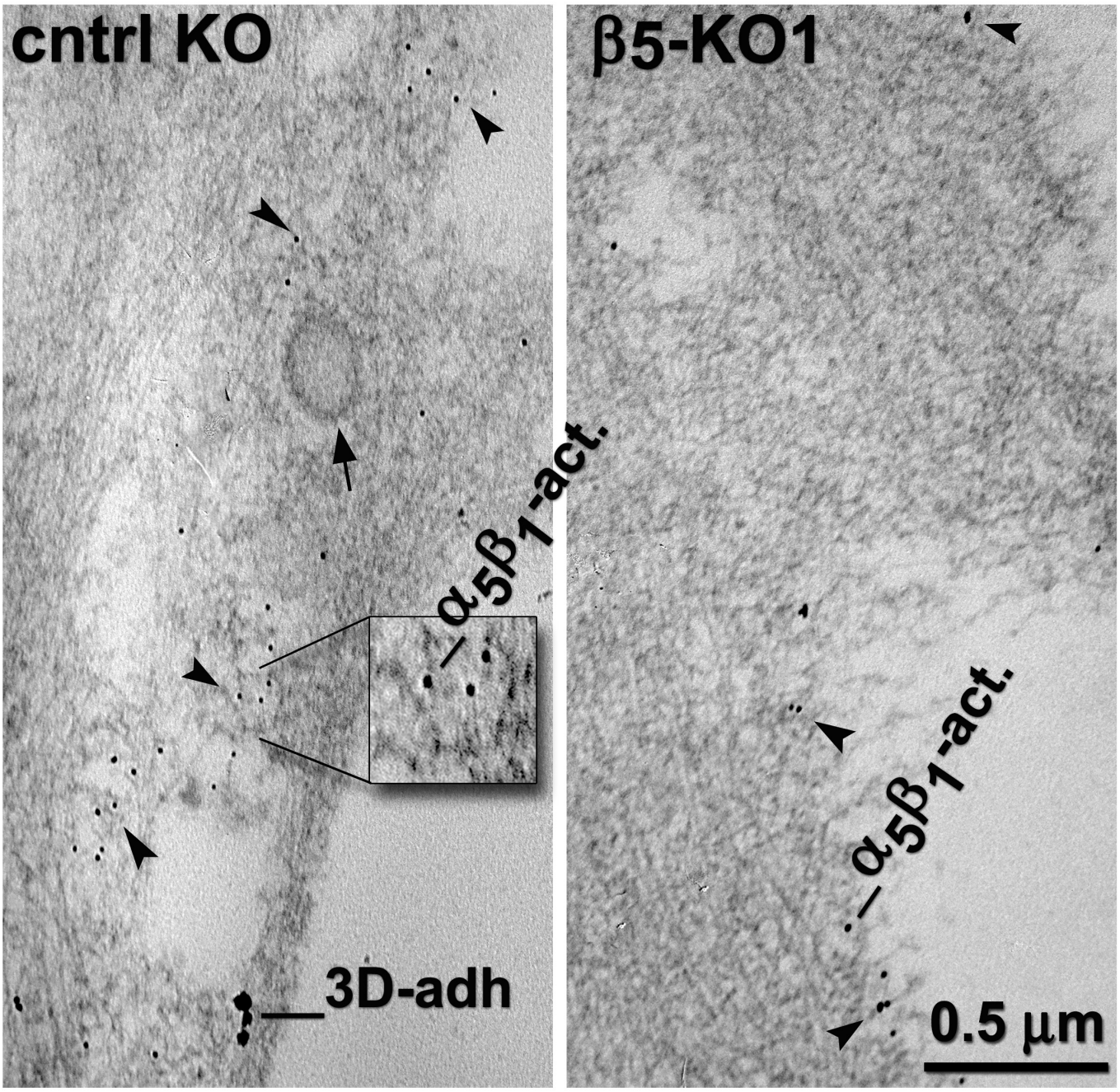

Figure 8—figure supplement 1. KO of β_5-integrin in naïve fibroblasts results in a redistribution of D-ECM-induced active $\alpha_5\beta_1$-integrin from intracellular pools back to the plasma membrane. Transmitted electron microscopy images of double immunogold-labeled 3D-adhesions (–3D-adh. large particles, [***Cukierman et al., 2001***]) vs. active $\alpha_5\beta_1$-integrin (-$\alpha_5\beta_1$-act. small particles, [***Clark et al., 2005***]), detected in naïve control KO (cntrl-KO) or β_5-integrin KO (β_5-KO1) fibroblastic stellate cells cultured within D-ECM. The images show a reduction of the total amounts of active $\alpha_5\beta_1$-integrin and relocation of active $\alpha_5\beta_1$-integrin pools to the PM in β_5-integrin KO fibroblasts. The magnified insert depicts an example of intracellular pools of active $\alpha_5\beta_1$-integrin at what appears to be multi-vesicular endosomes. Note that small particles, indicative of active $\alpha_5\beta_1$-integrin, seemed to be absent from the clathrin-coated vesicle; these particles are indicated by the closed arrow, while arrowheads point to examples of random immunogold particles.

DOI: 10.7554/eLife.20600.037

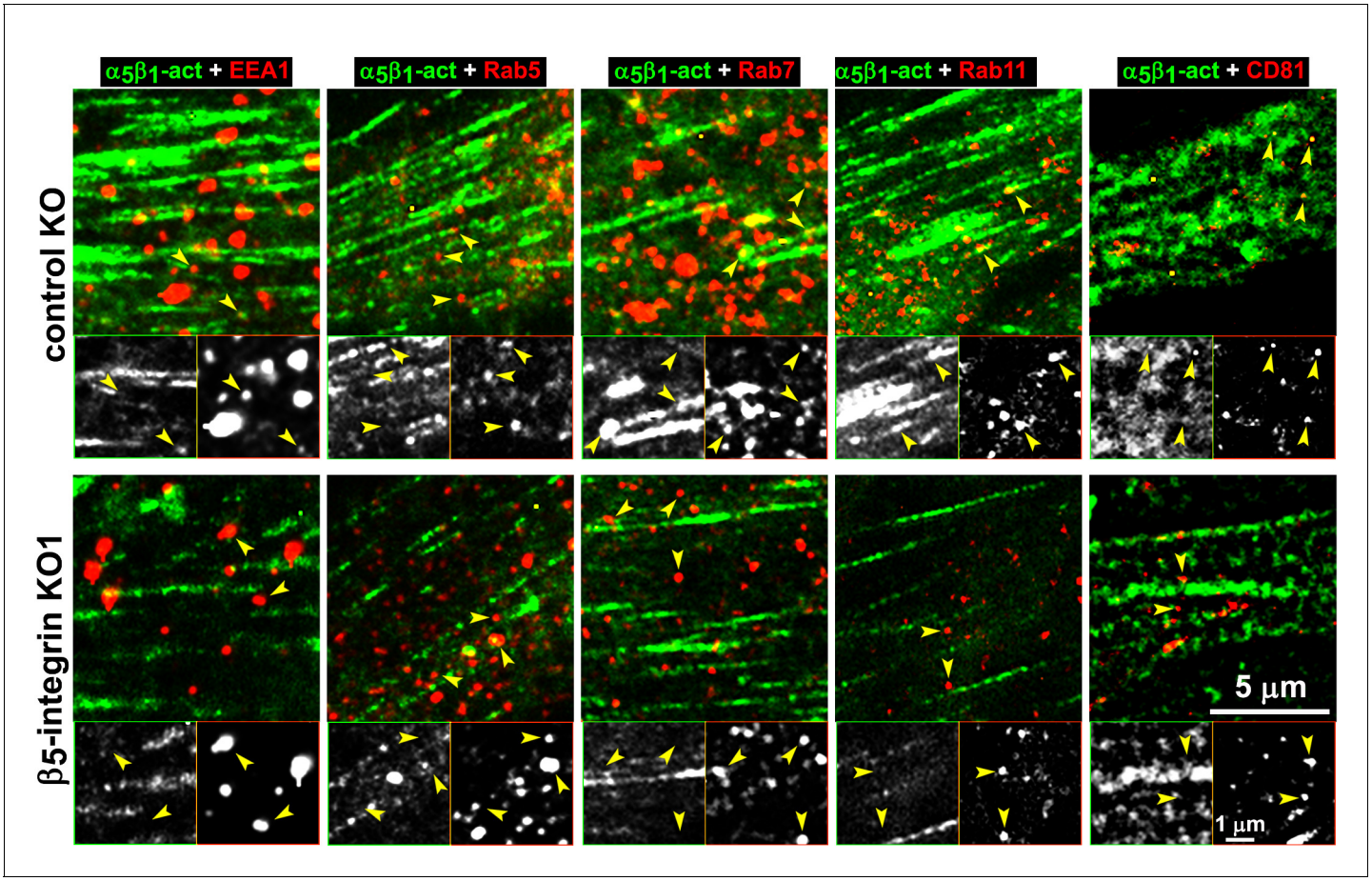

Figure 9. Loss of β5-integrin expression in naïve fibroblasts effectively reduces D-ECM-induced relocation of active $\alpha_5\beta_1$-integrin to late and multivesicular endosomes. Control KO (cntrl-KO) or β_5-integrin knock-out (β_5-KO1) naïve fibroblastic stellate cells were cultured overnight in desmoplastic-ECMs (D-ECM), and were subjected to indirect immunofluorescence using SNAKA51 to detect active $\alpha_5\beta_1$-integrin ($\alpha_5\beta_1$-act in green) in combination with one of the following endosomal markers shown in red: anti-EEA-1 (for early endosome), anti-Rab5 (for clathrin-mediated endocytosis early endosome), anti-Rab7 (late endosome to be degraded, recycled or rerouted), anti-Rab11 (late endosome to be recycled), or anti-CD81 (multivesicular endosomes). Top panels: confocal images were captured for each double-stained condition to identify the localization of active $\alpha_5\beta_1$-integrin in relation to the assorted types of endosomes shown in red. Yellow arrowheads point to assorted endosomes and are identically placed in the slightly zoomed monochromatic inserts shown below, which allow better appreciation of the relative locations of the markers vs. those of active $\alpha_5\beta_1$-integrin. Note that the partial co-localization of active $\alpha_5\beta_1$-integrin with Rab7, Rab11 and especially with CD81 is lost in the naïve β_5-KO compared to control KO naive fibroblasts in response to D-ECM.

DOI: 10.7554/eLife.20600.038

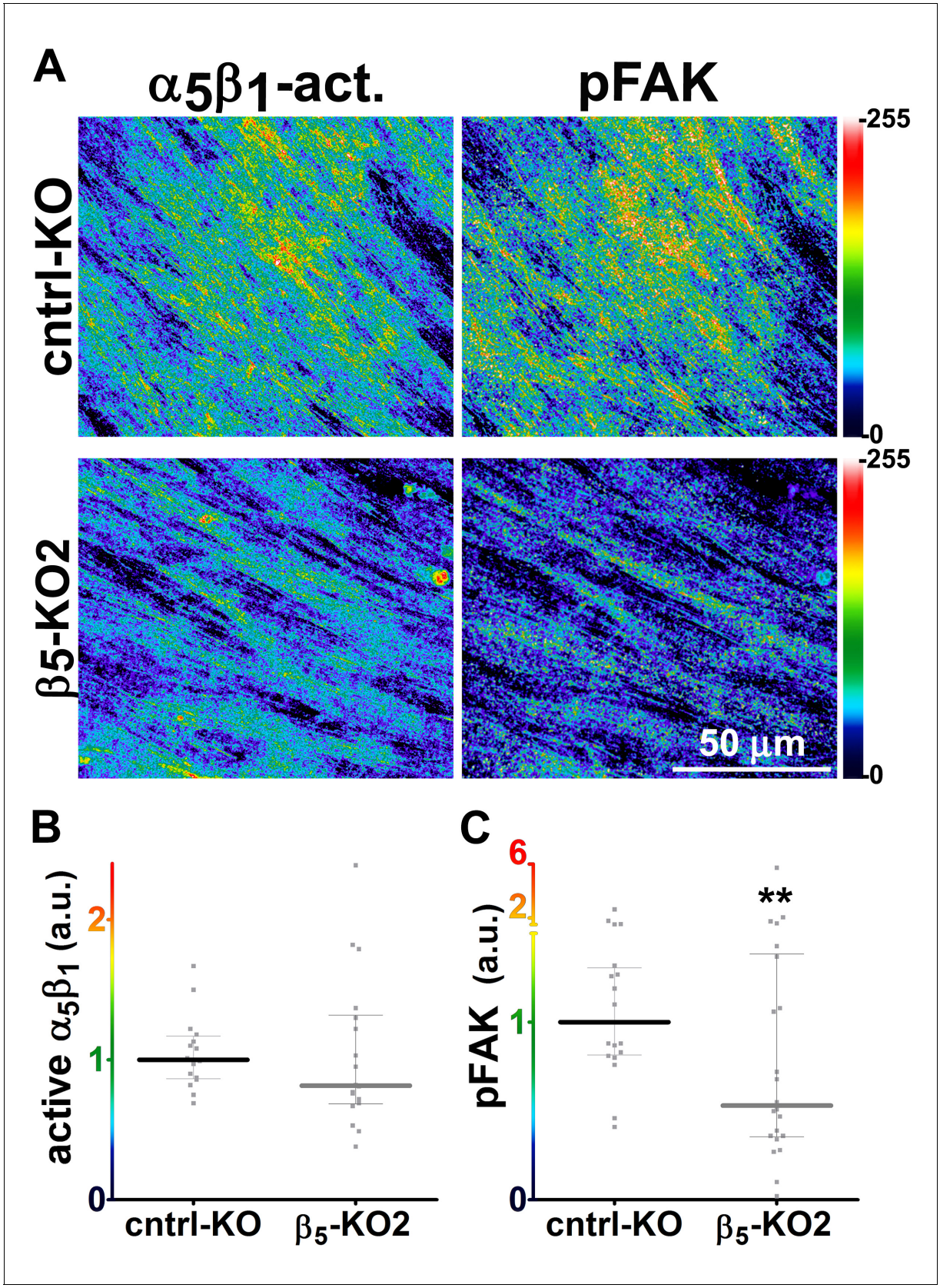

Figure 10. Loss of β_5-integrin in D-ECM-producing CAFs fails to significantly reduce overall levels of active $\alpha_5\beta_1$-integrin. Representative indirect immunofluorescence images showing active $\alpha_5\beta_1$-integrin (with SNAKA51 [***Clark et al., 2005***] [$\alpha_5\beta_1$-act.]) or pFAK in control KO (cntrl-KO) or β_5-integrin

Figure 10 continued on next page

Figure 10 continued

KO (β5-KO1) CAFs at the completion of the 3D matrix production process (see Materials and methods). (**B**-**C**) Graphs depicting levels of active $\alpha_5\beta_1$-integrin (**B**) or pFAK (**C**;**p=0.0465) in control and β_5-integrin KO CAFs from (**A**). Note that active $\alpha_5\beta_1$-integrin levels in CAFs were not significantly changed in response to β_5-integrin loss.

DOI: 10.7554/eLife.20600.039

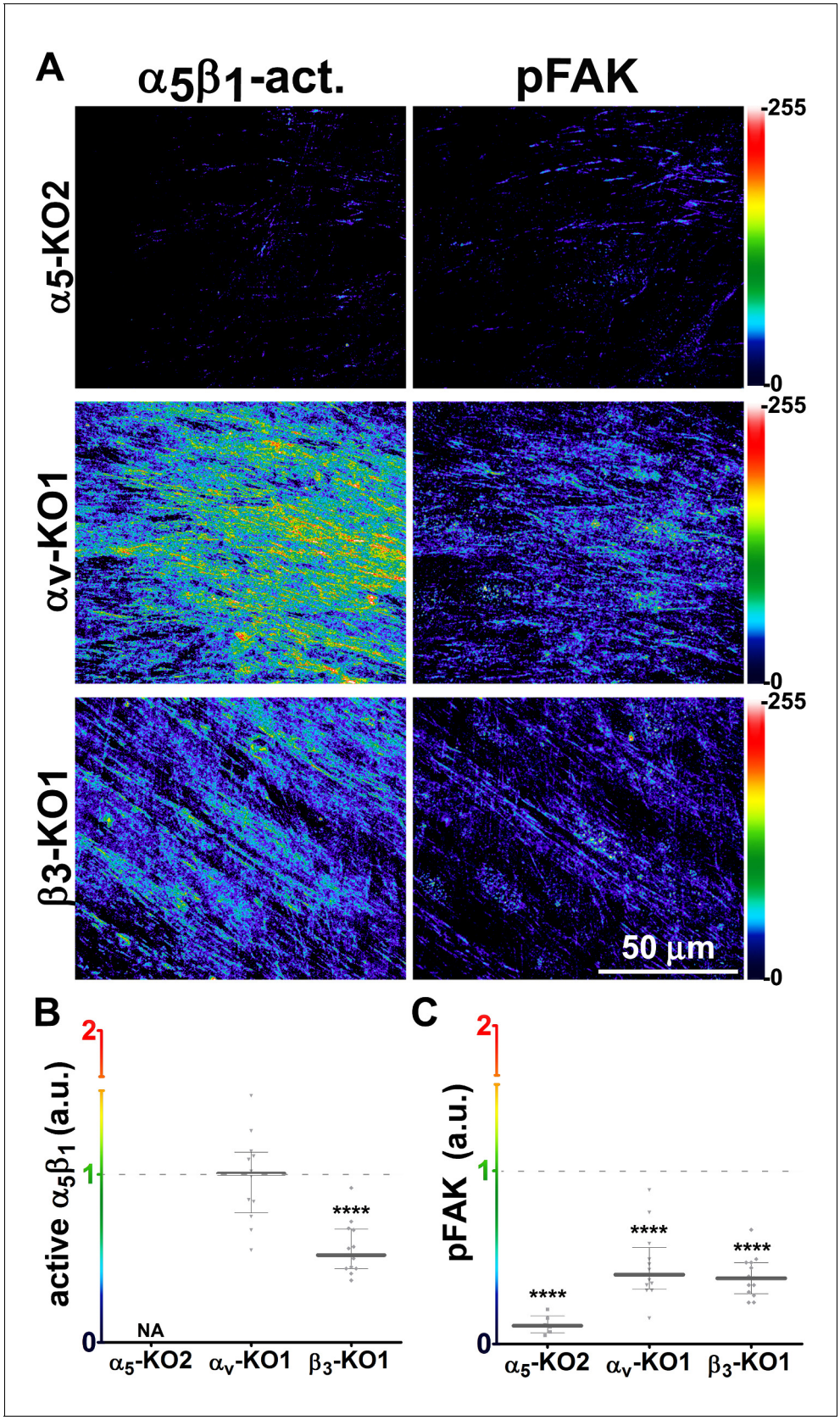

Figure 10—figure supplement 1. Loss of β_3- but not of α_V-integrin subunits in D-ECM-producing CAFs alters levels of active $\alpha_5\beta_1$-integrin. (**A**) Representative indirect immunofluorescence images showing active $\alpha_5\beta_1$-integrin (with SNAKA51 [***Clark et al., 2005***] [$\alpha_5\beta_1$-act.]) or pFAK

Figure 10—figure supplement 1 continued on next page

Figure 10—figure supplement 1 continued

corresponding to α_5-integrin KO (α_5-KO2), α_V-integrin KO (α_V-KO1) or β_3-integrin KO (β_3-KO1) CAFs at the conclusion of matrix production (see Materials and methods). (**B**-**C**) Graphs depicting levels of active $\alpha_5\beta_1$-integrin (**B**) or pFAK (**C**) in control and β_5-integrin KO CAFs from (**A**) (****p<0.0001). Dotted lines in (**B**–**C**) denote control KO CAF normalized levels from ***Figure 10***. Note that active $\alpha_5\beta_1$-integrin levels in CAFs were altered in response to β_3- but not α_V-integrin loss, whereas levels detected in α_5-integrin KO CAFs served as background control and were therefore marked as 'not applicable' (**NA**).

DOI: 10.7554/eLife.20600.040

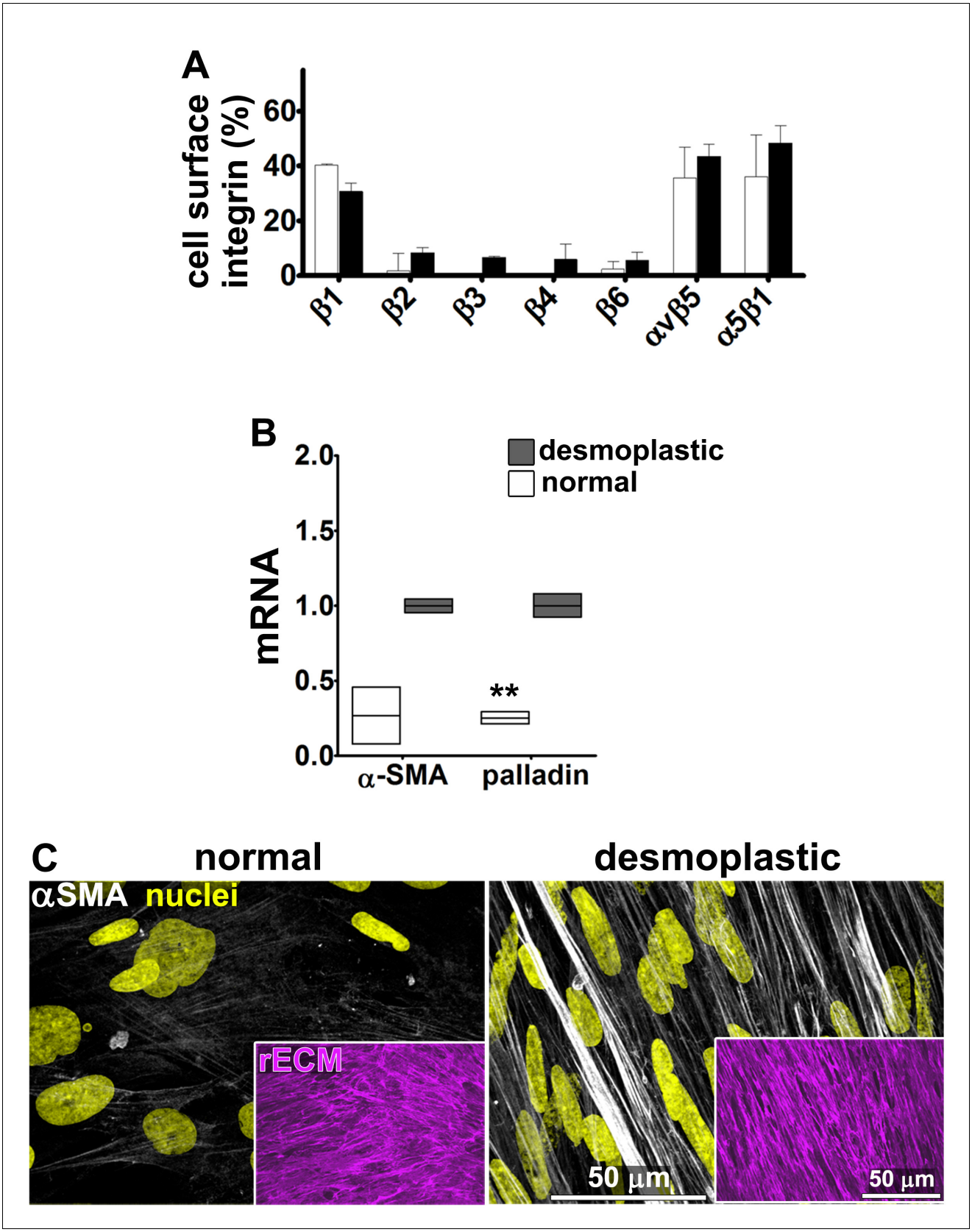

Figure 11. Renal fibroblasts present a similar profile to pancreatic fibroblasts during matrix production. Fibroblasts were isolated from RCC surgical pathologically normal or tumoral samples, and their ECM-producing phenotypes were assessed after seven days of matrix production. (**A**) An integrin-

Figure 11 continued on next page

Figure 11 continued

dependent cell adhesion array test was used to assess the PM expression of integrin heterodimers in primary fibroblasts isolated from normal (white bars) vs. tumoral (dark bars) tissues. Note that no differences were apparent between the two cell types with regards to levels of $\alpha_v\beta_5$ and $\alpha_5\beta_1$ integrins. (**B**) Normal vs. desmoplastic mRNAs levels, corresponding to αSMA and palladin (used as an additional myofibroblastic marker as before) were obtained via RT-qPCR from the indicated 3D-cultures following renal ECM (rECM) production, which was achieved via confluent culturing of fibroblasts in the presence of ascorbic acid for a period lasting 8 days (***Franco-Barraza et al., 2016***) (**p=0.0286). (**C**) Representative images of normal vs. desmoplastic phenotypes, subsequent to 3D rECM production, are shown; comparison of low vs. high αSMA levels (white), heterogeneous/round vs. elongated/spindled nuclei (yellow) and disorganized/isotropic vs. parallel aligned/anisotropic rECMs (magenta) are evident in the representative images.

DOI: 10.7554/eLife.20600.041

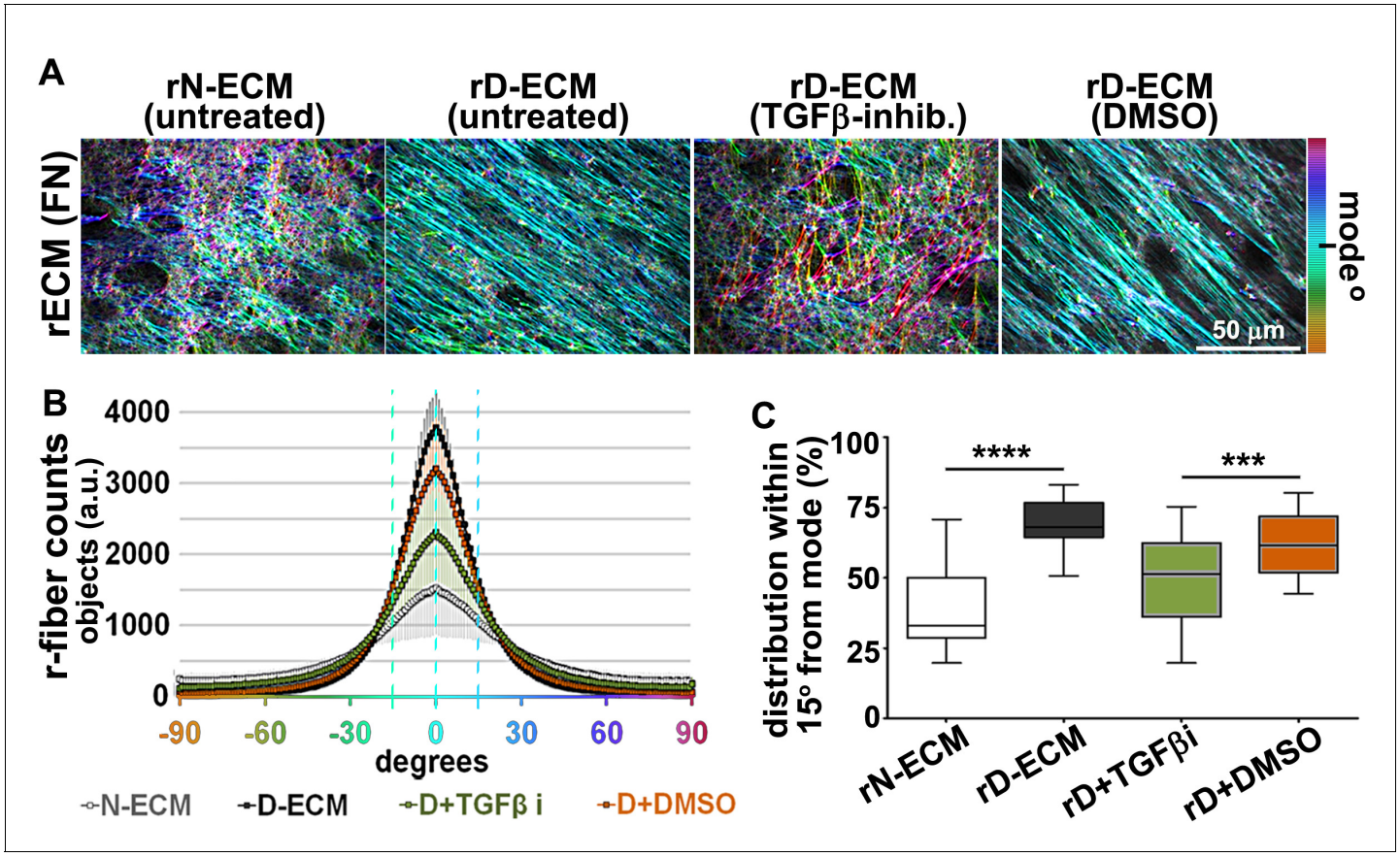

Figure 11—figure supplement 1. rD-ECM production by rCAFs is TGFβ-dependent. (**A**) Images representative of the ECM phenotypes of renal normal (rN-ECM) and RCC-associated CAF-derived ECMs (rD-ECM), and of cells treated with small molecule TGFβ1-receptor SB431542 (TGFβ-inhib) or with vehicle (DMSO) during rD-ECM production are shown. ECM fiber angle distributions, measured with Image-J's 'OrientationJ' plug, are represented by the various colors, while all images were normalized using hue values for common, cyan, mode angle visualization as represented in the bar in the right. (**B**) Curves corresponding to the indicated experimental conditions depicting averaged and variations of angle distributions that were normalized to 0˚ modes. Dotted lines indicate 15˚ spread from the mode. (**C**) Plotted data from (**B**) summarizing percentages of fibers distributed at 15˚angles from the mode in each of the indicated experimental conditions. (**** $p<0.0001$, ***$p<0.0028$).

DOI: 10.7554/eLife.20600.042

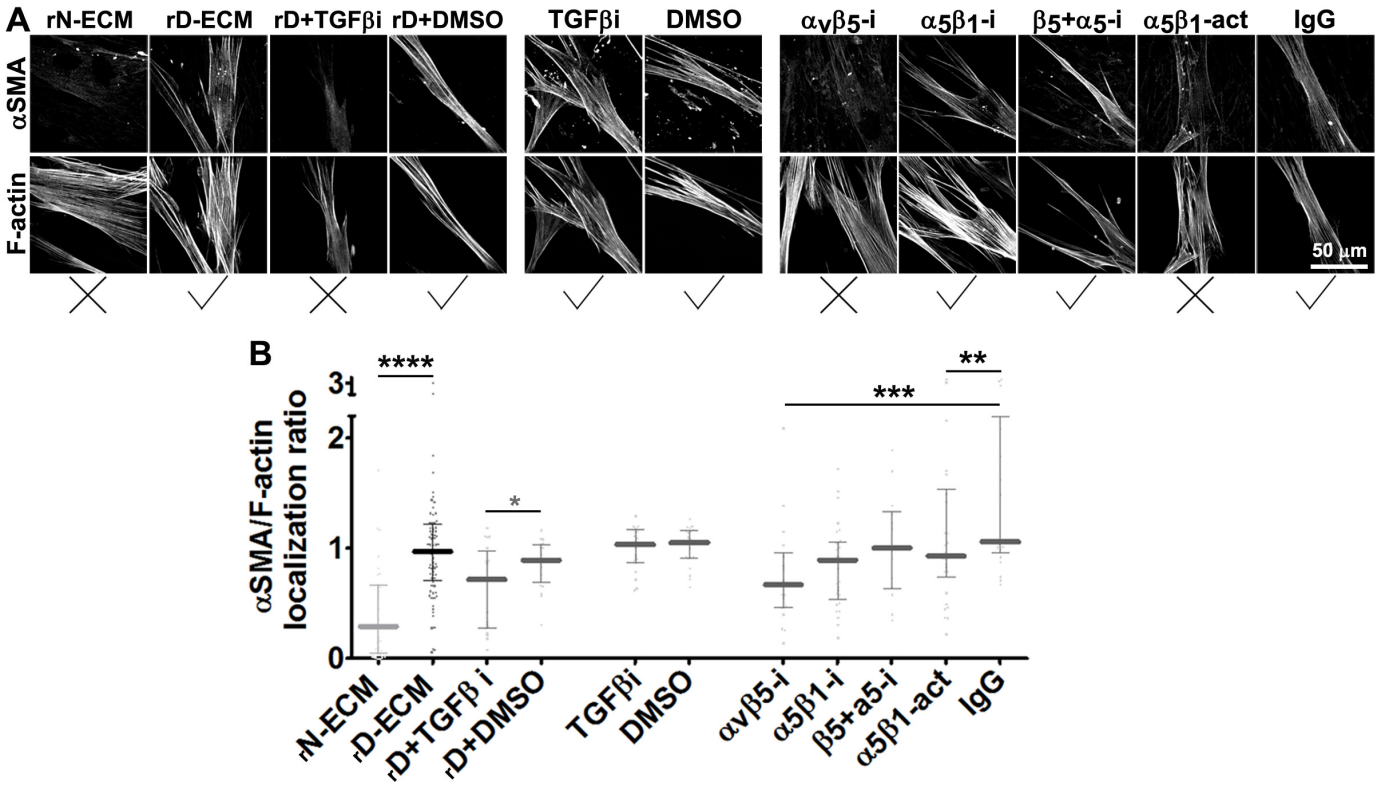

Figure 11—figure supplement 2. rD-ECM-induced renal naïve-to-myofibroblastic activation is reminiscent of pancreatic D-ECM fibroblastic stellate cell activation. Naïve renal fibroblasts were cultured overnight within normal (rN-ECM) or RCC-associated CAF-derived ECMs (rD-ECM). rD-ECMs were produced in the presence of vehicle control (D + DMSO) or TGFβ1-receptor inhibitor (D + TGFβi). Alternatively, naïve cells cultured within rD-ECMs were treated with TGFβ1 inhibitor (TGFβ-i), with vehicle (DMSO), with the function-blocking anti-$\alpha_v\beta_5$-integrin ALULA(***Su et al., 2007***) ($\alpha_v\beta_5$-i), with the function-blocking anti-$\alpha_5\beta_1$-integrin mAB16 (***Akiyama et al., 1989***) ($\alpha_5\beta_1$-i), with combinations of ALULA + mAb16 (β_5-i + α_5-i), with the function-stabilizing anti-active $\alpha_5\beta_1$-integrin antibody SNAKA51 (***Clark et al., 2005***) ($\alpha_5\beta_1$-act), or with corresponding isotype controls (IgG). (**A**) Representative monochromatic images of immunofluorescently labeled αSMA and corresponding actin stress fibers (F-actin). Checkmarks indicate conditions that induce a myofibroblastic activation phenotype in response to rD-ECM. X marks indicate conditions that did not induce myofibroblastic activation. (**B**) Graph depicting measured levels of stress fiber (F-actin) localized αSMA ratios. The results and statistical analysis for this set of experiments are summarized in ***Table 5***. Note that, while TGFβ inhibition rendered matrices produced by CAFs (D + TGFβi) nonfunctional, naïve renal fibroblasts are effectively activated by rD-ECM in a TGFβ-independent manner (TGFβ-i) that is apparently maintained by the same integrin crosstalk seen in the human PDAC model.

DOI: 10.7554/eLife.20600.043

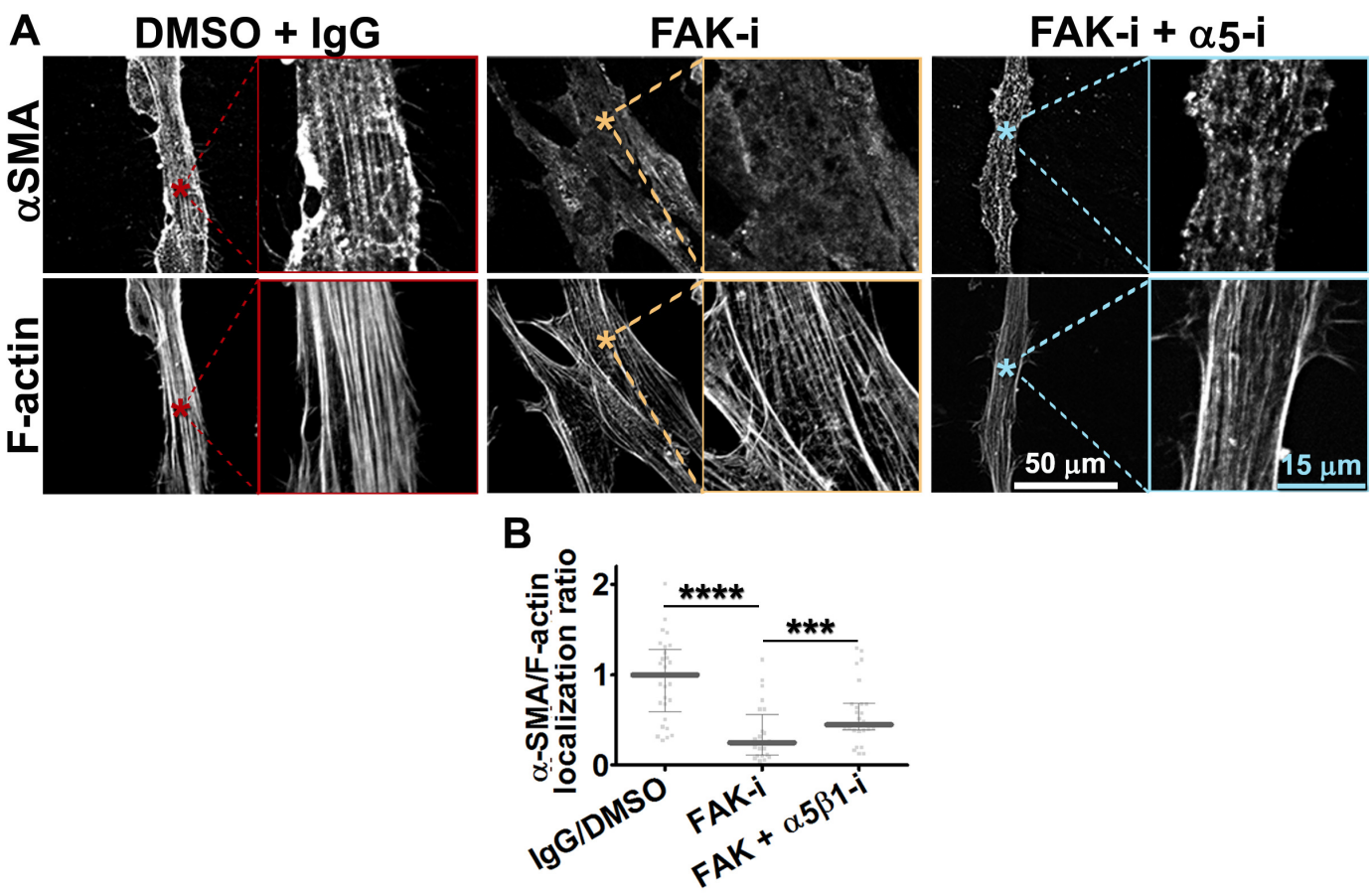

Figure 11—figure supplement 3. FAK-independent $\alpha_5\beta_1$-integrin activity negatively regulates rD-ECM-induced naïve-to-myofibroblastic activation. Naïve r-fibroblasts were re-plated onto rD-ECMs and challenged with either control conditions (DMSO + IgG), small molecule FAK inhibitor PF573,228 (***Slack-Davis et al., 2007***) (FAK-i) alone or FAK-i in combination with $\alpha_5\beta_1$-integrin inhibitor (FAK-i + α_5-i, mAb16 [***Akiyama et al., 1989***]), and the activation of fibroblasts was tested. (**A**) Representative monochromatic images of immunofluorescently labeled αSMA and actin stress fibers (F-actin). Colored asterisks in (**A**) represent areas that are magnified in the corresponding panels to the right. (**B**) Quantification of αSMA at actin stress fibers (F-actin) from (**A**) normalized to DMSO + IgG control (one arbitrary unit; a.u). (IgG/DMSO vs. FAK-i: ****p=<0.0001, FAK-i vs. FAK-i + $\alpha_5\beta_1$-i: ***p=0.0051).

DOI: 10.7554/eLife.20600.044

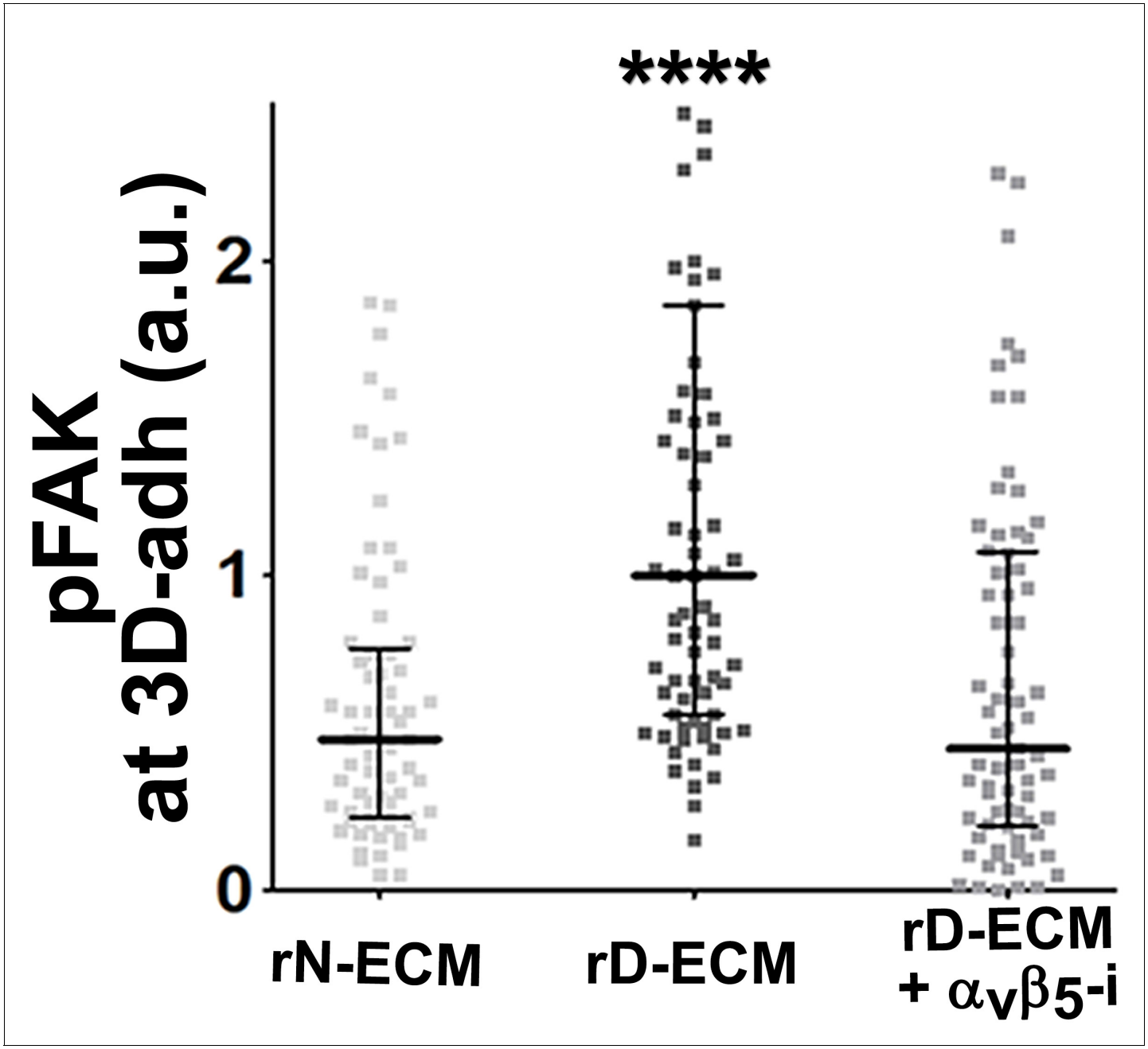

Figure 11—figure supplement 4. rD-ECM-induced increase in pFAK levels localized at 3D-adhesions are regulated by $\alpha_v\beta_5$–integrin in naïve renal fibroblasts. Naïve renal fibroblasts were cultured overnight within N-ECM or RCC-associated CAF-derived ECMs (rD-ECM) in the presence or absence of ALULA (***Su et al., 2007***) (rD-ECM + $\alpha_v\beta_5$-i) and 3D-adhesions using mAb11 and pFAK-Y^{397} were detected by indirect immunofluorescence. The resulting SMIA-CUKIE-generated integrated intensities of pFAK-Y^{397} at 3D-adhesions (****$p<0.0001$) are depicted in this graph.
DOI: 10.7554/eLife.20600.045

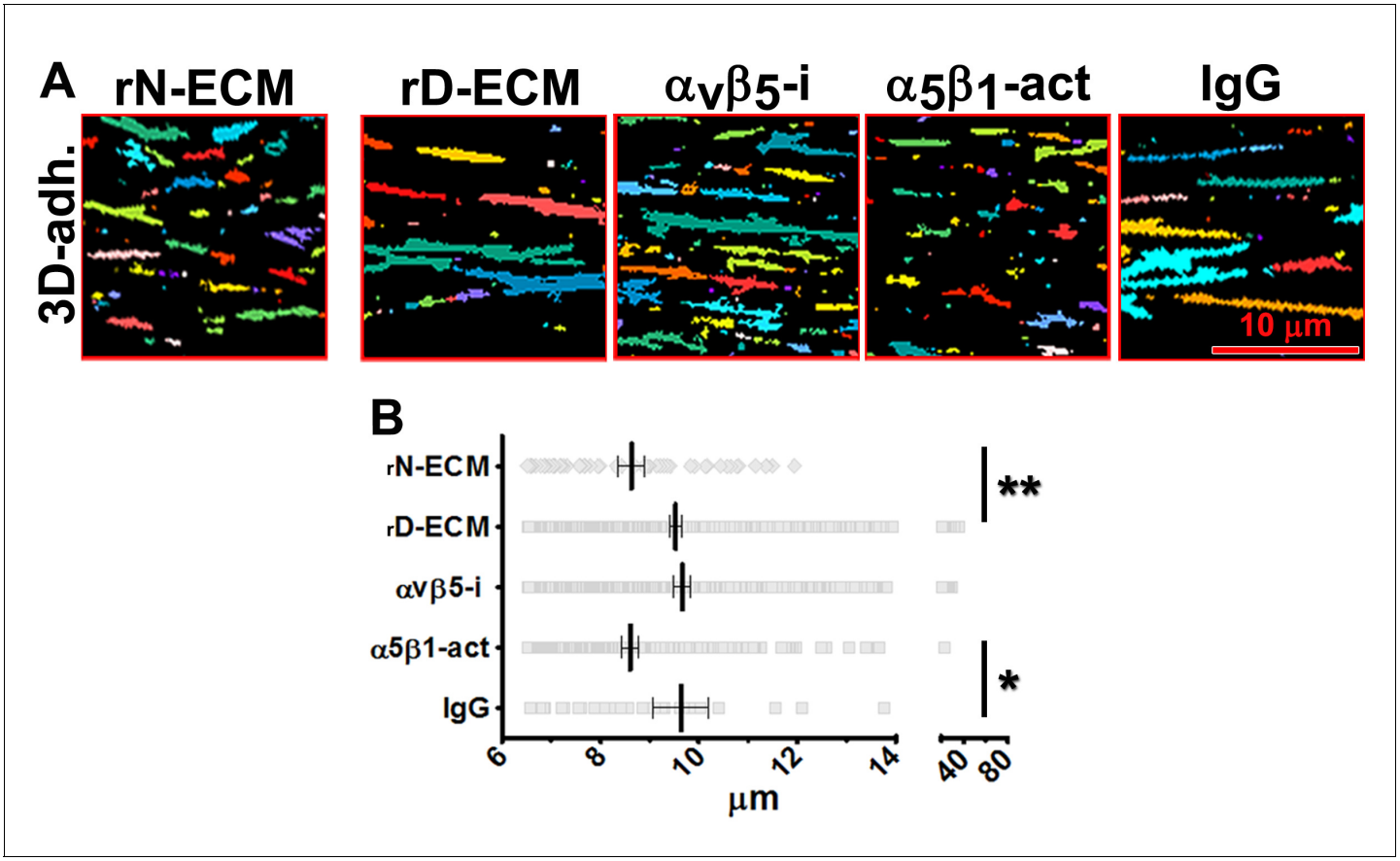

Figure 11—figure supplement 5. rD-ECM regulates 3D-adhesion structure length, dependent on $\alpha_5\beta_1$-integrin activity. (**A**) Indirect immunofluorescent and spinning disc confocal generated images of 3D-adhesions, identified using mAb11 (***Cukierman et al., 2001***), formed by naïve fibroblastic cells cultured within rN-ECM or rD-ECM in the absence (cnt.) or in the presence of ALULA (***Su et al., 2007***) for $\alpha_v\beta_5$-integrin inhibition ($\alpha_v\beta_5$-i) or of SNAKA51 (***Clark et al., 2005***) to stabilize $\alpha_5\beta_1$-integrin activity ($\alpha_5\beta_1$ act) or of IgG as control. Images were processed using the computer-selected internally threshold objects (ITOs) function of the MetaMorph 7.8.0.0 software. (B) Quantification of the length of ITO-generated objects from (**A**) (**p=0.0492, *p=0.0928). Note the significant differences in 3D-adhesion length observed between rN-ECM and rD-ECM as well as between IgG and SNAKA51 treatments.

DOI: 10.7554/eLife.20600.046

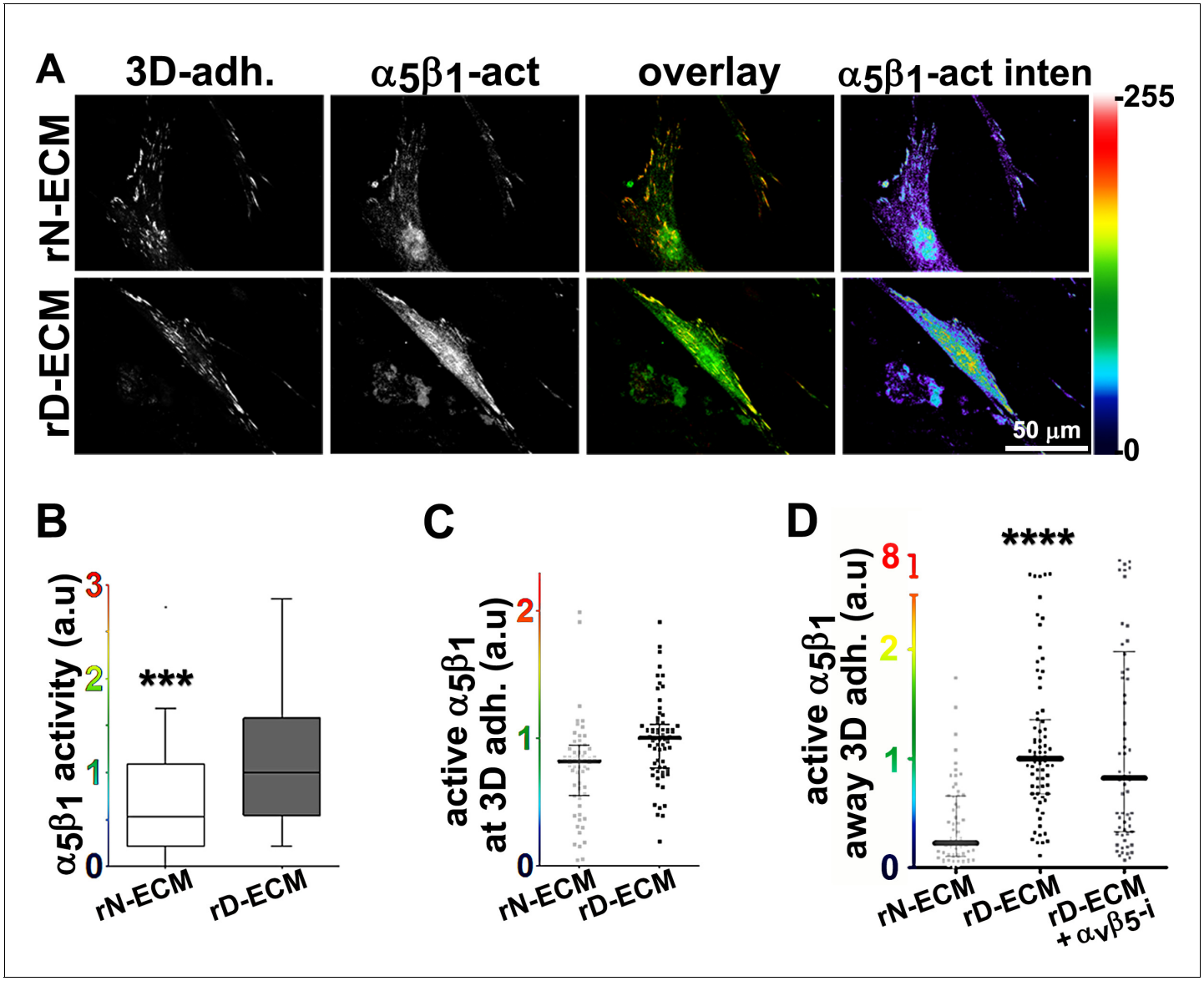

Figure 11—figure supplement 6. Naïve renal fibroblastic cells increase overall levels of active $\alpha_5\beta_1$-integrin in response to rD-ECM. (**A**) Double-labeled images depicting 3D-adhesion (red in overlay; 3D-adh.) and active $\alpha_5\beta_1$-integrin (green in overlay; $\alpha_5\beta_1$-act) in naïve r-fibroblasts cultured overnight in renal normal-ECMs (rN-ECM) or RCC-associated CAF-derived ECMs (rD-ECM). Pseudocolored images at the far right represent semi-quantitative images, maximum reconstructions of active $\alpha_5\beta_1$-integrin levels ($\alpha_5\beta_1$-act inten), with a corresponding intensity bar shown on the right. Total active $\alpha_5\beta_1$-integrin levels were calculated using SMIA-CUKIE, which is publicly available at https://github.com/cukie/SMIA. (**B–D**) Results are summarized in (**B**), using median levels on rD-ECM for normalization (one arbitrary unit; a.u.) (***p=0.0001), in (**C**) using integrated levels of active $\alpha_5\beta_1$-integrin localized at 3D-adhesions, and in (**D**), using active $\alpha_5\beta_1$-integrin integrated intensity levels, measured away from 3D-adhesions, in the absence or presence of $\alpha_v\beta_5$-integrin inhibition (****p<0.0001).

DOI: 10.7554/eLife.20600.047

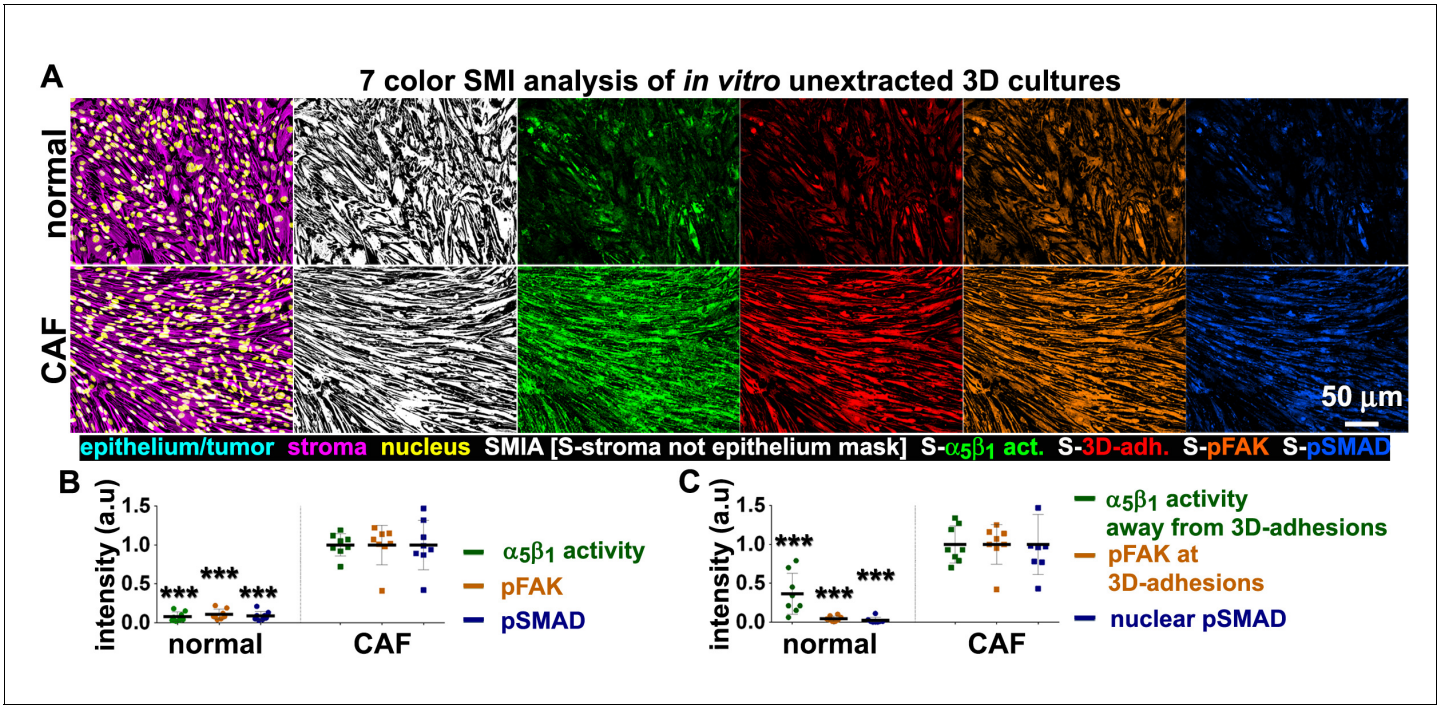

Figure 12. *In vitro* characterization of normal and tumor-associated 3D matrix-producing fibroblastic cultures provide a set of prognostic markers to be tested *in vivo*. (**A**) SMI approach image outputs of *in vitro* 3D cultures of naïve fibroblastic stellate cells (normal) and desmoplastic CAFs (tumor associated) during ECM production. Leftmost panels demonstrate the positive staining of vimentin (magenta), and the lack of cytokeratin (cyan), indicating the purity of the fibroblasts isolated; nuclei are marked in yellow. White masks (SMI approach; SMIA) in the next panel represent vimentin-positive/cytokeratin-negative (in this case vimentin-positive only as there is no cytokeratin present) areas as recognized by the software following threshold values provided by the user. Next panels represent the assorted markers localized at pixels corresponding to SMI-selected masks and conforming to: active $\alpha_5\beta_1$-integrin (S-$\alpha_5\beta_1$ act.; in green), 3D-adhesions (S-3D-adh.; in red), pFAK-Y^{397} (S-pFAK; in orange), and pSMAD2/3 (S-pSMAD; in blue). (**B**) Graphs summarizing SMIA-CUKIE-generated data outputs representing median intensity levels of active $\alpha_5\beta_1$-integrin (green bullets), pFAK-Y^{397} (orange bullets) and pSMAD2/3 (blue bullets) from data conditions as in (**A**) (***p=0.0002). (**C**) Graphs summarizing SMIA-CUKIE-generated data from marker intersections indicating mean intensity levels of $\alpha_5\beta_1$-integrin activity localized away from 3D-adhesions (green bullets) (***p=0.0008), pFAK-Y^{397} at 3D-adhesions (orange bullets) (***p=0.0002), and nuclear $pSMAD_{2/3}$ (blue bullets) (***p=0.0002).

DOI: 10.7554/eLife.20600.049

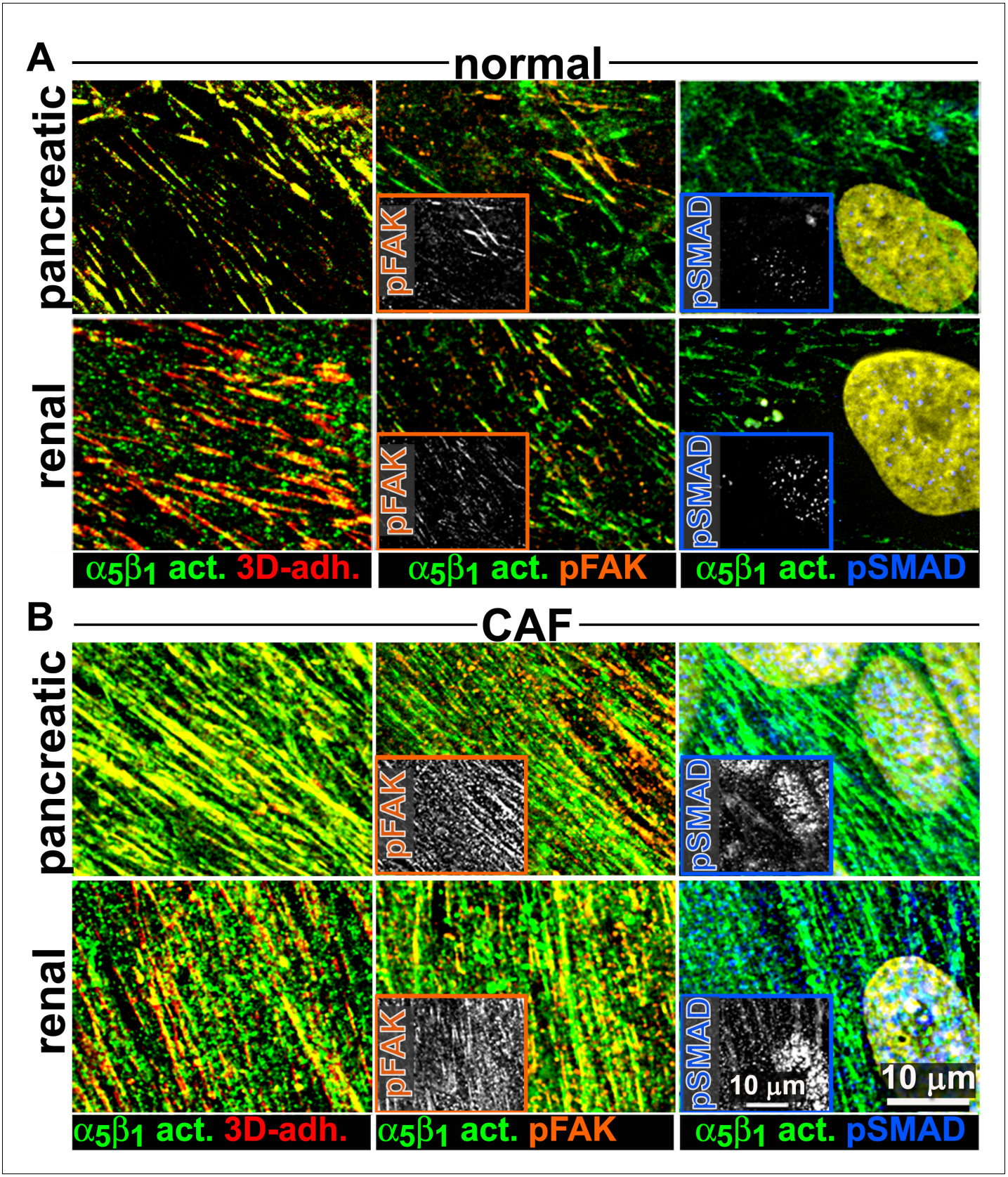

Figure 12—figure supplement 1. *In vitro* characterization of pancreatic and renal normal and CAF unextracted 3D fibroblastic cultures. Samples correspond to normal fibroblastic stellate cells (**A**) and CAFs (**B**): depicted are spinning disc confocal-acquired images of indirect immunofluorescence

Figure 12—figure supplement 1 continued on next page

Figure 12—figure supplement 1 continued

of the assorted stromal markers. Images are shown as overlays to indicate the distribution of active $\alpha_5\beta_1$-integrin ($\alpha_5\beta_1$ act.; green) with regards to 3D-adhesion locations (3D-adh.; red), pFAK-Y^{397} (pFAK; orange), pSMAD2/3 (pSMAD; blue) and nucleus (yellow). Inserts correspond to monochromatic images of the corresponding marker.

DOI: 10.7554/eLife.20600.050

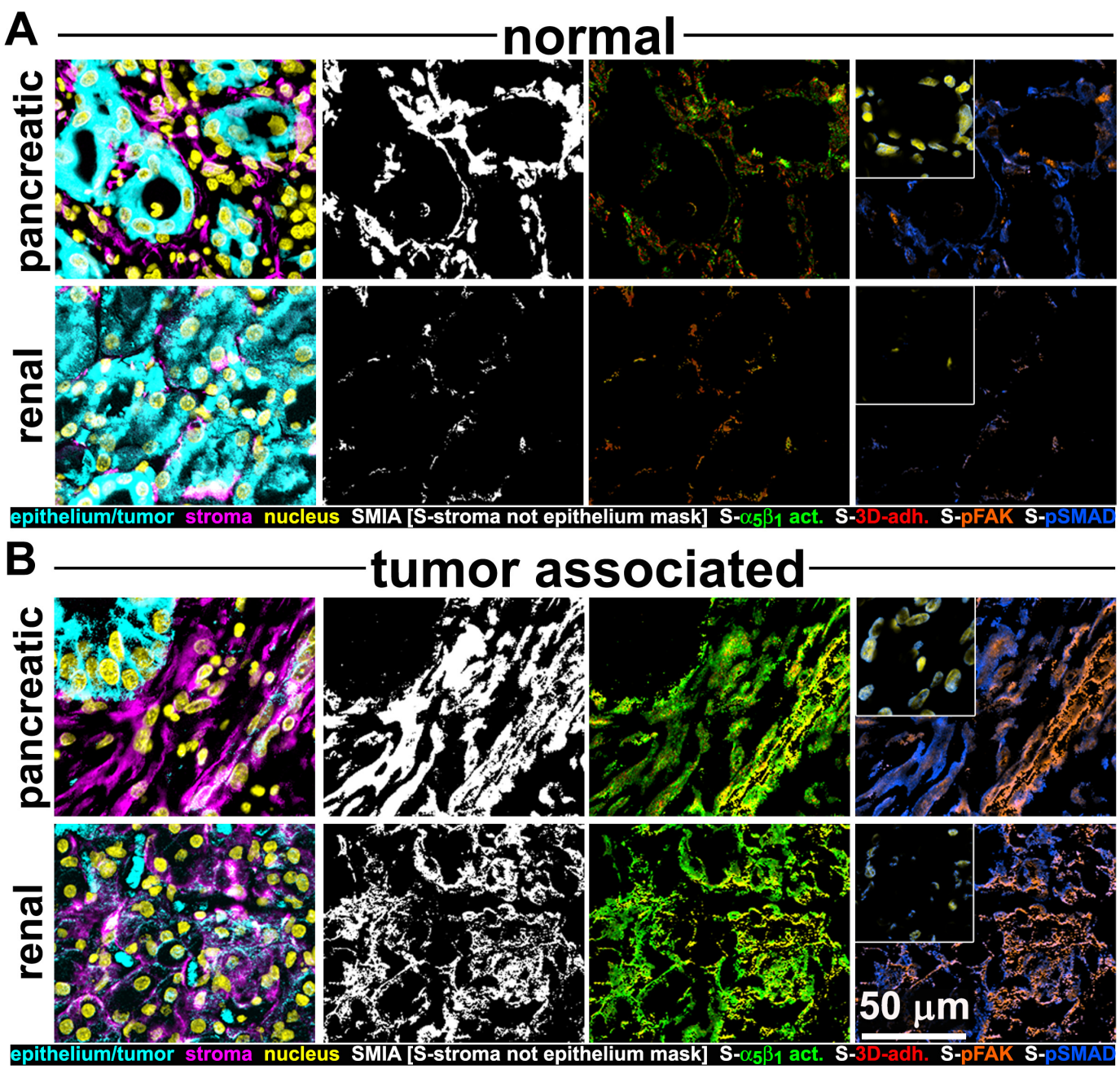

Figure 12—figure supplement 2. *In vitro* uncovered traits correspond to *in vivo* PDAC and RCC stromal phenotypes. A seven-color simultaneous multi-channel immunofluorescent (SMI; see Materials and methods) approach was implemented to analyze FFPE tissue from the original patient surgical samples from which the fibroblasts used *in vitro* were harvested. (**A**) Normal tissue panel, representative images of PDAC and RCC FFPE samples. Note that the PDAC images correspond to pathological and matched normal samples from patient #1; fibroblasts harvested from this pair of samples were immortalized and used to generate all human KOs that were presented above. (**B**) Tumor-associated tissue panel, representative images. The first column of images in (**A**) and (**B**) are overlaid images including the three colors used for 'masked' locations (see Materials and methods for details); epithelial/tumoral areas are pseudocolored in cyan, stromal vimentin is magenta, and nuclei labeled using draq5 are shown in yellow. The SMIA-CUKIE software (https://github.com/cukie/SMIA_CUKIE) was instructed to render an intersection 'mask' image (SMIA-mask 'S'; white) corresponding to pixel areas selected as stroma-positive and epithelial/tumoral-negative to exclude potential mesenchymal to epithelial transduced tumoral locations. Next, to the right of the SMIA mask image, are images of the corresponding markers showing only pixels corresponding to *bona fide* stromal 'masks' depicted in the mask image. Markers shown correspond to: active $\alpha_5\beta_1$-integrin (S- $\alpha_5\beta_1$ act.; green) and 3D-adhesions (S-3D-adh.;

Figure 12—figure supplement 2 continued on next page

Figure 12—figure supplement 2 continued

insert red), followed next to the right by pFAK-Y^{397} (S-pFAK; orange) and pSMAD2/3 (S-pSMAD; blue). Note that only pixels shown, which corresponded to the selected SMIA-mask (white), were quantitatively analyzed by the SMIA-CUKIE software (see ***Figure 12—figure supplement 3*** for values).

DOI: 10.7554/eLife.20600.051

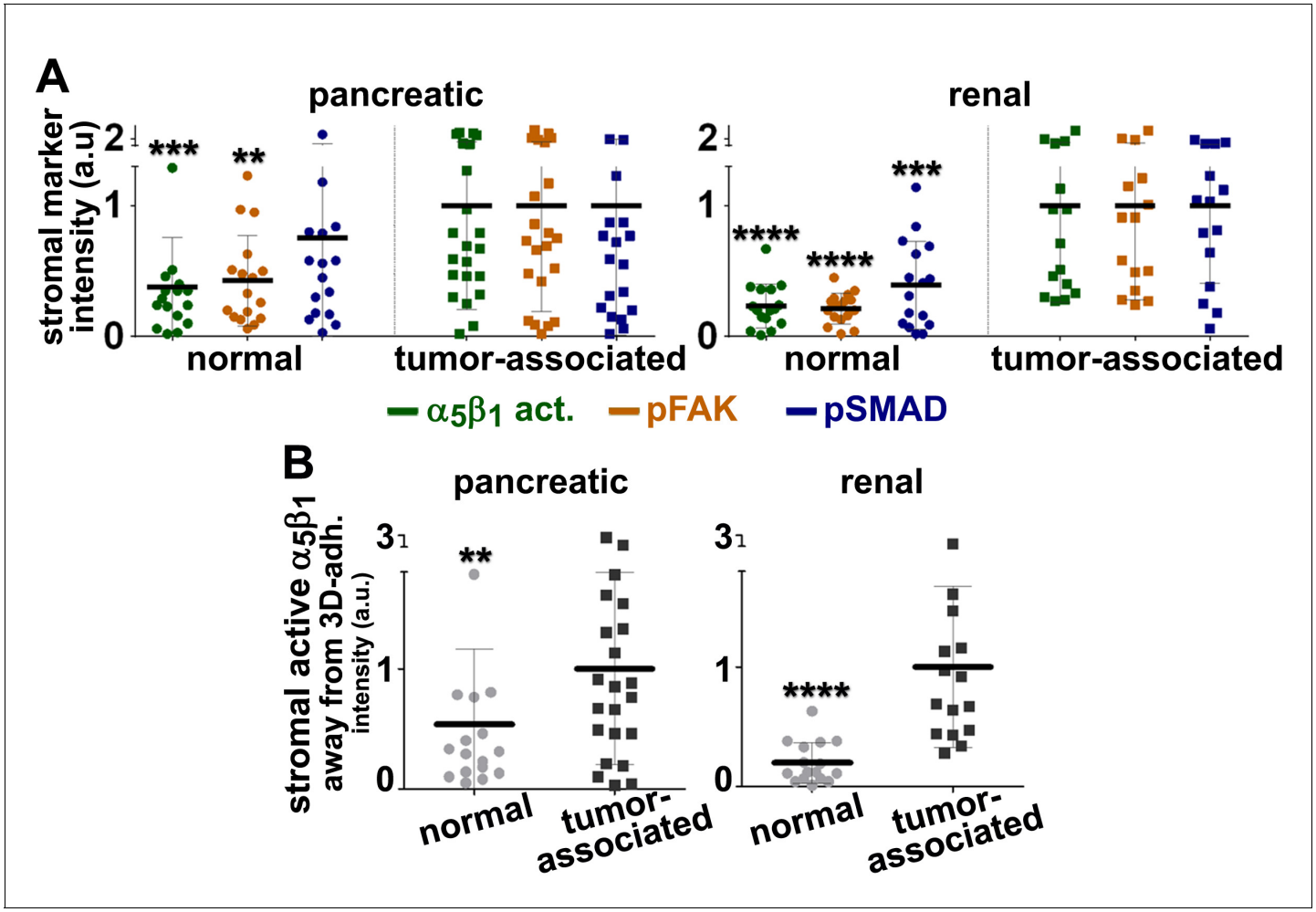

Figure 12—figure supplement 3. Quantification of *in vivo* SMI approach validates *in vitro* findings. (**A**) Individual patient SMIA-CUKIE-generated intensity values from PDAC and RCC normal or tumor-associated tissue samples, representing stromal levels of active $\alpha_5\beta_1$-integrin (green bullets), pFAK-Y^{397} (orange bullets) and pSMAD2/3 (blue bullets). (**B**) Stromal active $\alpha_5\beta_1$-integrin away from 3D-adhesions in pancreatic (left) and renal (right) normal or tumor associated tissues. Significance asterisks represent the following: (**A**) PDAC ***p=0.0013, **p=0.0371; RCC ****p<0.0001, ***p=0.0031; (**B**), **p=0.0371 and ****p<0.0001.

DOI: 10.7554/eLife.20600.052

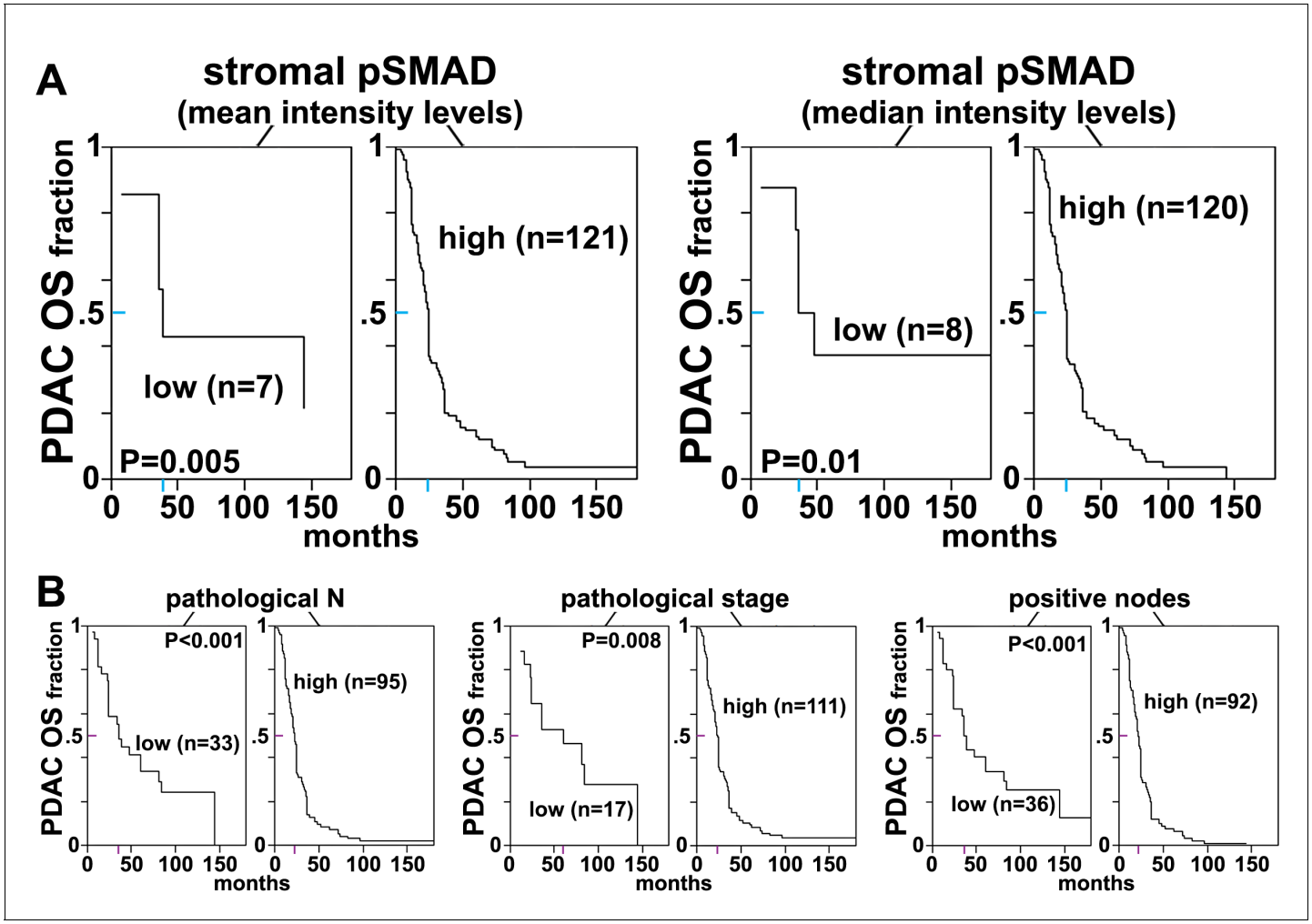

Figure 13. Stromal pSMAD2/3 levels are predictive of poor overall survival in PDAC patients. (**A**) CART-generated survival curves depicting overall survival (OS) as a function of stromal pSMAD2/3 expression in PDAC patients. Left and right curves were obtained using mean and median intensity levels, generated by SMIA-CUKIE, of stromal pSMAD2/3 related to OS, respectively. (**B**) Survival curves depicting pathological N, stage, and node status with PDAC patient OS. Colored tick-lines crossing Y axes indicate 0.5 survival marks and correspond to X axes locations that mark the median survival times obtained from the assorted curves. P values are shown. All patient data as well as SMIA-CUKIE generated data corresponding to human cohort constructed TMAs (shown in ***Table 6***) can be found in the online table at the following publically available link: https://www.foxchase.org/sites/fccc/files/assets/cukierman_Franco-Barraza%20SMIA-CUKIE-Dec-2016.xlsx. Note that since our cohorts comprised of samples obtained from surgeries, early neoplastic stages were overrepresented.

DOI: 10.7554/eLife.20600.054

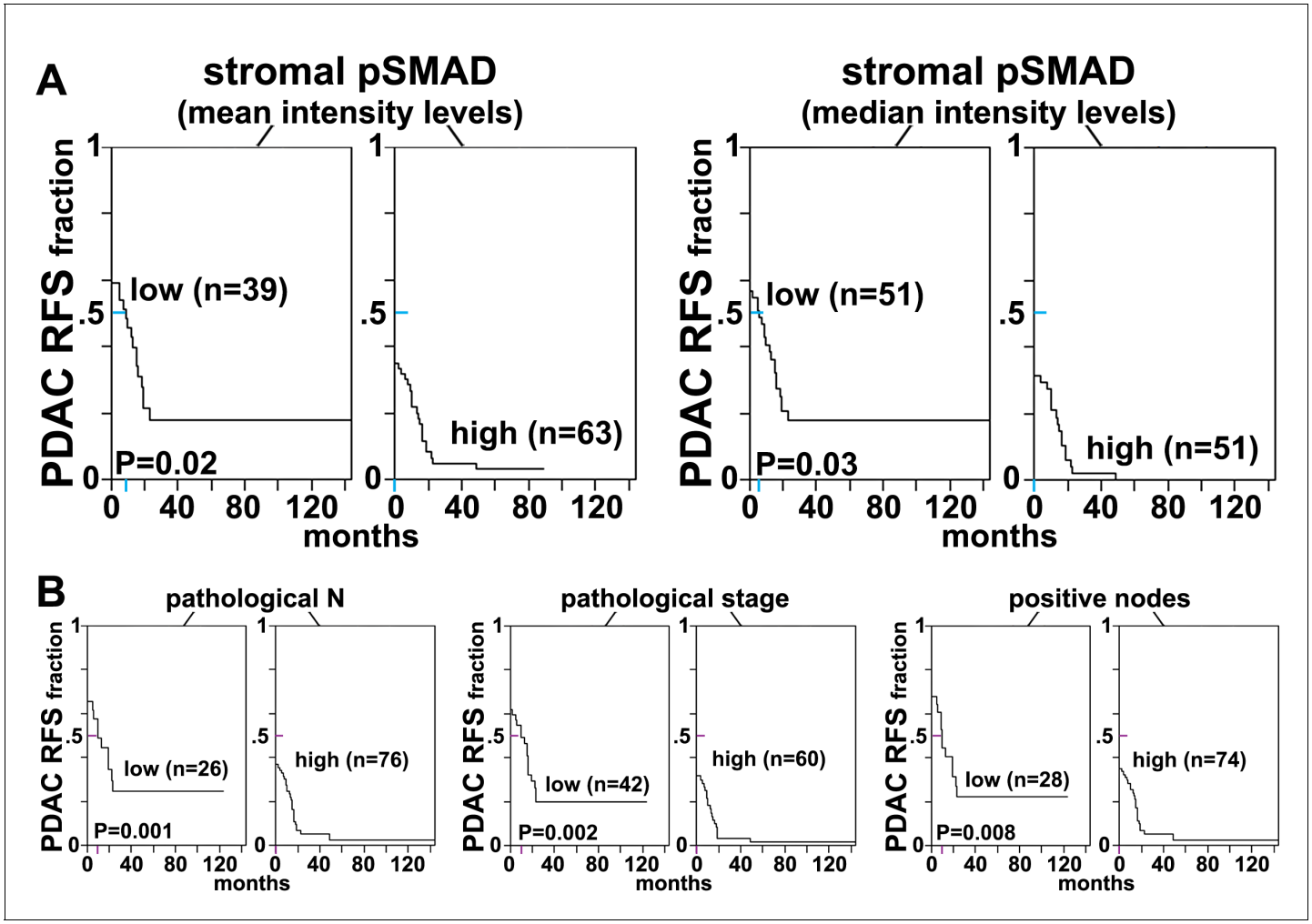

Figure 13—figure supplement 1. Stromal pSMAD2/3 levels are predictive of short recurrence-free survival in PDAC patients. (**A**) CART-generated survival curves indicative of recurrence-free survival (RFS) as a function of stromal pSMAD2/3 expression in PDAC patients. Left and right curves were obtained using mean and median intensity levels, generated by SMIA-CUKIE, of stromal pSMAD2/3 related to RFS, respectively. (**B**) Survival curves depicting pathological N, stage, and node status plotted against PDAC patient RFS fraction. Colored tick-lines crossing Y axes indicate 0.5 survival marks and correspond to X axis locations that mark the median RFS times obtained from the assorted curves. P values are shown. All patient data as well as SMIA-CUKIE generated data corresponding to human cohort constructed TMAs (shown in ***Table 6***) can be found in the online table at the following publically available link: https://www.foxchase.org/sites/fccc/files/assets/cukierman_Franco-Barraza%20SMIA-CUKIE-Dec-2016.xlsx. Note that since our cohorts comprised of samples obtained from surgeries, early neoplastic stages were overrepresented.

DOI: 10.7554/eLife.20600.055

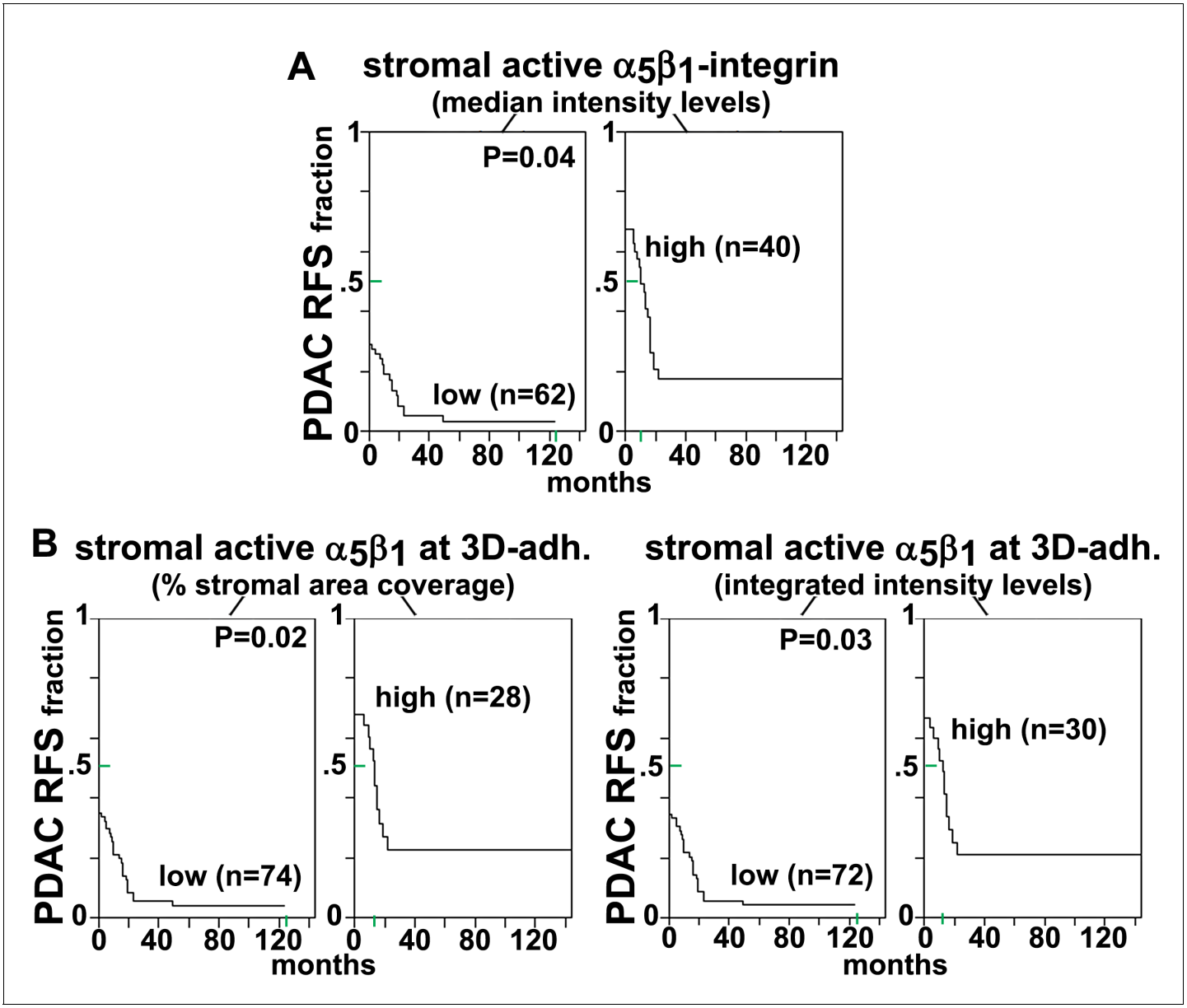

Figure 13—figure supplement 2. Stromal active $\alpha_5\beta_1$-integrin levels localized at 3D-adhesions correlate with longer recurrence-free survival in PDAC patients. CART-generated survival curves depicting recurrence-free survival (RFS) as a function of active stromal $\alpha_5\beta_1$-integrin levels in PDAC patients. Curves were obtained using (**A**) active $\alpha_5\beta_1$-integrin median intensity levels and (**B**) percentage area coverage or integrated intensity of stroma populated by active $\alpha_5\beta_1$-integrin localized at 3D-adhesions that were generated by SMIA-CUKIE, related to RFS. Colored tick-lines crossing Y axes indicate 0.5 survival marks and correspond to X axis locations that mark the median RFS obtained from the curves. P values are shown. All patient data as well as SMIA-CUKIE-generated data corresponding to human cohort constructed TMAs (shown in ***Table 6***) can be found in the online table at the following publically available link : https://www.foxchase.org/sites/fccc/files/assets/cukierman_Franco-Barraza%20SMIA-CUKIE-Dec-2016.xlsx. Note that since our cohorts comprised of samples obtained from surgeries, early neoplastic stages were overrepresented.

DOI: 10.7554/eLife.20600.056

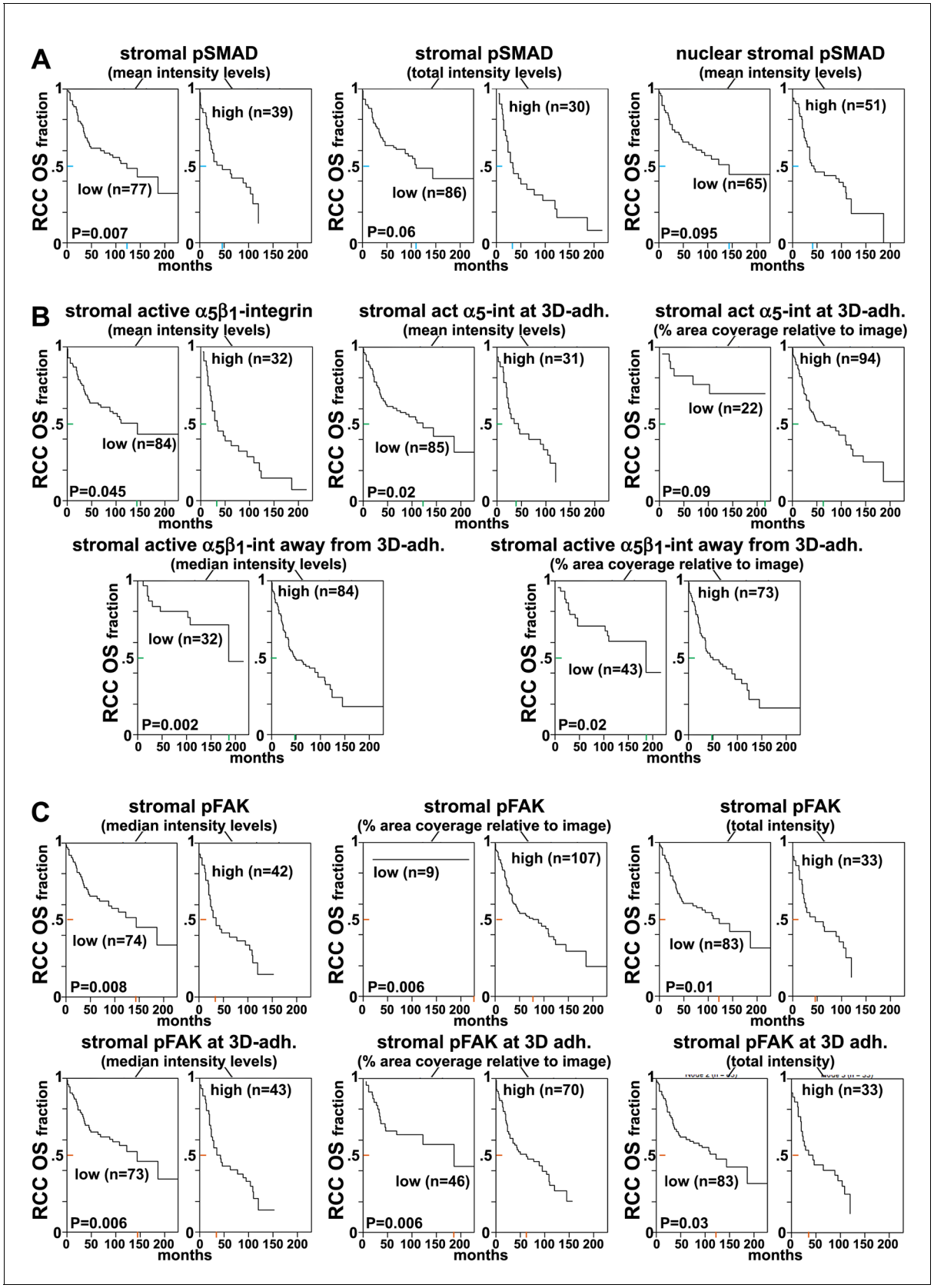

Figure 13—figure supplement 3. Stromal levels and locations of p-SMAD2/3, active $\alpha_5\beta_1$-integrin, and pFAK correlate with short overall survival in RCC patients. (**A–C**) CART-generated survival curves depicting overall survival (OS) as a function of stromal assorted marker levels in RCC patients. (**A**)

Figure 13—figure supplement 3 continued on next page

Figure 13—figure supplement 3 continued

Left and middle curves correspond to mean and total intensity levels of stromal pSMAD2/3 and right curves to pSMAD2/3 mean intensity levels particularly localized at stromal nuclei, as a function of OS. (**B**) OS curves as a function of stromal active $\alpha_5\beta_1$-integrin levels. Top left curves show mean intensity of active $\alpha_5\beta_1$-integrin related to OS, top middle curves show mean intensity of active $\alpha_5\beta_1$-integrin at 3D adhesions related to OS, and top right curves show the percentage area coverage of active $\alpha_5\beta_1$-integrin at 3D adhesions related to OS. Bottom left curves depict median intensity levels of active $\alpha_5\beta_1$-integrin away from 3D adhesions, while bottom right curves depict percentage area coverage of active $\alpha_5\beta_1$-integrin away from 3D adhesions. (**C**) Curves depicting OS as a function of stromal pFAK. Top left curves show mean intensity of pFAK related to OS, top middle curves show percentage area coverage of pFAK related to OS, and top right curves show the total intensity pFAK related to OS. Bottom left curves depict median intensity levels of pFAK at 3D adhesions, bottom middle curves depict percentage area coverage of pFAK at 3D adhesions, and bottom right curves depict total intensity of pFAK at 3D adhesions. Colored tick-lines crossing Y axes indicate 0.5 survival marks and correspond to X axis locations that mark the median survival times obtained from the assorted curves. P values are shown. All patient data as well as SMIA-CUKIE-generated data corresponding to human cohort constructed TMAs (shown in ***Table 6***) can be found in the online table at the following publically available link: https://www.foxchase.org/sites/fccc/files/assets/cukierman_Franco-Barraza%20SMIA-CUKIE-Dec-2016.xlsx. Since our cohorts were comprised of samples obtained from surgeries, early neoplastic stages were overrepresented. Note that the above-mentioned links host RCC clinical data that provided the following results, which were obtained prior to CART analyses to assure that in spite of the bias provided by the use of surgical samples, the cohort in question showed significant associations between clinical and outcome variables and OS and Disease-Specific Survival (DSS): associations between pathological stage and OS had HRs of 2.4 (Uni; p=1.11E-10; 95% CI 1.9–3.2) and 3.2 (MVA; p=0.001; 95% CI 1.6–6.2), respectively. Also, Uni analyses of pathological T, N and M showed significant correlation with OS (T —HR = 2.0, p=4.16E-05, 95% CI 1.4–2.8; N — HR = 2.1, p=0.0003, 95% CI 1.4–3.1; and M — HR = 5.4, p=3.79E-10, 95% CI 3.2–9.1). Similarly, Uni and MVA analyses suggested that shorter DSS times are associated with advanced pathological stage (Uni —HR = 3.1, p=7.94E-11 and 95% CI 2.2–4.3; MVA — HR = 3.4, p<0.0001% and 95% CI 1.6–7.3).

DOI: 10.7554/eLife.20600.057

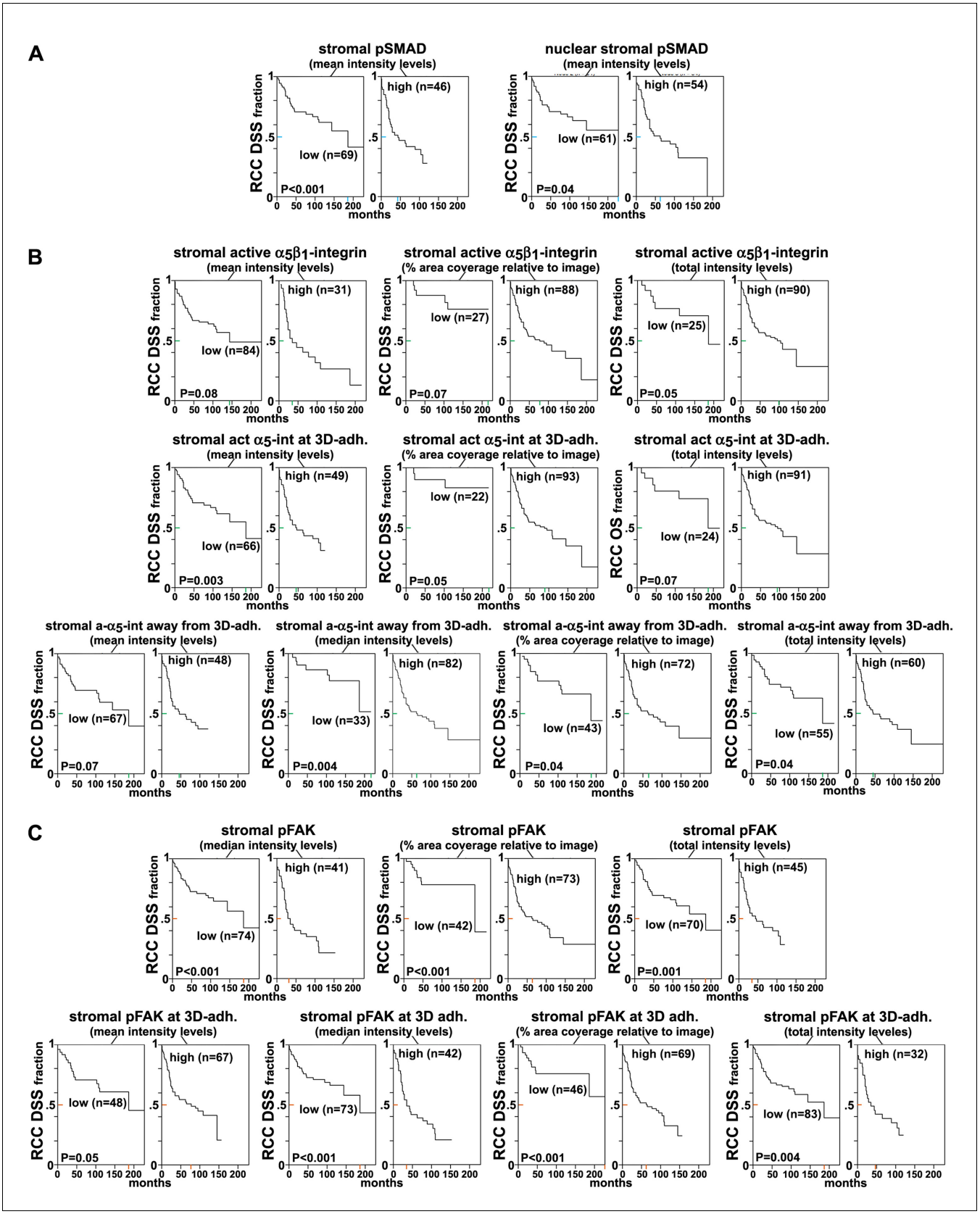

Figure 13—figure supplement 4. Stromal levels and locations of p-SMAD2/3, active $\alpha_5\beta_1$-integrin, and pFAK correlate with short disease specific survival in RCC patients. (**A-C**) CART-generated survival curves depicting disease specific survival (DSS) as a function of stromal assorted marker levels in

Figure 13—figure supplement 4 continued on next page

Figure 13—figure supplement 4 continued

RCC patients. (**A**) Left and right curves correspond to mean stromal-and stromal-nuclei- localized intensity levels of pSMAD, related to DSS. (**B**) DSS curves as a function of stromal active $\alpha_5\beta_1$-integrin levels. Top left curves show mean intensity of active $\alpha_5\beta_1$-integrin related to DSS, top middle curves show stromal percentage active $\alpha_5\beta_1$-integrin related to DSS, and top right curves show the total stromal intensity levels of active $\alpha_5\beta_1$-integrin related to DSS. Middle left, middle and right curves depict mean, percentage coverage and total intensity levels of active stromal $\alpha_5\beta_1$-integrin at 3D adhesions, respectively, each related to DSS. Bottom row from left to right corresponds to mean, median, percentage coverage and total intensity levels of active stromal $\alpha_5\beta_1$-integrin away from 3D adhesions, each related to DSS. (**C**) Survival curves depicting DSS as a function of stromal pFAK. Top from left to right: curves showing median, percentage coverage and total intensity levels of stromal pFAK related to DSS. Bottom from left to right: curves showing mean, median, percentage coverage and total intensity of stromal pFAK localized at 3D-adhesions related to DSS. Colored tick-lines crossing Y axes indicate 0.5 survival marks and correspond to X axis locations that mark the median survival times obtained from the assorted curves. P values are shown. All patient data as well as SMIA-CUKIE-generated data corresponding to human cohort constructed TMAs (shown in ***Table 6***) can be found in the online table at the following publically available link: https://www.foxchase.org/sites/fccc/files/assets/cukierman_Franco-Barraza%20SMIA-CUKIE-Dec-2016.xlsx. Note that since our cohorts comprised of samples obtained from surgeries, early neoplastic stages were overrepresented.

DOI: 10.7554/eLife.20600.058

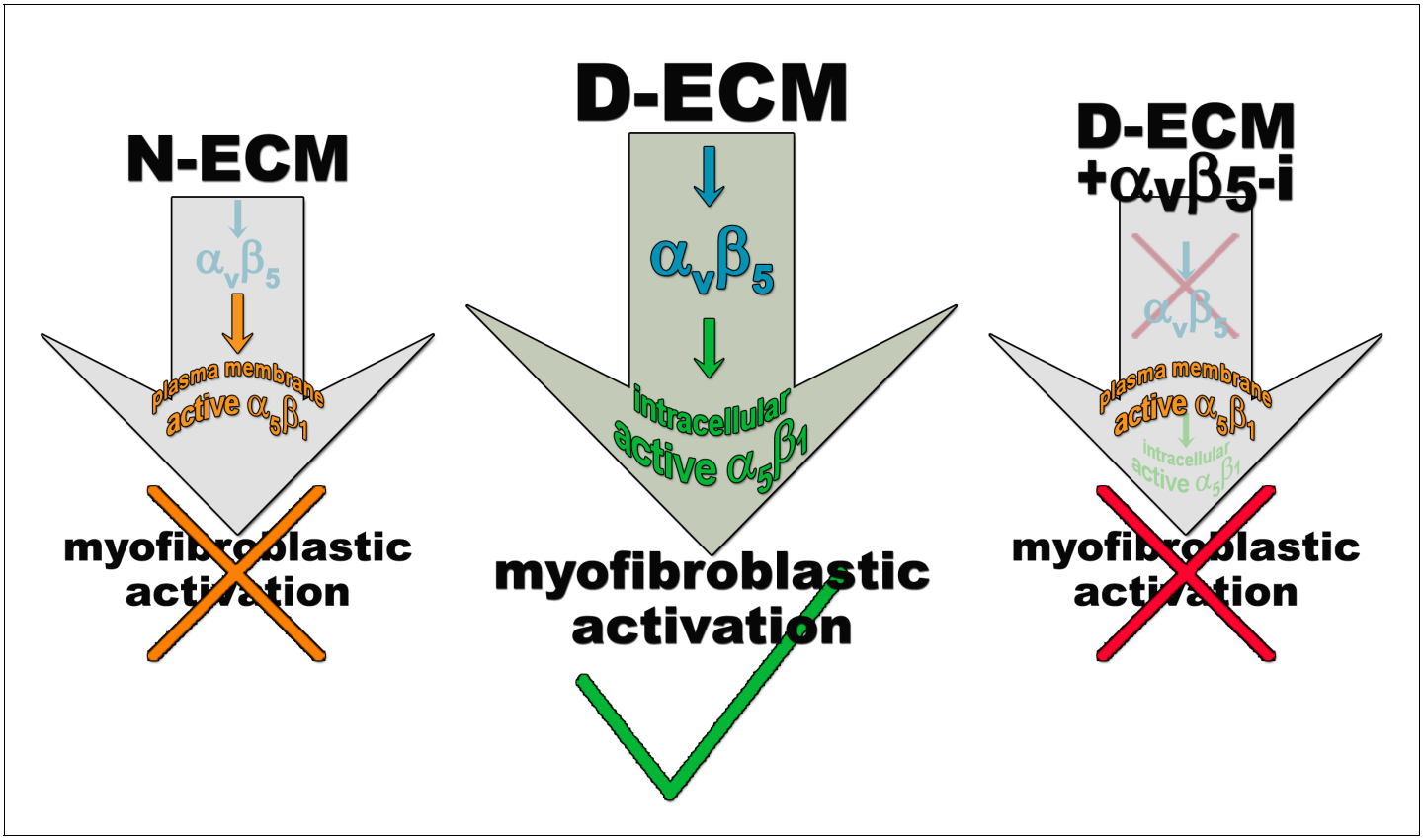

Figure 14. Model depicting D-ECM-induced $\alpha_V\beta_5$ regulation of active $\alpha_5\beta_1$-integrin localization during naïve-to-myofibroblastic activation. Essentially, naïve fibroblasts grown in N-ECMs do not trigger a surplus in active $\alpha_V\beta_5$ and $\alpha_5\beta_1$-integrin conformations. Consequently, the non-pathological N-ECM spares regulation of $\alpha_V\beta_5$-integrin activity and assures physiological accumulation of low active $\alpha_5\beta_1$-integrin levels at the PM, rendering fibroblasts inactive. D-ECMs induce an excess of active $\alpha_5\beta_1$-integrin and regulate $\alpha_V\beta_5$-integrin-mediated relocation of active $\alpha_5\beta_1$-integrin from the PM to intracellular (e.g., late endosomal) pools, resulting in myofibroblastic activation. Last, this D-ECM activity is dependent on the activity of $\alpha_V\beta_5$-integrin, as inhibition of $\alpha_V\beta_5$-integrin maintains active $\alpha_5\beta_1$-integrin at the PM (similarly to N-ECM regulation of active $\alpha_5\beta_1$-integrin locations), which averts D-ECM-induced myofibroblastic activation. The summarized data provide a possible explanation for the early model presented in ***Figure 3G***, which called for a D-ECM control of $\alpha_v\beta_5$ regulation of active $\alpha_5\beta_1$ and suggests that the alluded to regulation constitutes a re-localization of active $\alpha_5\beta_1$ to intracellular endosomal compartments, allowing D-ECM-induced naïve-to-myofibroblastic activation.

DOI: 10.7554/eLife.20600.059